POLITECNICO DI MILANO

School of Industrial and Information Engineering

Master of Science in Aeronautical Engineering

Dipartimento di Scienze e Tecnologie Aerospaziali

Ritz Approach for the Analysis of Curvilinearly Stiffened Panels

Advisor: Prof. Riccardo Vescovini

Co-Advisor: Prof. Lorenzo Dozio

Co-Advisor: Dr. Vincenzo Oliveri

Master Thesis by:

Davide Pizzi Matr. 842210

Academic Year 2017-2018

Acknowledgements

I wish to express my deepest gratitude to professor Riccardo Vescovini for the constant support and patience he offered me during this thesis project. His constant help has allowed me to gain one of the greatest achievements of my life.
I would like to thank Lorenzo Dozio for his support, and Vincenzo Oliveri, for his invaluable help and for always treating me as a friend since the very first day of my stay in Limerick.
I would also like to take this opportunity to thank professor Paul Weaver and the whole VariComp project committee for the warm hospitality in their research group in UL.

Un ringraziamento particolare va ai miei genitori Luigi e Francesca, e a mia sorella Giulia, senza di loro nulla di tutto questo sarebbe stato possibile. L'ultimo ringraziamento, ma non per importanza, va ad Agnese, compagna di studio e di vita, che mi ha sostenuto durante questi duri anni di università.

Abstract

Innovative manufacturing techniques open the door to improved flexibility in the design of aerostructures. In the past few years, research efforts carried out at VTech demonstrated the potential benefits due to structural panels stiffened with curvilinear – instead of straight – stringers. One critical issue in the design of these panels is the ability to efficiently cope with increased geometrical complexity. For instance, finite element models need to be carefully realized to guarantee proper mesh regularity, and to avoid the presence of distorted elements. This aspect, in conjunction with the time needed for the analysis, is of crucial importance when performing preliminary design optimizations. In this context, the activity aims at developing a fast method for the efficient analysis of curvilinearly stiffened panels. A Ritz-based approach is developed, which is capable of predicting the linear response (static and buckling analysis) and the dynamic one (free vibrations) with reduced computational burden. The quality of the results is assessed by comparison against finite element calculations, demonstrating the potentialities of the tool as a mean for performing preliminary parametric studies to assess the potential benefits of this innovative structural solution.

Sommario

Tecnologie di produzione innovative hanno aperto la strada ad una maggiore flessibilità nel progetto di strutture aeronautiche. Negli ultimi anni, attività di ricerca svolte presso il Vtech hanno dimostrato i potenziali benefici dell'impiego di pannelli strutturali irrigiditi con correnti curvilinei, anzichè rettilinei. Un problema critico nel progetto di questi pannelli è la capacità di far fronte alla maggiore complessità geometrica in modo efficiente. Per esempio, i modelli a elementi finiti devono essere realizzati con particolare cura in modo da garantire sufficiente regolarità della mesh, ed evitare la presenza di elementi distorti. Questo aspetto, insieme al tempo necessario per l'analisi, è d'importanza fondamentale per la risoluzione di problemi di ottimizzazione strutturale. In questo contesto, il lavoro mira alla realizzazione di un metodo efficiente per l'analisi di pannelli irrigiditi con correnti curvilinei. Attraverso l'utilizzo di un aprroccio alla Ritz, è stato sviluppato uno strumento in grado di predire con limitato onere computazionale la risposta lineare (analisi statica e di buckling), e quella dinamica (vibrazioni libere). La qualità dei risultati è valutata attraverso il confronto con analisi a elementi finiti, dimostrando le potenzialità del metodo come strumento per realizzare studi parametrici preliminari che possano stimare i potenziali benefici di questa innovativa soluzione strutturale.

Contents

List of Figures

List of Tables

1. Introduction

Aeronautical structures progress has always been determined by the constant quest for increasingly efficient solutions, that can ensure solid structures, capable of withstanding high level of stress, with the lowest possible weight burden. Alongside the necessity to reduce the costs of aircraft production, the reasons are nowadays related to fuel efficiency, generated noise, NOx emissions, that have become of prime importance because of environmental concerns.
The classical configuration adopted for the load-carrying part of the wing (the *wing-box*) is an explicative example of the effort done to solve this trade-off. Straight stiffening members like spars, ribs, and stringers are riveted to wing panels, giving shape to a strong lightweight structure, facilitating the manufacturing process. Nonetheless, novel manufacturing techniques were recently developed in an attempt to minimize the joints weight contribute and material wastage. Moreover, these technologies open the door to a new design philosophy, which makes use of *unitized structures*: monolithic constructions where the employment of many mechanically fastened structural parts is replaced by integrated structures. In addition to reduced manufacturing costs, this solution can improve the flexibility of airframe design, allowing the fabrication of more complex shape structures. For example curvilinear stiffening members can be realized with negligible additional cost and time with respect to conventional processes.
In the context of composite materials, it has been proven how the employment of curvilinear reinforcement fibers can increase the stability performance of laminated panels [1], by spatially varying the fiber orientation and, consequently, the stiffness of the structure (for this reason they are called variable stiffness or variable angle tow laminates). Although variable stiffness panels

should not be confused with curvilinearly-stiffened ones, they share the common idea of tailoring the stiffnesses, and leading to non-uniform elastic properties over the panel domain. Weaver et al. [2] demonstrate how a unitized wing-box demonstrator with VAT laminates can be efficiently manufactured using Automated Fiber Placement technique. A laser-assisted automated tape placement (LATP) machine is able to wind the wingbox's skin directly over the stiffeners, while the bonding of skin and stiffeners is achieved using a laser beam in-situ consolidation.

Alongside VAT laminates, the design space of aeronautical panels can be broadened also by using arbitrarily curved stiffeners, recently introduced by Kapania et al. in [3]. While from a manufacturing point of view these kind of structures can be easily integrated in an unitized structure manufacturing process [4], they present some critical issues during the modelling phase. For instance, finite element models need to be carefully realized to guarantee proper mesh regularity, and avoiding the presence of distorted elements.

In his dissertation, Locatelli [5] implemented curvilinear stiffening members in the design process of supersonic aircraft wing-box, using a finite elements based approach. The optimization framework required the development of a tool able to automatically generate the geometry and perform the re-meshing for every variation in the structure configuration. To obviate this difficulty, Kapania et al. [6] proposed the implementation of a contact algorithm to enforce the compatibility condition between plate and stiffeners, making use of the interpolation polynomials employed in the finite element method. With this technique plate and stiffeners do not have to share their nodes and no re-meshing is needed.

The modelling phase can be further simplified by using "mesh-free" techniques, as the plate/stiffeners compatibility can be more easily enforced. Among them, the Ritz method [7] has proved to be a successful alternative to finite element method, for the structural analysis of plates and shells. For instance, Bisagni and Vescovini [8–10] developed analytical and semi-analytical formulations for the linear buckling and non-linear post-buckling analysis of stiffened panels, using a variational approach and applying the Ritz method. The geometrical symmetry of the problem, and the assumption

of a local buckling mode shape give the authors the possibility of studying the complete structure considering only a reduced portion of the whole stiffened panel, giving birth to a very efficient approach which they employed to develop a fast procedure for the design and optimization of stiffened panels [11–13].

When unconventional stiffeners configuration lead to increased geometry complexity, similar simplifications cannot be adopted. However this aspect does not represent a limitation for the Ritz method. Brubak et al. [14, 15] used the Ritz method for the vibration and buckling analysis of plates with arbitrary straight stiffener arrangements, and for the prediction of the ultimate strength [16]. They showed how this approach is capable of achieving relatively high numerical accuracy with low computational efforts.

Tamijani and Kapania [17] used a Ritz-based approach for the buckling and vibration analysis of isotropic curvilinearly stiffened plates, while Shi et al. [18] used the same approach for the free-vibration analysis of curvilinearly stiffened shallow shells. Alongside the Ritz method, element-free Galerkin method was employed by Tamijani and Kapania [19, 20] for the analysis of isotropic curvilinearly stiffened plates, and their results for free-vibration analysis were validated with experimental data [21].

In this context, the present activity aims at developing a fast yet accurate method for the efficient analysis of curvilinearly stiffened composite panels. A Ritz-based approach is developed, which allows to speed-up the modelling phase, and to predict the structural response with reduced computational burden.

The work is divided into three parts. The first part mainly focuses on the formulations for the structural analysis of curvilinearly stiffened composite plates. In the second part the accuracy of the results is assessed through convergence studies and comparisons against finite element calculations. Parametric studies are then performed in order to achieve a better understanding of the mechanical behaviour of this kind of structure. In the last part further studies are conducted on a structure resulting from a preliminary sizing process of an aircraft wing-box, in order to investigate the benefits that curvilinearly stiffened panels may bring in a real application scenario.

2. Basic Concepts

2.1 Strong and weak formulation of the elastic problem

The mathematical representation of the elastic problem is expressed by means of governing equations describing the change of configuration of a deformable body under the action of external loads and constraints. The set of non-linear partial differential equations expressing the equilibrium can be obtained by applying fundamental physical laws such as conservation of the mass and linear momentum [24]:

$$\nabla \cdot \mathbf{P} + \mathbf{b} = \rho_0 \, \mathbf{a} \quad \text{in } \Omega \tag{2.1}$$

with boundary conditions:

$$\begin{aligned} \mathbf{P} \cdot \mathbf{n} &= \mathbf{f} \quad \text{on } \partial\Omega_N \\ \mathbf{u} &= \mathbf{g} \quad \text{on } \partial\Omega_D \end{aligned} \tag{2.2}$$

where $\mathbf{P}$ is the first Piola-Kirchhoff stress tensor and ρ_0 is the density of the reference configuration. From a physical point of view the external volume forces $\mathbf{b}$ along with the inertial ones, if any, determine a state of internal stress which satisfies Eq. 2.1. Boundary conditions of Eq. 2.2 express the equilibrium on the loaded surface $\partial\Omega_N$ (Neumann or natural boundary condition) and the prescribed displacement on the constrained surface $\partial\Omega_D$ (Dirichlet or essential boundary condition). The stress measure is chosen due the fact that the equilibrium is written in the initial, or reference, configuration, and consequently that the physical laws are applied in a *lagrangian* sense: the

attention is focused on the variation of the quantities of interest experienced by a particle during the deformation process; since the particle can be identified by its position $\mathbf{x}_0$ in the reference configuration, all of those quantities (including displacements) can be seen as functions of the initial position $\mathbf{x}_0$ of that particle. This means that there exists a function $\mathbf{x} = \phi(\mathbf{x}_0,t)$ that gives the position of the particle $\mathbf{x}_0$ after deformation. The function ϕ is indeed a transformation of coordinates and the quantity $\mathbf{F} = \nabla\phi$, named deformation gradient, is its Jacobian matrix.
In addition to the equilibrium requirements of Eqs. 2.1 and 2.2, the solution of the elastic problem demands that compatibility conditions are satisfied as well. To this aim, the compatibility requirements are introduced in the form of strain-displacement relations, referring to the strain tensor measure due to Green-Lagrange. In particular, the expression reads:

$$\boldsymbol{\varepsilon} = \frac{1}{2}\left(\nabla\mathbf{u} + \nabla\mathbf{u}^T + \nabla\mathbf{u}^T\nabla\mathbf{u}\right) \tag{2.3}$$

where $\boldsymbol{\varepsilon}$ is the Green-Lagrange strain tensor, which is energetically conjugate to the II Piola-Kirchhoff stress tensor $\boldsymbol{\sigma} = \mathbf{F}^{-1}\mathbf{P}$. In the case of large displacements, strains are non-linear functions of the displacement field, while in the case of a non-linear material, the stress-strain relation is non-linear. In general, a closed form solution of the elastic problem can be hardly achieved. Moreover strong requirements on the regularity of the solution make the problem written in differential form difficult to handle when it comes to look for an approximate solution; in many cases it is more convenient to rewrite the equations in integral (or weak, or variational) form. To this aim the principle of virtual work can be considered. Being a virtual displacement $\delta\mathbf{u}$ an infinitesimal, arbitrary and constraint compatible change of configuration, and the virtual work a work done by a real system of forces for a virtual displacement field, the principle can be stated as: if a continuous body is in equilibrium, the virtual work of all actual forces in moving through a virtual displacement is zero [25]:

$$\delta W_i - \delta W_e \equiv \delta W = 0 \tag{2.4}$$

where δW_i is the virtual work done by internal stresses, while δW_e is the virtual work done by external forces. Substituting their expression the principle writes:

$$\delta W = \int_\Omega \delta\boldsymbol{\varepsilon} : \boldsymbol{\sigma}\, d\Omega + \int_\Omega \rho_0\, \delta\mathbf{u}\cdot\ddot{\mathbf{u}}\, d\Omega - \int_\Omega \delta\mathbf{u}\cdot\mathbf{b}\, d\Omega - \int_{\partial\Omega_N} \delta\mathbf{u}\cdot\mathbf{f}\, d\partial\Omega = 0 \quad (2.5)$$

In the weak-form statement of Eq. 2.5, requirements over the regularity of the solution are relaxed if compared to the strong-form formulation. Indeed, the solution has to be regular enough to guarantee the existence of the integrals above, leading to a weaker requirement compared to the strong formulation case. If the system is conservative, it is sufficient to find the stationarity point of a functional: $\delta\,\Pi = 0$. Considering a static problem this functional is the total potential energy Π_{tot}:

$$\delta\,\Pi_{tot} = \delta\,(U + V) = 0 \quad (2.6)$$

where the terms in brackets are the strain energy function, U, and the potential of the external forces, V, respectively[1]. This is consistent with the stationarity of the total potential energy theorem, which states: among all the compatible configurations, that one which is also equilibrated minimizes the total potential energy [22]. In the case of linear hyperelastic constitutive law, the terms in Eq. 2.6 are:

$$U = \frac{1}{2}\int_\Omega \boldsymbol{\varepsilon} : \boldsymbol{\sigma}\, d\Omega \quad (2.7)$$

$$V = -\left(\int_\Omega \mathbf{u}\cdot\mathbf{b}\, d\Omega + \int_{\partial\Omega_N} \mathbf{u}\cdot\mathbf{f}\, d\partial\Omega\right) \quad (2.8)$$

[1]For a conservative system the work done by the internal forces going from configuration A to configuration B, does not depend on the deformation process, and can be obtained from the values the strain energy function assumes in A and B. This has to be true also for the work done by external forces that can be computed evaluating the potential in A and B; in the case of configuration-independent loads such potential always exists. The virtual internal work can be seen as the differential of the strain energy function, while the virtual external work as the differential of the potential of the external forces.

In this work the approach is based on the principle of virtual work, where inertial forces can be easily accounted for by referring to the d'Alembert principle[2]. The non-linear problem of Eq. 2.5 can be solved by using specific techniques for non-linear structural mechanics. Nonetheless this work is focused on linear behaviour of structures, hence a linearisation of the problem 2.5 around a reference configuration is be performed:

$$\Pi_\delta \simeq \Pi_{\delta 0} + \partial\Pi_\delta = 0 \tag{2.9}$$

Physically this means that small perturbations around an equilibrated configuration are considered. Such reference configuration can be the natural one, devoid of internal tensions, or a solution of a previously solved, potentially non-linear, structural problem. Considering only configuration-independent external forces, the linearisation leads to the following problem [23]:

$$\begin{aligned}\Pi_\delta \simeq &\int_\Omega \delta\boldsymbol{\varepsilon}_0 : \partial\boldsymbol{\sigma}\, d\Omega + \int_\Omega \partial\delta\boldsymbol{\varepsilon} : \boldsymbol{\sigma}_0\, d\Omega \\ &+ \int_\Omega \rho_0\, \delta\mathbf{u}\cdot\ddot{\mathbf{u}}\, d\Omega - \int_\Omega \delta\mathbf{u}\cdot\mathbf{b}\, d\Omega - \int_{\partial\Omega_N} \delta\mathbf{u}\cdot\mathbf{f}\, d\partial\Omega = 0\end{aligned} \tag{2.10}$$

where a quantity evaluated in the reference configuration is identified with the notation $(\,\cdot\,)_0$. Considering the constitutive law of an hyperelastic material and neglecting the volume forces which are not taken into account in this work, Eq. 2.10 becomes:

$$\int_\Omega \delta\boldsymbol{\varepsilon}_0 : \mathbb{D} : \partial\boldsymbol{\varepsilon}\, d\Omega + \int_\Omega \partial\delta\boldsymbol{\varepsilon} : \boldsymbol{\sigma}_0\, d\Omega + \int_\Omega \rho_0\, \delta\mathbf{u}\cdot\ddot{\mathbf{u}}\, d\Omega - \int_{\partial\Omega_N} \delta\mathbf{u}\cdot\mathbf{f}\, d\partial\Omega = 0 \tag{2.11}$$

where $\mathbb{D}$ is the fourth order elasticity tensor. The linearisation of the Green-

[2] As an alternative one could use the Hamilton's principle, which allows to exploit the definition of conservative system.

Lagrange strain tensor $\partial\boldsymbol{\varepsilon}$ around the reference configuration results in the small strain tensor: $\boldsymbol{\varepsilon}_l = \frac{1}{2}\left(\nabla\mathbf{u} + \nabla\mathbf{u}^T\right)$ [23]. In the same way $\delta\boldsymbol{\varepsilon}_0 = \delta\boldsymbol{\varepsilon}_l$. Eventually the problem is written in its final form:

find $\mathbf{u} \in H^d$ such as

$$\delta W_i\left(\delta\mathbf{u},\mathbf{u}\right) + \delta W_e\left(\delta\mathbf{u},\ddot{\mathbf{u}}\right) = 0 \qquad \forall\, \delta\mathbf{u} \in H^d \tag{2.12}$$

where space H^d is the linear space where the solution and the virtual displacements are defined, and it has to guarantee the boundedness of the integrals in Eq. 2.5. After some manipulation on the term $\partial\delta\mathbf{E}$, the two term in Eq. 2.12 can be written as:

$$\begin{aligned}
\delta W_i\left(\delta\mathbf{u},\mathbf{u}\right) &= \int_\Omega \delta\boldsymbol{\varepsilon}_l : \mathbb{D} : \boldsymbol{\varepsilon}_l \, d\Omega + \int_\Omega \boldsymbol{\sigma}_0 : \left[\left(\nabla_0\mathbf{u}\right)^T \nabla_0\delta\mathbf{u}\right] \, d\Omega \\
\delta W_e\left(\delta\mathbf{u},\ddot{\mathbf{u}}\right) &= \int_\Omega \rho_0 \, \delta\mathbf{u}\cdot\ddot{\mathbf{u}} \, d\Omega - \int_{\partial\Omega_N} \delta\mathbf{u}\cdot\mathbf{f} \, d\partial\Omega_N = 0
\end{aligned} \tag{2.13}$$

The uppercase d in the notation used for the linear space H^d is there only to highlight that every component u_i $(i = 1, \ldots, d)$ of the vector $\mathbf{u} \in H^d$ is an element belonging to H. In this case each component of vectorial fields has to be square-integrable with square-integrable gradient in Ω, and this has to be true for every time instant t. A space of square-integrable function is defined as:

$$L^2(\Omega) = \left\{ f : \Omega \to \mathbb{R} \quad \textit{such that} \quad \left\| f \right\|_{L^2} = \sqrt{\int_\Omega |f|^2 \, d\Omega} < \infty \right\} \tag{2.14}$$

So each component u_i and δu_i $(i = 1, \ldots, d)$ has to satisfy:

$$u_i \,,\, \delta u_i \in V = \left\{ f \in L^2(\Omega) \quad \textit{with}\ \nabla f \in L^2(\Omega) \right\} \tag{2.15}$$

Another requirement on the unknown functions is the fulfillment of the essential boundary condition for the solution and the compatibility for the virtual displacements. In the case of homogeneous essential boundary condition both $\delta\mathbf{u}$, $\mathbf{u}$, have to be null at the boundary, therefore they are defined in the same space $H_0^d = \left\{\mathbf{f} \in H^d \quad with\ \mathbf{f} = \mathbf{0}\ on\ \partial\Omega_D\right\}$. On the other hand, in the case of a finite prescribed movement the space of the solution $\mathbf{u}$ has to be $H_g^d = \{\mathbf{f} \in H \quad with\ \mathbf{f} = \mathbf{g}\ on\ \partial\Omega_D\}$, while the virtual displacements are still in H_0^d, as on the Dirichlet boundary $\delta\mathbf{u}$ is still null by definition. However it is noted that, introducing a known function $\mathbf{u}_0 \in H_g^d$, a solution like $\mathbf{u} = \tilde{\mathbf{u}} + \mathbf{u}_0$ with $\tilde{\mathbf{u}} \in H_0^d$, satisfies the essential boundary conditions: the relative displacement $\tilde{\mathbf{u}}$ is the new unknown and the prescribed one, $\mathbf{u}_0$, leads to a new term in the virtual external work.

2.2 Approximate solution

The principle of virtual work states that the solution of the structural problem makes the functional δW null for an infinite number of virtual displacement functions $\delta\mathbf{u}$. The vectorial space H in which the solution and virtual displacements are defined is an infinite dimensional space. A common practice to solve the problem in Eq. 2.12 is to look for an approximate solution through the discretization of the problem: the solution is sought within a finite dimensional space $\overline{H}$ that is a subspace of the infinite dimensional one (hence assuring the existence of the integrals in Eq. 2.13):

$$\overline{H} \subset H\,, \qquad dim\,\overline{H} = N < \infty \tag{2.16}$$

Thanks to this property it is possible to describe any element $u \in \overline{H}$ as a linear combination of a linearly-independent set of functions ϕ_i forming a basis in $\overline{H}$, exactly in the same way as in an euclidean space $\mathbb{R}^n$ every point can be obtained from a set of base vectors [24]:

$$
\begin{aligned}
&u(x,y,z,t) = \boldsymbol{\phi}^T(x,y,z)\,\mathbf{a}(t) = \sum_{i=1}^{N_h} \phi_i(x,y,z)\,a_i(t)\,, \\
&\text{with } \overline{H} = span\,\{\phi_1, \phi_2, \ldots, \phi_N\}
\end{aligned}
\tag{2.17}
$$

where $a_i(t) \in \mathbb{R}$ are unknown coefficients. This approach can be simply extended to the vectorial fields case. A possible way to define the element $\mathbf{u} = \{u_1, \ldots, u_d\} \in \overline{H}^d$ as a linear combination of the basis is the following:

$$
\mathbf{u} = \begin{Bmatrix} u_1 \\ u_2 \\ \vdots \\ u_d \end{Bmatrix} = \begin{bmatrix} \boldsymbol{\phi}_1^T & \mathbf{0} & \cdots & \mathbf{0} \\ \mathbf{0} & \boldsymbol{\phi}_2^T & \cdots & \mathbf{0} \\ \vdots & \vdots & \ddots & \vdots \\ \mathbf{0} & \mathbf{0} & \cdots & \boldsymbol{\phi}_d^T \end{bmatrix} \begin{Bmatrix} \mathbf{a}_1 \\ \mathbf{a}_2 \\ \vdots \\ \mathbf{a}_d \end{Bmatrix} = \boldsymbol{\Phi}^T \mathbf{d} \tag{2.18}
$$

The same notation can be straightforwardly adopted for the virtual displacements $\delta\mathbf{u}$. The key aspect is that now Eq. 2.12 does not need to be verified for all the infinite number of functions $\delta\mathbf{u} \in H^d$, but only for each function of the basis, as all the element in the finite dimensional space $\overline{H}^d$ is a linear combination of them. As it will be more accurately explained in the following sections, this means that the problem Eq. 2.12 can be reformulated through the following system of linear constant-coefficients difference equation:

$$
\mathbf{M}\ddot{\mathbf{d}} + (\mathbf{K} + \mathbf{K}_G)\,\mathbf{d} = \mathbf{P} \tag{2.19}
$$

where the matrix $\mathbf{M}$, $\mathbf{K}$, $\mathbf{K}_G$, result from the process of discretization. The choice of basis functions $\phi_i(x,y,z)$ determines the type of approximate method that is used. In this work the approach used to solve the structural problem is based on the Ritz method, where the bases are usually polynomials or trigonometric functions defined on the overall domain Ω. An important requirement on the Ritz functions is completeness, intended as the ability of representing a generic function $f \in H$ with the desired level of accuracy. The distance between a function $f \in H$ and a function $\overline{f} \in \overline{H}$ is measured using the energy norm, descending from the variational formulation of the problem. In this case the requirement on completeness can be stated as: for

each $f \in H$ and each $\varepsilon > 0$, there exists an $N^* \in \mathbb{N}$ such that:

$$\left\| f - \overline{f} \right\|_{energy} = \sqrt{\left(|\nabla f| - |\nabla \overline{f}| \right)^2} < \varepsilon \quad \forall\, N \geq N^* \tag{2.20}$$

In other words completeness means that with a rich enough set of Ritz functions, it is possible to represent any function in H with any level of accuracy. For example, considering a 1D problem, any function can be approximated as a linear combination of polynomials (Weierstrass theorem). The basis $\{1,x,x^2,x^3,...\}$ is then a complete basis, but if, for instance, the x^2 term is missed, such basis will never succeed in approximating a quadratic function no matter how rich it is, because it's not complete. Convergence of the Ritz method is guaranteed for the solution and its derivatives up to the highest order of differentiation entering the virtual internal work:

$$\lim_{h \to \infty} \left\| \mathbf{u} - \overline{\mathbf{u}} \right\|_H = 0 \tag{2.21}$$

where:

$$\left\| f \right\|_H = \sqrt{\left\| f \right\|_{L^2}^2 + \left\| \nabla f \right\|_{L^2}^2} \tag{2.22}$$

This implies convergence not only for displacements, but also for strains and stresses, as they are related to the first derivatives of the solution.

Concepts of completeness and convergence have been introduced for the general three-dimensional problem. There are cases in which it is possible to reduce the problem dimensions through proper assumptions on the displacement field and the state of stress. This is the case of beam and plate kinematic models where the expression of the principle virtual work is modified in order to suit for 2D and 1D continua. First order shear deformation theory for plates, and Timoshenko theory for beams, provide the kinematic assumptions considered in the present work to model curvilinearly stiffened plates. Using these kinematic models, even if the principle of virtual work assumes different aspects, the conclusions on completeness and convergence done for the three-dimensional case are still valid, as strains and stresses are

still obtained through the first derivatives of the solution. In other kinematic models this may not be true. For example in the Euler-Bernoulli beam theory [25], the strain deformation energy is related to the second derivative of the transversal displacement. This means that energy norm, used to check completeness, has to be performed on the second derivative of the unknown. Moreover, in this case, convergence is assured for bending moment, but not for shear, as it is related to the third derivative of the unknown function.

3. Modelling of curvilinearly stiffened plates

In this part all the steps required for the modelling of plates stiffened with curvilinear stringers are presented in detail. After a brief introduction of the problem, the attention is focused on the assumptions and the methods adopted to perform the structural analysis of these kind of structures. The principle of virtual work will be at first derived for 2-D and 1-D continua, and then discretized using the Ritz method in order to seek for an approximate solution for vibrations, linear static and buckling analyses.

3.1 Problem statement

Curvilinearly stiffened panels can be seen as the assembly of two structural components as shown in the sketch of Figure 3.1. In the picture, a laminated composite plate is stiffened by an I-shaped beam that follows a curvilinear path on the plate surface.
In this work the stiffeners lamination direction is taken perpendicular to that of the plate, meaning that, referring to Figure 3.1, the plies are stacked along the smallest dimension of the beam section. This subdivision defines the scheme of the modelling procedure. At first, plate and stringers can be treated separately, and the displacement field for each structural element is described through a suitable kinematic model. As said previously, this allows to reduce the dimensions of the problem and leads to two different expressions for the virtual internal and external works. Then this two models has to be assembled in a single mathematical description of the problem and the issue of the plate/stiffener compatibility enforcement is discussed. The seek

for an approximate solution is conducted discretizing the problem with the Ritz method. One of the important aspects of this thesis is the development of a technique that is able to create flexible curvilinear shapes using the least number of inputs as possible, in order to give the possibility to change the stiffeners geometrical configuration with the least effort. As previously said, the "mesh-free" nature of the Ritz method makes it particularly suitable to achieving this last target. This modelling phase aims to develop a programming tool which is capable of predicting the linear response (static and buckling analysis) and the dynamic one (vibrations).

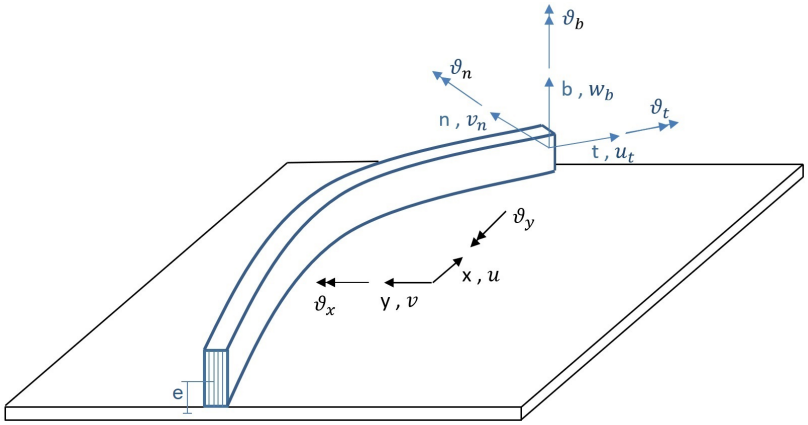

Figure 3.1: Schematic representation of a curvilinearly stiffened plate.

3.2 Plate model

3.2.1 Kinematics

The plate is modelled using the first order shear deformation theory (FSDT) where the displacements of every point of the plate is assumed to be a linear combination of unknown functions and the thickness coordinate z [25]:

$$u_i(x,y,z,t) = \sum_{k=0}^{1} z^k \, \psi_i^{(k)}(x,y,t) \tag{3.23}$$

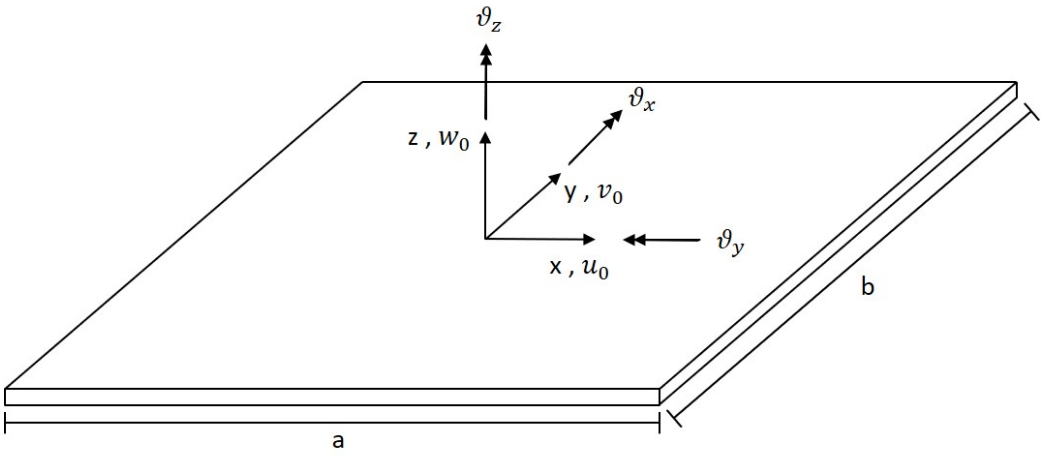

Figure 3.2: Definition of global coordinate system and plate displacement field.

where u_i is the ith component of displacement, (x,y) the in-plane coordinates, t the time, and $\psi_i^{(k)}$ are the linear displacements and rotation kinematics parameters of the midsurface [3]. More precisely, the form of the displacement field is the following:

$$\mathbf{u}_p = \begin{Bmatrix} u(x,y,z,t) \\ v(x,y,z,t) \\ w(x,y,z,t) \end{Bmatrix} = \begin{Bmatrix} u^0(x,y,z,t) \\ v^0(x,y,z,t) \\ w^0(x,y,z,t) \end{Bmatrix} + z \begin{bmatrix} 1 & 0 & 0 \\ 0 & 1 & 0 \\ 0 & 0 & 0 \end{bmatrix} \begin{Bmatrix} \theta_x(x,y,t) \\ \theta_y(x,y,t) \\ \theta_z(x,y,t) \end{Bmatrix} \tag{3.24}$$

$$= \mathbf{u}_p^0 + z\,\mathbf{L}\,\boldsymbol{\theta}_p$$

where the meaning of each variable is explained in Figure 3.2. It has to be pointed out that there is no elastic or inertial energetic contribute due to the "drilling" rotation θ_z, which is introduced for the enforcement of the plate/stiffener compatibility [26], as discussed later. In the FSDT theory, the hypothesis that the transverse section has to be perpendicular to the midsurface after deformation (Kirchhoff hypothesis) is relaxed. In this way

[3] Extending the summation for values of k > 1 one can obtain higher-order theories, introducing other unknowns difficult to interpret in physical terms, increasing the accuracy of the formulation but leading to a larger number of degrees of freedom.

the theory allows to take into account transverse shear energy, which can be relevant for moderately thick plates. As seen from Eq. 3.24 the transverse displacement w is constant along the thickness. The main benefit of making explicit the dependence on the thickness coordinate is to reduce the problem dimensions: under this assumption a 3D continuum can be studied in a 2D domain. The non-linear strain tensor components are computed from the definition of the Green-Lagrange strain tensor, under the assumption that the only non negligible quadratic terms are those related to the variation of the transversal displacement w along the in-plane coordinates, introducing the so called von Kármán hypothesis, a special case of geometric nonlinearity widely adopted in stability analysis of plates.
Introducing the notation $(\cdot)_{/\alpha}$ to express the derivative with respect to α, strain components can be written as:

$$\begin{aligned}
\varepsilon_{xx} &= u_{/x} + \frac{1}{2}\left(w_{/x}\right)^2 = u^0_{/x} + \frac{1}{2}\left(w^0_{/x}\right)^2 + z\,\theta_{x/x} = \varepsilon^0_{xx} + z\,k_{xx} \\
\varepsilon_{yy} &= v_{/y} + \frac{1}{2}\left(w_{/y}\right)^2 = v^0_{/y} + \frac{1}{2}\left(w^0_{/x}\right)^2 + z\,\theta_{y/y} = \varepsilon^0_{yy} + z\,k_{yy} \\
\gamma_{xy} &= u_{/y} + v_{/x} + w_{/x}\,w_{/y} \\
&= u^0_{/y} + v^0_{/x} + w^0_{/x}\,w^0_{/y} + z\left(\theta_{x/y} + \theta_{y/x}\right) = \gamma^0_{xy} + z\,k_{xy} \\
\gamma_{xz} &= w_{/x} + u_{/z} = w^0_{/x} + \theta_x \\
\gamma_{yz} &= w_{/y} + v_{/z} = w^0/y + \theta_y \\
\varepsilon_{zz} &= w_{/z} = 0
\end{aligned} \tag{3.25}$$

where the notation $\gamma_{\alpha\beta} = 2\varepsilon_{\alpha\beta}$ is adopted. Since $\varepsilon_{zz} = 0$, the transverse normal stress σ_{zz}, although not zero identically, does not appear in the virtual internal work. However, from practical considerations, it is more meaningful to assume $\sigma_{zz} = 0$, making use of the plane stress constitutive law instead of the plane strain one. In both cases the effect on the expression of the virtual internal work is the same. Another important consideration is that the transverse shear strains are constant along the thickness: in the reality these components are at least parabolic so this approximation can be corrected

using the shear factors in order to have a more reliable energetic contribute. All the other strain components depend linearly on the thickness coordinate z. The following compact notation can be introduced:

$$\begin{aligned} \boldsymbol{\varepsilon} &= \begin{Bmatrix} \varepsilon^0_{xx} \\ \varepsilon^0_{yy} \\ \gamma^0_{xy} \end{Bmatrix} + z \begin{Bmatrix} k_{xx} \\ k_{yy} \\ k_{xy} \end{Bmatrix} = \boldsymbol{\varepsilon}^0 + z\,\mathbf{k} \\ \boldsymbol{\gamma} &= \begin{Bmatrix} \gamma_{xz} \\ \gamma_{yz} \end{Bmatrix} \end{aligned} \tag{3.26}$$

where $\boldsymbol{\varepsilon}^0$ can be further divided in its linear and non-linear parts: $\boldsymbol{\varepsilon}^0 = \boldsymbol{\varepsilon}^0_l + \boldsymbol{\varepsilon}^0_{nl}$. In the present work laminated composite plates are considered. The state of tension inside each orthotropic lamina can be described as a plane-stress state with the addition of the transverse shear stresses (only $\sigma_{zz} = 0$). In this case the linear constitutive relations are expressed in lamina coordinates as:

$$\begin{aligned} \boldsymbol{\sigma}_1 &= \begin{Bmatrix} \sigma_1 \\ \sigma_2 \\ \sigma_{12} \end{Bmatrix} = \begin{bmatrix} \frac{E_1}{1-\nu_{12}\nu_{21}} & \frac{\nu_{12}E_2}{1-\nu_{12}\nu_{21}} & 0 \\ \frac{\nu_{12}E_2}{1-\nu_{12}\nu_{21}} & \frac{E_2}{1-\nu_{12}\nu_{21}} & 0 \\ 0 & 0 & G_{12} \end{bmatrix} \begin{Bmatrix} \varepsilon_1 \\ \varepsilon_2 \\ \gamma_{12} \end{Bmatrix} = \mathbf{Q}\,\boldsymbol{\varepsilon}_1 \\ \boldsymbol{\tau}_1 &= \begin{Bmatrix} \sigma_{13} \\ \sigma_{23} \end{Bmatrix} = \begin{bmatrix} G_{13} & 0 \\ 0 & G_{23} \end{bmatrix} \begin{Bmatrix} \gamma_{13} \\ \gamma_{23} \end{Bmatrix} = \mathbf{Q}_n\,\boldsymbol{\tau}_1 \end{aligned} \tag{3.27}$$

where E_1, E_2 are the elastic moduli in fibre and matrix direction respectively, ν_{12}, ν_{21} the Poisson coefficients, and G_{12}, G_{13}, G_{23} the in-plane and transversal tangential moduli. A laminated plate is made up by the stacking of a number of orthotropic laminae, called plies, with fibres oriented in different directions. For this reason the directions of orthotropy of each ply do not coincide with the global directions of the problem. In order to express stresses and strains in the same global coordinate system (laminate coordinates), the constitutive

law has to be rotated, obtaining:

$$\begin{aligned}\boldsymbol{\sigma} &= \begin{Bmatrix}\sigma_{xx}\\ \sigma_{yy}\\ \sigma_{xy}\end{Bmatrix} = \begin{bmatrix}\overline{Q}_{11} & \overline{Q}_{12} & \overline{Q}_{16}\\ \overline{Q}_{12} & \overline{Q}_{22} & \overline{Q}_{26}\\ \overline{Q}_{16} & \overline{Q}_{26} & \overline{Q}_{66}\end{bmatrix} \begin{Bmatrix}\varepsilon_{xx}\\ \varepsilon_{yy}\\ \gamma_{xy}\end{Bmatrix} = \overline{\mathbf{Q}}\,\boldsymbol{\varepsilon}\\ \boldsymbol{\tau} &= \begin{Bmatrix}\sigma_{xz}\\ \sigma_{yz}\end{Bmatrix} = \begin{bmatrix}\overline{Q}_{44} & \overline{Q}_{45}\\ \overline{Q}_{45} & \overline{Q}_{55}\end{bmatrix} \begin{Bmatrix}\gamma_{xz}\\ \gamma_{yz}\end{Bmatrix} = \overline{\mathbf{Q}}_n\,\boldsymbol{\gamma}\end{aligned} \tag{3.28}$$

Recalling from Section 2.1 the expression of the virtual internal work, it is possible to carry out the integration along the thickness, turning the integral over the volume into a surface integral:

$$\begin{aligned}\delta W_p &= \int_S \int_t \left(\delta\boldsymbol{\varepsilon}^{0T} + z\,\delta\mathbf{k}^T\right)\boldsymbol{\sigma}\,dz\,dS + \int_S \int_t \delta\boldsymbol{\gamma}^T\boldsymbol{\tau}\,dz\,dS\\ &= \int_S \delta\boldsymbol{\varepsilon}^{0T}\,\mathbf{N}\,dS + \int_S \delta\mathbf{k}^T\,\mathbf{M}\,dS + \int_S \delta\boldsymbol{\gamma}^T\,\mathbf{V}\,dS\end{aligned} \tag{3.29}$$

where the quantities $\mathbf{N} = \{N_{xx}\,, N_{yy}\,, N_{xy}\}^T$, $\mathbf{V} = \{V_{xz}\,, V_{yz}\}^T$ and $\mathbf{M} = \{M_{xx}\,, M_{yy}\,, M_{xy}\}^T$ are called in-plane force resultants, shear force resultants and moment resultants respectively. They are forces and moments per unit length. Introducing the linear constitutive relation in Eq. 3.28 and considering a composite laminate made by N plies with different direction of orthotropy, it is possible to introduce the laminate stiffness matrices $(\mathbf{A}\,, \mathbf{B}\,, \mathbf{D}\,, \mathbf{A}_n\,)$:

$$\begin{aligned}\mathbf{N} &= \int_t \boldsymbol{\sigma}\,dz = \sum_{k=1}^{N}\int_{t_k}^{t_{k+1}} \overline{\mathbf{Q}}_k\,dz\,\boldsymbol{\varepsilon}^0 + \sum_{k=1}^{N}\int_{t_k}^{t_{k+1}} z\,\overline{\mathbf{Q}}_k\,dz\,\mathbf{k} = \mathbf{A}\,\boldsymbol{\varepsilon}^0 + \mathbf{B}\,\mathbf{k}\\ \mathbf{M} &= \int_t z\,\boldsymbol{\sigma}\,dz = \sum_{k=1}^{N}\int_{t_k}^{t_{k+1}} z\,\overline{\mathbf{Q}}_k\,dz\,\boldsymbol{\varepsilon}^0 + \sum_{k=1}^{N}\int_{t_k}^{t_{k+1}} z^2\,\overline{\mathbf{Q}}_k\,dz\,\mathbf{k} = \mathbf{B}\,\boldsymbol{\varepsilon}^0 + \mathbf{D}\,\mathbf{k}\\ \mathbf{V} &= \int_t \boldsymbol{\tau}\,dz = \sum_{k=1}^{N}\int_{t_k}^{t_{k+1}} K_p\,\overline{\mathbf{Q}}_{n_k}\,dz\,\boldsymbol{\gamma} = \mathbf{A}_n\,\boldsymbol{\gamma}\end{aligned} \tag{3.30}$$

where K_p is the shear factor. The linearization of the internal virtual work, see Eq. 3.29, can be performed by observing that:

$$\partial\delta\boldsymbol{\varepsilon} = \partial\left(\delta\boldsymbol{\varepsilon}_l^0 + \delta\boldsymbol{\varepsilon}_{nl}^0 + z\,\delta\mathbf{k}\right) = \partial\delta\boldsymbol{\varepsilon}_{nl}^0 = \begin{Bmatrix} \frac{\partial w}{\partial x}\frac{\partial \delta w}{\partial x} \\ \frac{\partial w}{\partial y}\frac{\partial \delta w}{\partial y} \\ \frac{\partial w}{\partial x}\frac{\partial \delta w}{\partial y} + \frac{\partial w}{\partial y}\frac{\partial \delta w}{\partial x} \end{Bmatrix} \tag{3.31}$$

Referring to Eq. 3.31 and making use of the laminate constitutive equation, the virtual internal work for a composite laminated plate can be written as:

$$\begin{aligned} \delta W_p = &\int_S \begin{Bmatrix} \delta\boldsymbol{\varepsilon}_l^0 \\ \delta\mathbf{k} \\ \delta\boldsymbol{\gamma} \end{Bmatrix}^T \begin{bmatrix} \mathbf{A} & \mathbf{B} & \mathbf{0} \\ \mathbf{B} & \mathbf{D} & \mathbf{0} \\ \mathbf{0} & \mathbf{0} & \mathbf{A}_n \end{bmatrix} \begin{Bmatrix} \boldsymbol{\varepsilon}_l^0 \\ \mathbf{k} \\ \boldsymbol{\gamma} \end{Bmatrix} dS \\ &+ \int_S \begin{Bmatrix} \delta w_{/x} \\ \delta w_{/y} \end{Bmatrix}^T \begin{bmatrix} N_{xx}^0 & N_{xy}^0 \\ N_{xy}^0 & N_{yy}^0 \end{bmatrix} \begin{Bmatrix} w_{/x} \\ w_{/y} \end{Bmatrix} dS \end{aligned} \tag{3.32}$$

where $N_{\alpha\beta}^0$ represents a prestress contribute. Collecting all the unknowns in the vector $\mathbf{q}_p = \begin{Bmatrix} \mathbf{u}_p^0 \\ \boldsymbol{\theta}_p \end{Bmatrix}$ it is possible to write:

$$\delta W_p = \int_S \Big(\boldsymbol{\mathcal{B}}_1\delta\mathbf{q}_p\Big)^T \mathbf{D}_p \Big(\boldsymbol{\mathcal{B}}_1\mathbf{q}_p\Big)\, dS + \int_S \Big(\boldsymbol{\mathcal{B}}_2\delta\mathbf{q}_p\Big)^T \begin{bmatrix} N_{xx}^0 & N_{xy}^0 \\ N_{xy}^0 & N_{yy}^0 \end{bmatrix} \Big(\boldsymbol{\mathcal{B}}_2\mathbf{q}_p\Big)\, dS \tag{3.33}$$

where $\boldsymbol{\mathcal{B}}_1$ and $\boldsymbol{\mathcal{B}}_2$ are differential operators through which it is possible to obtain strain parameters from displacement and rotation fields. They are

defined as:

$$\boldsymbol{\mathcal{B}}_1 = \begin{bmatrix} \frac{\partial}{\partial x} & 0 & 0 & 0 & 0 & 0 \\ 0 & \frac{\partial}{\partial y} & 0 & 0 & 0 & 0 \\ \frac{\partial}{\partial y} & \frac{\partial}{\partial x} & 0 & 0 & 0 & 0 \\ 0 & 0 & 0 & \frac{\partial}{\partial x} & 0 & 0 \\ 0 & 0 & 0 & 0 & \frac{\partial}{\partial y} & 0 \\ 0 & 0 & \frac{\partial}{\partial x} & 1 & 0 & 0 \\ 0 & 0 & \frac{\partial}{\partial y} & 0 & 1 & 0 \end{bmatrix}, \qquad \boldsymbol{\mathcal{B}}_2 = \begin{bmatrix} 0 & 0 & \frac{\partial}{\partial x} & 0 & 0 & 0 \\ 0 & 0 & \frac{\partial}{\partial y} & 0 & 0 & 0 \end{bmatrix} \tag{3.34}$$

The virtual work of the inertial forces is similarly treated. Since the displacements of every point of the plate depend linearly on the thickness, it is possible to carry out the integration along direction z:

$$\begin{aligned} \delta U_p &= \int_\Omega \left(\delta \mathbf{u}_p^0 + z\,\mathbf{L}\,\delta\boldsymbol{\theta}_p\right)^T \rho_0 \left(\ddot{\mathbf{u}}_p^0 + z\,\mathbf{L}\,\ddot{\boldsymbol{\theta}}_p\right) d\Omega \\ &= \int_S \begin{Bmatrix} \delta \mathbf{u}_p^0 \\ \delta\boldsymbol{\theta}_p \end{Bmatrix}^T \int_{-h/2}^{h/2} \rho_0 \begin{bmatrix} \mathbf{I} & z\,\mathbf{L} \\ z\,\mathbf{L} & z^2\,\mathbf{L} \end{bmatrix} dz \begin{Bmatrix} \mathbf{u}_p^0 \\ \boldsymbol{\theta}_p \end{Bmatrix} dx\,dy \\ &= \int_S \delta\mathbf{q}_p^T\,\overline{\mathbf{M}}_p\,\ddot{\mathbf{q}}_p\,dx\,dy \end{aligned} \tag{3.35}$$

Considering homogeneously distributed density, components of matrix $\overline{\mathbf{M}}_p$ are:

$$\overline{\mathbf{M}}_p = \rho_0 \begin{bmatrix} h & 0 & 0 & 0 & 0 & 0 \\ 0 & h & 0 & 0 & 0 & 0 \\ 0 & 0 & h & 0 & 0 & 0 \\ 0 & 0 & 0 & \frac{h^3}{12} & 0 & 0 \\ 0 & 0 & 0 & 0 & \frac{h^3}{12} & 0 \\ 0 & 0 & 0 & 0 & 0 & 0 \end{bmatrix} \tag{3.36}$$

The external load are assumed in the form of the in-plane loads $\mathbf{P} = \begin{Bmatrix} P_x & P_y \end{Bmatrix}^T$, forces per unit length acting along the plate edges, and the distributed pressure p on the surface of the plate. The external virtual work can be written

as:

$$\delta V_p = \int_{\partial S} \begin{Bmatrix} \delta u^0 \\ \delta v^0 \end{Bmatrix}^T \begin{Bmatrix} P_x \\ P_y \end{Bmatrix} d\partial S + \int_S \delta w^0 \, p \, dS \tag{3.37}$$

3.2.2 Ritz approximation

In the present work Legendre Polynomials are chosen as Ritz functions. This class of one-dimensional functions is made by the solutions $\varphi_n(x)$ to Legendre's differential equation and can be expressed as [27]:

$$\varphi_n(x) = \frac{1}{2n!} \frac{d^n}{dx^n} \left(x^2 - 1\right)^n \tag{3.38}$$

It can be demonstrated that these are orthogonal function with respect to the L^2 inner product in the interval $-1 < x < 1$:

$$\int_{-1}^{1} \varphi_m(x) \varphi_n(x) \, dx = \frac{2}{2n+1} \delta_{mn} \tag{3.39}$$

where δ_{mn} is the Kronecker delta (equal to 1 if $m = n$, 0 otherwise). By using Legendre polynomials the components of the displacement and virtual displacement fields, are defined in the 2D domain $S_0 = [-1\,,1] \times [-1\,,1]$, which is linked to the physical domain through the bilinear mapping:

$$\begin{Bmatrix} x \\ y \end{Bmatrix} = \boldsymbol{F}(\xi, \eta) \tag{3.40}$$

where ξ and η are the dimensionless coordinates. In the simple case of rectangular plates (which are considered in this work) it can be expressed as:

$$\begin{Bmatrix} x \\ y \end{Bmatrix} = \begin{bmatrix} a/2 & 0 \\ 0 & b/2 \end{bmatrix} \begin{Bmatrix} \xi \\ \eta \end{Bmatrix} \tag{3.41}$$

where a and b are the planar dimensions of the plate. The Jacobian of the

transformation is simply $J = (ab)/4$, while the derivative operators are linked by the following expression:

$$\begin{Bmatrix} \frac{\partial}{\partial x} \\ \frac{\partial}{\partial y} \end{Bmatrix} = \begin{bmatrix} 2/a & 0 \\ 0 & 2/b \end{bmatrix} \begin{Bmatrix} \frac{\partial}{\partial \xi} \\ \frac{\partial}{\partial \eta} \end{Bmatrix} \tag{3.42}$$

The generic unknown component f is then written as [28]:

$$f(\xi,\eta) = g_f(\xi,\eta) \sum_{r=0}^{R} \sum_{s=0}^{S} \varphi_r(\xi)\, \varphi_s(\eta)\, C_{rs}^f \tag{3.43}$$

being $\varphi_r(\xi)$ the r^{th} Legendre polynomial of order r, C_{rs}^f are the unknown Ritz coefficients and $g_f(\xi,\eta)$ a function that guarantees the fulfillment of the essential boundary conditions (as shown in Figure 3.3), defined as:

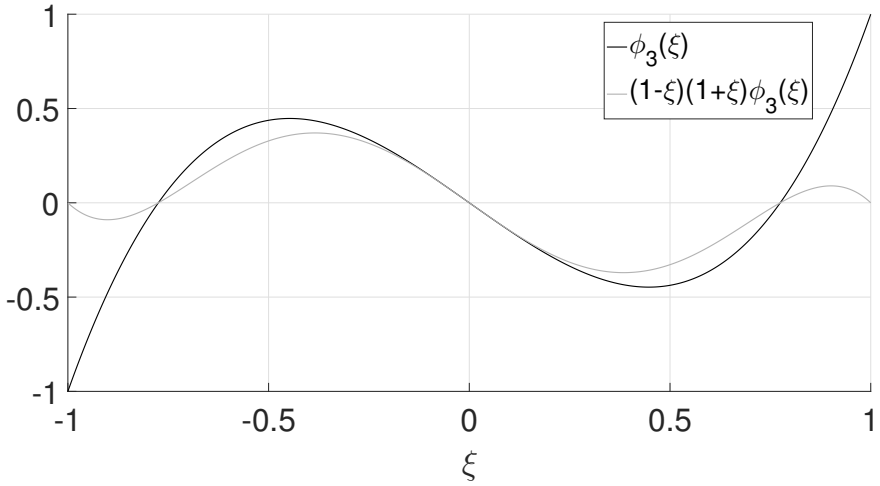

Figure 3.3: Ritz function based on third order Legendre polynomial, with free and fixed ends.

$$g_f(\xi,\eta) = (1-\xi)^{\gamma_1}(1+\xi)^{\gamma_2}(1-\eta)^{\gamma_3}(1+\eta)^{\gamma_4} \tag{3.44}$$

where the terms γ_i can take values 0 or 1 according to the condition prescribed on each edge ($\xi = \pm 1$) and ($\eta = \pm 1$), as shown in Table 3.1. Aiming

edge	free	fixed
$\xi = +1$	$\gamma_1 = 0$	$\gamma_1 = 1$
$\xi = -1$	$\gamma_2 = 0$	$\gamma_2 = 1$
$\eta = +1$	$\gamma_3 = 0$	$\gamma_3 = 1$
$\eta = -1$	$\gamma_4 = 0$	$\gamma_4 = 1$

Table 3.1: Values of the exponents in equation 3.44.

at simplifying the notation, the vectors $\boldsymbol{\varphi_r}(\xi) = \left\{\varphi_0(\xi) \quad ... \quad \varphi_R(\xi)\right\}^T$ and $\mathbf{c}_f = \left\{C^f_{00} \quad C^f_{01} \quad ... \quad C^f_{RS}\right\}^T$ are introduced, then Eq. 3.43 can be written as:

$$f(\xi,\eta) = g_f(\xi,\eta)\left(\boldsymbol{\varphi_r}(\xi) \otimes \boldsymbol{\varphi_s}(\eta)\right)^T \mathbf{c}_f = \boldsymbol{\phi}^T_f(\xi,\eta)\,\mathbf{c}_f \tag{3.45}$$

where the symbol "$\otimes$" identifies the Kronecker product. The formalism can be extended to the approximation of fields $\mathbf{u}^0_p$ and $\boldsymbol{\theta}_p$ (the same notation can be straightforwardly applied to the virtual field $\delta\mathbf{u}^0_p$ and $\delta\boldsymbol{\theta}_p$):

$$\begin{aligned}
\mathbf{u}^0_p &= \begin{bmatrix} \boldsymbol{\phi}^T_u(\xi,\eta) & \mathbf{0} & \mathbf{0} \\ \mathbf{0} & \boldsymbol{\phi}^T_v(\xi,\eta) & \mathbf{0} \\ \mathbf{0} & \mathbf{0} & \boldsymbol{\phi}^T_w(\xi,\eta) \end{bmatrix} \begin{Bmatrix} \mathbf{c}_u \\ \mathbf{c}_v \\ \mathbf{c}_w \end{Bmatrix} = \boldsymbol{\Phi}_u(\xi,\eta)\,\mathbf{c}^u_p \\
\boldsymbol{\theta}_p &= \begin{bmatrix} \boldsymbol{\phi}^T_{\theta_x}(\xi,\eta) & \mathbf{0} & \mathbf{0} \\ \mathbf{0} & \boldsymbol{\phi}^T_{\theta_y}(\xi,\eta) & \mathbf{0} \\ \mathbf{0} & \mathbf{0} & \boldsymbol{\phi}^T_{\theta_z}(\xi,\eta) \end{bmatrix} \begin{Bmatrix} \mathbf{c}_{\theta_x} \\ \mathbf{c}_{\theta_y} \\ \mathbf{c}_{\theta_z} \end{Bmatrix} = \boldsymbol{\Phi}_\theta(\xi,\eta)\,\mathbf{c}^\theta_p
\end{aligned} \tag{3.46}$$

and simplifying the notation:

$$\mathbf{q}_p = \begin{bmatrix} \boldsymbol{\Phi}_u(\xi,\eta) & \mathbf{0} \\ \mathbf{0} & \boldsymbol{\Phi}_\theta(\xi,\eta) \end{bmatrix} \begin{Bmatrix} \mathbf{a}^u_p \\ \mathbf{a}^\theta_p \end{Bmatrix} = \boldsymbol{\Phi}(\xi,\eta)\,\mathbf{a}_p \tag{3.47}$$

Substituting equation 3.47 into 3.32, the discretized virtual internal work can

be written as:

$$\begin{aligned}\delta W_p &= \delta \mathbf{a}_p^T \int_{-1}^{1}\int_{-1}^{1} \Big(\boldsymbol{\mathcal{B}}_1\Phi(\xi,\eta)\Big)^T \mathbf{D}_p \Big(\boldsymbol{\mathcal{B}}_1\Phi(\xi,\eta)\Big)\, J\, d\xi\, d\eta\, \mathbf{a}_p \\ &+ \delta \mathbf{a}_p^T \int_{-1}^{1} \Big(\boldsymbol{\mathcal{B}}_2\Phi(\xi,\eta)\Big)^T \begin{bmatrix} N^0_{xx} & N^0_{xy} \\ N^0_{xy} & N^0_{yy} \end{bmatrix} \Big(\boldsymbol{\mathcal{B}}_2\Phi(\xi,\eta)\Big)\, J\, d\xi\, d\eta\, \mathbf{a}_p \\ &= \delta \mathbf{a}_p^T \mathbf{K}_p\, \mathbf{a}_p + \delta \mathbf{a}_p^T \mathbf{K}_{pG}\, \mathbf{a}_p\end{aligned} \tag{3.48}$$

The derivatives about the physical coordinates $(x\,, y)$, involved by $\boldsymbol{\mathcal{B}}_1$ and $\boldsymbol{\mathcal{B}}_2$, can be computed using relation 3.42. The same approach is applied to discretize the virtual work done by inertial and external forces:

$$\begin{aligned}\delta U_p + \delta V_p &= \delta \mathbf{a}_p^T \int_{-1}^{1}\int_{-1}^{1} \boldsymbol{\Phi}(\xi,\eta)^T \overline{\mathbf{M}}_p\, \boldsymbol{\Phi}(\xi,\eta)\, J\, d\xi\, d\eta\, \ddot{\mathbf{a}}_p \\ &- \delta \mathbf{a}_p^T \int_{-1}^{1} \Big(\boldsymbol{\Phi}(-1,\,\eta)^T\, \mathbf{p}_1 + \boldsymbol{\Phi}(+1,\,\eta)^T\, \mathbf{p}_3\Big) \frac{a}{2}\, d\xi \\ &- \delta \mathbf{a}_p^T \int_{-1}^{1} \Big(\boldsymbol{\Phi}(\xi,\,-1)^T\, \mathbf{p}_2 + \boldsymbol{\Phi}(\xi,\,+1)^T\, \mathbf{p}_4\Big) \frac{b}{2}\, d\eta \\ &- \delta a_w^T \int_{-1}^{1}\int_{-1}^{1} p\, \phi_w(\xi,\eta)\, J\, d\xi\, d\eta \\ &= \delta \mathbf{a}^T \mathbf{M}_p\, \ddot{\mathbf{a}} - \delta \mathbf{a}^T \mathbf{P}_p\end{aligned} \tag{3.49}$$

where $\mathbf{p}_i$ represents the loads per unit length acting on the i-th edge. Computation of the integrals in equations (3.48 and 3.49) can be performed analytically. In this context, an efficient way to perform this operation is presented in reference [29].

3.3 Stiffener model

3.3.1 Path parametrisation

The first element to obtain the mathematical model of the stiffener is its geometrical description. As discussed later, the stiffener is modelled as a mono-dimensional element and its geometry can be fully described using its reference line which draws a curve on the 2D domain of the plate. This curve can be described by a vector function defining the position of its points $\mathbf{r} = \{ x , y , z \}$ depending on a parameter ζ:

$$\mathbf{r} : (\zeta_i , \zeta_f) \subset \mathbb{R} \rightarrow \mathbb{R}^3 \tag{3.50}$$

This function represents the parametrization of the stiffener path. For example, the plot of the cubic function $y = x^3$ is a curve on the (x, y) domain, and can be parametrized in the following way:

$$\begin{aligned} x(\zeta) &= \zeta \\ y(\zeta) &= \zeta^3 \end{aligned} \tag{3.51}$$

A requirement on the regularity of the parametrisation is that $\mathbf{r}(\zeta) \in C^1(\zeta_i , \zeta_f)$. This means that the variation of coordinates (x, y) with the parameter ζ has to be sufficiently regular to avoid paths characterized by a discontinuity of the first derivative, an example of which is provided in Figure 3.4b.
The parametrisation permits to define the tangent vector $\mathbf{t}$:

$$\mathbf{t}(\zeta) = \mathbf{r}'(\zeta) = \begin{Bmatrix} x'(\zeta) \\ y'(\zeta) \end{Bmatrix} \tag{3.52}$$

where the notation $(\bullet)'$ represents the derivative with respect to the parameter ζ. As shown in Figure 3.5, $\mathbf{t}$ is a vector applied in the point $\mathbf{r}(\zeta)$ and tangent to the curve. Its magnitude can vary from point to point along the curve and depends on the parametrization used. An interpretation of the quantities involved in the description of the stiffener path is given by the

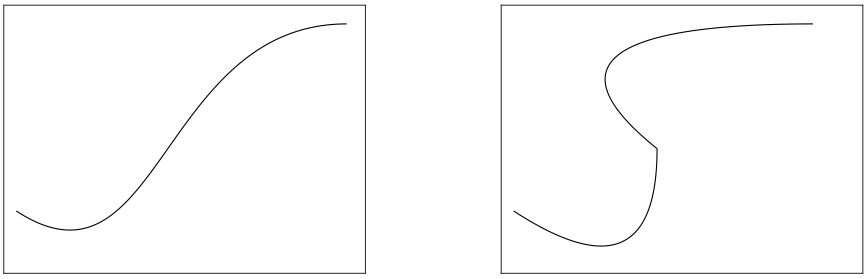

(a) **(b)**

Figure 3.4: Requirement on the regularity of the parametrization. The curve in **(b)** is not enough regular.

analogy - used throughout this section for clarity purposes - with the trajectory of a material point in the space, where ζ is in analogy with the time t. For instance, the tangent vector can be seen as the velocity of a particle moving along the curve at the time instant ζ. Using this interpretation it is intuitive to define the length of the curve as the distance covered by the particle at a velocity of magnitude $\left\|\mathbf{t}(\zeta)\right\|$ between the two time instants $(\zeta_i\,,\zeta_f)$:

$$\Gamma = \int_{\zeta_i}^{\zeta_f} \left\|\mathbf{t}(\zeta)\right\| d\zeta \tag{3.53}$$

There exist a particular parametrization which uses the so called arc length parameter s, that makes $\left\|\mathbf{t}(\zeta)\right\| = 1$ for each point along the curve. It follows that in this case the length of the curve is simply computed as:

$$\Gamma = \int_{s_i}^{s_f} ds = s_f - s_i \tag{3.54}$$

where s_f and s_i are initial and final values of the arc length parameter. It can be noted that the relation between parameter s and ζ is of the same nature as that between coordinates $(x\,,y)$ and $(\xi\,,\eta)$. While s is a curvilinear coordinate of a physical domain, ζ is defined on a local domain. The Jacobian of the transformation is $J_s = \left\|\mathbf{t}(\zeta)\right\|$. A common practice is to normalize the tangent vector so that $\mathbf{t}(\zeta)$ and $\mathbf{t}(s)$ represent the same quantity:

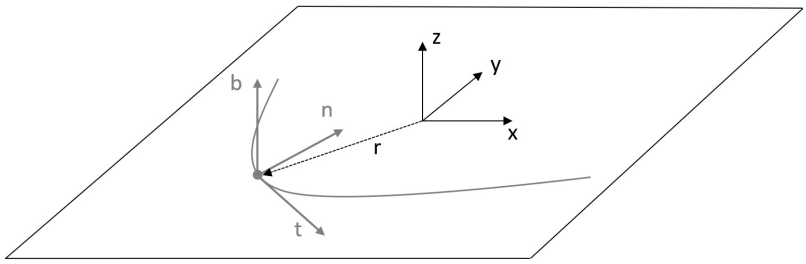

Figure 3.5: Definition of the curve based reference frame.

$$\mathbf{t}(\zeta) = \frac{\mathbf{r}'(\zeta)}{\left\|\mathbf{r}'(\zeta)\right\|} \qquad \text{or} \qquad \mathbf{t}(s) = \mathbf{r}'(s) \tag{3.55}$$

An orthonormal, curve-based, reference frame has to be introduced to describe the displacement field of the stiffener. Tangent vector is the first element of such frame. A normal vector $\mathbf{n}$ can be introduced, and its definition can be physically interpreted as the centripetal acceleration of the aforementioned particle:

$$\mathbf{n}(s) = \frac{\mathbf{r}''(s)}{\left\|\mathbf{r}''(s)\right\|} \tag{3.56}$$

where the normalization is required to have a reference frame composed by unit vectors. The normalization factor $\kappa(s) = \left\|\mathbf{r}''(s)\right\|$ is known as *geometric curvature* which measures the rate of change of the tangent vector direction. The third vector is necessarily obtained through the cross product between the other two:

$$\mathbf{b}(s) = \mathbf{t}(s) \wedge \mathbf{n}(s) \tag{3.57}$$

Normal and binormal vectors can be defined using the general parameter ζ through the following relations:

$$\begin{aligned} \mathbf{b}(\zeta) &= \frac{\mathbf{r}'(\zeta) \wedge \mathbf{r}''(\zeta)}{\left\|\mathbf{r}'(\zeta) \wedge \mathbf{r}''(\zeta)\right\|} \\ \mathbf{n}(\zeta) &= \mathbf{b}(\zeta) \wedge \mathbf{t}(\zeta) \end{aligned} \tag{3.58}$$

The reference frame composed by unit vectors ($\mathbf{t}$, $\mathbf{n}$,$\mathbf{b}$), is known as Frènet frame and it is described in Figure 3.5. To underline its dependency on the point of the curve it is often called "moving" frame, reminding the analogy of the moving particle. The variation of the unit vectors along the curve is governed by the Frènet formulas:

$$\begin{aligned} \mathbf{t}'(s) &= \quad \kappa(s)\,\mathbf{n}(s) \\ \mathbf{n}'(s) &= -\kappa(s)\,\mathbf{t}(s) + \tau(s)\,\mathbf{b}(s) \\ \mathbf{b}'(s) &= -\tau(s)\,\mathbf{n}(s) \end{aligned} \tag{3.59}$$

where $\kappa(s)$ is the defined curvature parameter and $\tau(s)$ the torsion of the curve, which are positive quantities. This relations are very important when it comes to compute the derivative about s of a quantity described in the curve based frame (e.g. for velocity or strain fields). They are valid for a generic curve in the 3D space. For plane curves a possibility is to use this general relations considering $\tau(\zeta) = 0$; in this case the binormal unit vector is constant and the curve lies on a plane. However this is not the best way to proceed. To give a better understanding of the problem consider Figure 3.6a, representing the cubic $y = x^3$. The normal unit vector, as it is defined in Eq. 3.56, always points in the centripetal direction; when the curvature sign changes the normal unit vector undergoes a reversal, thus a discontinuous variation; the binormal vector suffers the same fate facing upwards or downward depending on the sign of the curvature. This leads to evident issues related to the definition of the displacement field along the curve. Another problem occurs when the curve is reduced to a straight line or presents inflection points. In these situations the curvature $\kappa(s)$ is null and and the normal vector cannot be defined[4]. A more reliable definition of the curve based frame is presented in [30] and, to some extent, makes the computations any easier. For these reasons, this approach is adopted here. Thanks to the restriction to plane curves it is possible to obtain the couple $\{\mathbf{t}\,,\mathbf{n}\}$ from the couple $\{\mathbf{e}_1\,,\mathbf{e}_2\}$ of the plate reference frame, simply through

[4]The denominator in the definition of $\mathbf{n}(s)$ in 3.56 has to be different from zero. In this case the curve is said to be *strongly regular*.

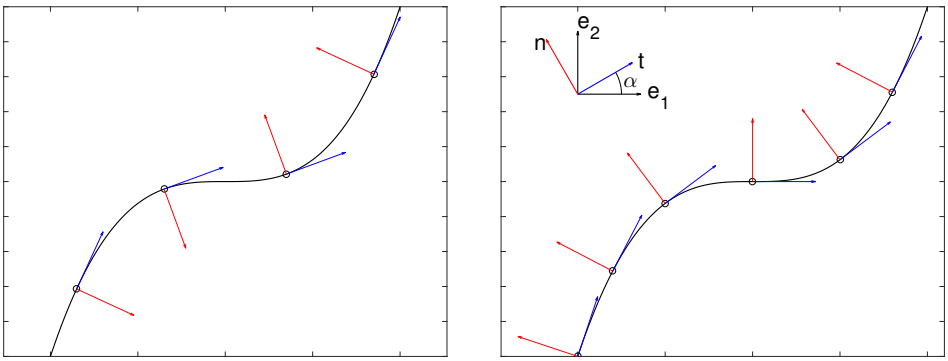

Figure 3.6: Comparison between curve based frame definitions

a rotation[5] of an angle α. Once the tangent vector is computed as in Eq. 3.55, the normal vector is obtained rotating anticlockwise the latter by $\pi/2$. In this way the binormal vector always face upwards (i.e. in the positive direction of thickness coordinate z, which is also the axis of rotation).

$$\mathbf{t}(s) = \begin{Bmatrix} \cos\alpha(s) \\ \sin\alpha(s) \\ 0 \end{Bmatrix} \quad , \quad \mathbf{n}(s) = \begin{Bmatrix} -\sin\alpha(s) \\ \cos\alpha(s) \\ 0 \end{Bmatrix} \quad , \quad \mathbf{b}(s) = \begin{Bmatrix} 0 \\ 0 \\ 1 \end{Bmatrix} \tag{3.60}$$

It is worth noting that now $\mathbf{n}$ does not depend on $\mathbf{r}''$. Computing the derivative about s, the Frénet formulas can be restored:

$$\begin{aligned} \mathbf{t}'(s) &= \begin{Bmatrix} -\sin\alpha(s)\alpha'(s) \\ \cos\alpha(s)\alpha'(s) \\ 0 \end{Bmatrix} = \kappa(s)\mathbf{n}(s) \\ \mathbf{n}'(s) &= \begin{Bmatrix} -\cos\alpha(s)\alpha'(s) \\ -\sin\alpha(s)\alpha'(s) \\ 0 \end{Bmatrix} = -\kappa(s)\mathbf{t}(s) \\ \mathbf{b}'(s) &= \mathbf{0} \end{aligned} \tag{3.61}$$

[5] And a traslation since the curve based frame is a moving frame.

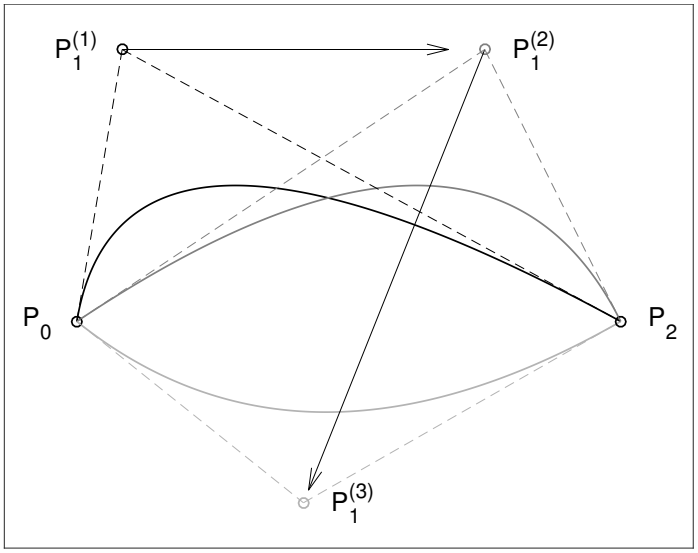

Figure 3.7: Curve path variations changing the position of control point $\mathbf{P}_1$.

where the curvature is now defined as $\kappa(s) = \alpha'(s)$, and it can take positive or negative values. In Figure 3.6b is reported the new situation. The only requirement is that the tangent vector varies with continuity and the normal vector is defined accordingly no matter the sign of the curvature; consequently inflection points or straight lines do not cause any problem as they are included in the theory. The type of parametric curves used in this work is widely adopted in computer graphics and it's based on the Bézier curves; their general definition is [31]:

$$\mathbf{r}(\mu) = \sum_{i=0}^{n} \mathbf{P}_i \binom{n}{i} \mu^i \left(1-\mu\right)^{n-1} \ , \qquad \mu \in [0\,,1] \tag{3.62}$$

where n is the order of the curve and $\mathbf{P}_i = \{x_{P_i}\,, y_{P_i}\,, z_{P_i}\}^T$, are the control points. These curves are very convenient for the purposes of the present work as it is possible to change the path of the stringer by merely changing the position of the control points. In Figure 3.7 it's shown the changing of the curve path with the position of control point $\mathbf{P}_1$. In this work, curves of the 2^{nd} and 3^{rd} order are considered, and their Bézier parametrization is now

reported in extended form:

$$
\begin{aligned}
2^{nd}\ order: \quad & \mathbf{r}(\zeta) = \frac{1}{2}(1-\zeta)^2\,\mathbf{P}_0 + 2\zeta\,(1-\zeta)\,\mathbf{P}_1 + \frac{1}{4}(1+\zeta)^2\,\mathbf{P}_2 \\
3^{rd}\ order: \quad & \mathbf{r}(\zeta) = \left(\frac{1}{2}-\frac{1}{2}\zeta\right)^3\mathbf{P}_0 + \frac{3}{2}(1+\zeta)\left(\frac{1}{2}-\frac{1}{2}\zeta\right)^2\mathbf{P}_1 \\
& \qquad + \frac{3}{2}(1+\zeta)^2\left(\frac{1}{2}-\frac{1}{2}\zeta\right)\mathbf{P}_2 + \left(\frac{1}{2}+\frac{1}{2}\zeta\right)^3\mathbf{P}_3 \\
& \qquad\qquad\qquad\qquad\qquad\qquad\qquad\qquad\qquad\qquad with \quad \zeta \in [-1\,,1]
\end{aligned}
\tag{3.63}
$$

Note that now the parameter takes values in $[-1\,,1]$, due to the application of the transformation $\zeta = 2\mu - 1$: as described in the following, this transformation is convenient for the implementation of Gauss integration rules.

3.3.2 Kinematics

The formulation adopted for the description of the beam displacement field is based on the Timoshenko hypotheses: the cross section is not constrained to stay perpendicular to the beam reference axis, as is the case of the Euler-Bernoulli beam theory, but can rotate according to the unknown quantities θ_n and θ_b, where the subscript identifies the axis of rotation. Moreover the dependence on the the cross section coordinates is imposed to be linear (just as in FSDT the displacement field varies linearly along the thickness). The displacement of every point in the cross section is then fully described by the linear displacements and rotations of the reference line:

$$
\mathbf{u}_s = \mathbf{u}_s^0 + (\mathbf{d}\times)^T\boldsymbol{\theta}_s \tag{3.64}
$$

with:

$$
\begin{aligned}
\mathbf{u}_s^0 &= u_t^0\,\mathbf{t} + v_n^0\,\mathbf{n} + w_b^0\,\mathbf{b} \\
\boldsymbol{\theta}_s &= \theta_t\,\mathbf{t} + \theta_n\,\mathbf{n} + \theta_b\,\mathbf{b} \\
\mathbf{d} &= 0\,\mathbf{t} + n\,\mathbf{n} + b\,\mathbf{b}
\end{aligned}
\tag{3.65}
$$

A schematic representation of the beam is reported in Figure 3.8, along with

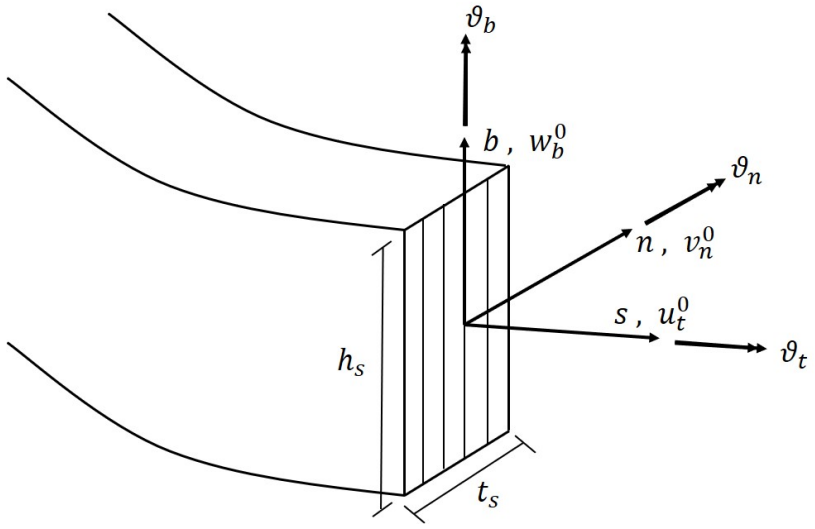

Figure 3.8: Definition of curvilinear coordinate system and beam displacement field.

the dimensions and the kinematic parameters. In this model three relevant strain components are present: the axial (ε_t) and two transversal shear strains (γ_n, γ_b) acting on the cross section plane. All the other components don't produce any energy contribute as the stresses energetically conjugated are equal to zero for the beam state of stress hypothesis. The strain tensor components of interest can be written as described in reference [32] [6]:

$$\begin{aligned}
\varepsilon_t &= \frac{\partial \mathbf{u}_s}{\partial s} \cdot \mathbf{t} + \frac{1}{2}\left(\frac{\partial w_b^0}{\partial s}\right)^2 \\
\gamma_n &= \frac{\partial \mathbf{u}_s}{\partial n} \cdot \mathbf{t} + \frac{\partial \mathbf{u}_s}{\partial s} \cdot \mathbf{n} \\
\gamma_b &= \frac{\partial \mathbf{u}_s}{\partial b} \cdot \mathbf{t} + \frac{\partial \mathbf{u}_s}{\partial s} \cdot \mathbf{b}
\end{aligned} \tag{3.66}$$

where the second term of the first relation comes from the hypothesis on the non-linear part of the Green-Lagrange strain tensor: in a similar way to plate

[6] In this article the strain components come from the *small strain tensor*, as the authors don't take into consideration the potential presence of a prestress in the linear static analysis of curved beams. Here a non-linear contribute has been added in order to perform the linear buckling analysis.

theory, the only source of non-linearities are the quadratic terms related to the variation of the transversal displacement w_b along the curvilinear coordinate. Theoretically this term should contain also the torsional rotation θ_t, but its contribute is considered negligible with respect to the adopted level of accuracy of the model. The derivatives of $\mathbf{u}_s$ along the coordinates $(s\,,n\,,b)$ lead to:

$$\begin{aligned}
\frac{\partial \mathbf{u}_s}{\partial s} &= \frac{\partial \mathbf{u}_s^0}{\partial s} + (\mathbf{d}\times)^T \frac{\partial \boldsymbol{\theta}_s}{\partial s} \\
\frac{\partial \mathbf{u}_s}{\partial n} &= \left(\frac{\partial \mathbf{d}}{\partial n}\times\right)^T \boldsymbol{\theta}_s = -\theta_b\,\mathbf{t} + \theta_t\,\mathbf{b} \\
\frac{\partial \mathbf{u}_s}{\partial b} &= \left(\frac{\partial \mathbf{d}}{\partial b}\times\right)^T \boldsymbol{\theta}_s = \theta_n\,\mathbf{t} - \theta_t\,\mathbf{b}
\end{aligned} \tag{3.67}$$

The first relation in 3.67 needs particular care as the component of displacement and rotation vectors, which are functions of s, are expressed in a "moving" frame, which depends on the arc length parameter as well:

$$\begin{aligned}
\frac{\partial \mathbf{u}_s^0}{\partial s} &= \frac{\partial u_t^0}{\partial s}\,\mathbf{t} + u_t^0\,\frac{\partial \mathbf{t}}{\partial s} + \frac{\partial v_n^0}{\partial s}\,\mathbf{n} + v_n^0\,\frac{\partial \mathbf{n}}{\partial s} + \frac{\partial w_b^0}{\partial s}\,\mathbf{b} + w_b^0\,\frac{\partial \mathbf{b}}{\partial s} \\
&= \left(\frac{\partial u_t^0}{\partial s} - \kappa(s)\,v_n^0\right)\,\mathbf{t} + \left(\frac{\partial v_n^0}{\partial s} + \kappa(s)\,u_t^0\right)\,\mathbf{n} + \frac{\partial w_b^0}{\partial s}\,\mathbf{b} \\
\frac{\partial \boldsymbol{\theta}_s^0}{\partial s} &= \frac{\partial \theta_t}{\partial s}\,\mathbf{t} + \theta_t\,\frac{\partial \mathbf{t}}{\partial s} + \frac{\partial \theta_n}{\partial s}\,\mathbf{n} + \theta_n\,\frac{\partial \mathbf{n}}{\partial s} + \frac{\partial \theta_b}{\partial s}\,\mathbf{b} + \theta_b\,\frac{\partial \mathbf{b}}{\partial s} \\
&= \left(\frac{\partial \theta_t}{\partial s} - \kappa(s)\,\theta_n\right)\,\mathbf{t} + \left(\frac{\partial \theta_n}{\partial s} + \kappa(s)\,\theta_t\right)\,\mathbf{n} + \frac{\partial \theta_b}{\partial s}\,\mathbf{b}
\end{aligned} \tag{3.68}$$

where the Frénet formulas in Eq. 3.61 are used to solve the unit vectors derivative. The small strain tensor components can be written as:

$$\boldsymbol{\varepsilon_s} = \begin{Bmatrix} \varepsilon_t \\ \gamma_n \\ \gamma_b \end{Bmatrix} = \boldsymbol{\varepsilon_s^0} + (\mathbf{d}\times)^T \mathbf{k}_s = \begin{Bmatrix} \varepsilon_t^0 + b\,k_n - n\,k_b \\ \gamma_n^0 - b\,k_t \\ \gamma_b^0 + n\,k_t \end{Bmatrix} \tag{3.69}$$

where the definition of the six deformation parameters is obtained by substi-

tuting 3.67 in 3.66, and considering 3.68:

$$\boldsymbol{\varepsilon}_{\boldsymbol{s}}^{0} = \boldsymbol{\varepsilon}_{\boldsymbol{s}}^{l} + \boldsymbol{\varepsilon}_{\boldsymbol{s}}^{nl} = \begin{Bmatrix} \varepsilon_t^0 \\ \gamma_n^0 \\ \gamma_b^0 \end{Bmatrix} + \begin{Bmatrix} \varepsilon_t^{nl} \\ 0 \\ 0 \end{Bmatrix} = \begin{Bmatrix} \frac{\partial u_t^0}{\partial s} - \kappa(s)\, v_n^0 \\ \frac{\partial v_n^0}{\partial s} + \kappa(s)\, u_t^0 - \theta_b \\ \frac{\partial w_b^0}{\partial s} + \theta_n \end{Bmatrix} + \begin{Bmatrix} \frac{1}{2}\left(\frac{\partial w_b^0}{\partial s}\right)^2 \\ 0 \\ 0 \end{Bmatrix}$$

$$\mathbf{k}_s = \begin{Bmatrix} k_t \\ k_n \\ k_b \end{Bmatrix} = \begin{Bmatrix} \frac{\partial \theta_t}{\partial s} - \kappa(s)\, \theta_n \\ \frac{\partial \theta_n}{\partial s} + \kappa(s)\, \theta_t \\ \frac{\partial \theta_b}{\partial s} \end{Bmatrix} \tag{3.70}$$

As said previously, in this work only blade laminated stiffeners were considered; the lamination direction is taken perpendicular to that of the plate. The rotated constitutive law valid for a generic lamina can be written as:

$$\begin{bmatrix} \overline{Q}_{11} & \overline{Q}_{12} & \overline{Q}_{16} & 0 & 0 \\ \overline{Q}_{12} & \overline{Q}_{22} & \overline{Q}_{26} & 0 & 0 \\ \overline{Q}_{16} & \overline{Q}_{26} & \overline{Q}_{66} & 0 & 0 \\ 0 & 0 & 0 & \overline{Q}_{44} & \overline{Q}_{45} \\ 0 & 0 & 0 & \overline{Q}_{45} & \overline{Q}_{55} \end{bmatrix} \begin{Bmatrix} \varepsilon_t \\ \varepsilon_b \\ \gamma_b \\ \gamma_{bn} \\ \gamma_n \end{Bmatrix} = \begin{Bmatrix} \sigma_t \\ \sigma_b \\ \tau_b \\ \tau_{bn} \\ \tau_n \end{Bmatrix} \tag{3.71}$$

The state of stress comes from the beam hypotheses and besides the axial stress σ_t, it involves the two shear components, τ_n and τ_b, acting on the cross section plane; the other components (σ_b and τ_{bn}) are null. It is possible to separate the energetically active components from the others rearranging rows and columns in 3.71:

$$\left[\begin{array}{ccc:cc} \overline{Q}_{11} & 0 & \overline{Q}_{16} & \overline{Q}_{12} & 0 \\ 0 & \overline{Q}_{55} & 0 & 0 & \overline{Q}_{45} \\ \overline{Q}_{16} & 0 & \overline{Q}_{66} & \overline{Q}_{26} & 0 \\ \hdashline \overline{Q}_{12} & 0 & \overline{Q}_{26} & \overline{Q}_{22} & 0 \\ 0 & \overline{Q}_{45} & 0 & 0 & \overline{Q}_{44} \end{array}\right] \left\{\begin{array}{c} \varepsilon_t \\ \gamma_n \\ \gamma_b \\ \hdashline \varepsilon_b \\ \gamma_{bn} \end{array}\right\} = \left\{\begin{array}{c} \sigma_t \\ \tau_n \\ \tau_b \\ \hdashline 0 \\ 0 \end{array}\right\} \tag{3.72}$$

and in compact form:

$$\begin{bmatrix} \overline{\mathbf{Q}}_{\varepsilon\varepsilon} & \overline{\mathbf{Q}}_{\varepsilon\beta} \\ \overline{\mathbf{Q}}_{\varepsilon\beta}^{T} & \overline{\mathbf{Q}}_{\beta\beta} \end{bmatrix} \begin{Bmatrix} \boldsymbol{\varepsilon}_s \\ \boldsymbol{\beta} \end{Bmatrix} = \begin{Bmatrix} \boldsymbol{\sigma}_s \\ \mathbf{0} \end{Bmatrix} \tag{3.73}$$

At this point, statically condensing 3.73, it is possible to write the constitutive relation taking into consideration only the components contributing to the virtual internal work:

$$\boldsymbol{\sigma}_s = \left(\overline{\mathbf{Q}}_{\varepsilon\varepsilon} - \overline{\mathbf{Q}}_{\varepsilon\beta}\, \overline{\mathbf{Q}}_{\beta\beta}^{-1}\, \overline{\mathbf{Q}}_{\varepsilon\beta}^{T} \right) \boldsymbol{\varepsilon}_s = \hat{\mathbf{Q}}\, \boldsymbol{\varepsilon}_s \tag{3.74}$$

The components of matrix $\overline{Q}_s$ are then:

$$\begin{aligned} \hat{\mathbf{Q}} &= \begin{bmatrix} \overline{Q}_{11} - \frac{\overline{Q}_{12}^2}{\overline{Q}_{22}} & 0 & \overline{Q}_{16} - \frac{\overline{Q}_{12}\,\overline{Q}_{26}}{\overline{Q}_{22}} \\ 0 & \overline{Q}_{55} - \frac{\overline{Q}_{45}^2}{\overline{Q}_{44}} & 0 \\ \overline{Q}_{16} - \frac{\overline{Q}_{12}\,\overline{Q}_{26}}{\overline{Q}_{22}} & 0 & \overline{Q}_{66} - \frac{\overline{Q}_{26}^2}{\overline{Q}_{22}} \end{bmatrix} \\ &= \begin{bmatrix} \hat{Q}_{11} & 0 & \hat{Q}_{16} \\ 0 & \hat{Q}_{55} & 0 \\ \hat{Q}_{16} & 0 & \hat{Q}_{66} \end{bmatrix} \end{aligned} \tag{3.75}$$

Considering the expression of the virtual internal work, it is possible to perform the integral over the cross section, since the dependency on coordinates $(b\,, n)$ are pre-determined, reducing the volume integral into a line integral:

$$\begin{aligned} \delta W_i^s &= \int_\Gamma \int_A \left(\delta\boldsymbol{\varepsilon}_{\boldsymbol{s}}^0 + (\mathbf{d}\times)^T\, \delta\mathbf{k}_s \right)^T \boldsymbol{\sigma}_s\, dA\, d\Gamma \\ &= \int_\Gamma \delta\boldsymbol{\varepsilon}_{\boldsymbol{s}}^{0\,T} \int_A \boldsymbol{\sigma}_s\, dA\, d\Gamma + \int_\Gamma \delta\mathbf{k}^T \int_A (\mathbf{d}\times)\, \boldsymbol{\sigma}_s\, dA\, d\Gamma \\ &= \int_\Gamma \delta\boldsymbol{\varepsilon}_{\boldsymbol{s}}^{0\,T}\, \mathbf{F}_s\, d\Gamma + \int_\Gamma \delta\mathbf{k}^T\, \mathbf{M}_s\, d\Gamma \end{aligned} \tag{3.76}$$

where $\mathbf{F}_s = \{F_t\,, F_n\,, F_b\}^T$ and $\mathbf{M}_s = \{M_t\,, M_n\,, M_b\}^T$ are the beam internal

forces and moments respectively. By substituting relation 3.74 in the surface integrals in 3.76, the constitutive relation at internal forces level are obtained:

$$\begin{aligned}\mathbf{F}_s &= \int_A \hat{\mathbf{Q}}\, dA\, \boldsymbol{\varepsilon}_s^0 + \int_A \hat{\mathbf{Q}}\, (\mathbf{d}\times)^T\, dA\, \mathbf{k}_s = \mathbf{D}_{FF}\, \boldsymbol{\varepsilon}_s^0 + \mathbf{D}_{FM}\, \mathbf{k}_s \\ \mathbf{M}_s &= \int_A (\mathbf{d}\times)\, \hat{\mathbf{Q}}\, dA\, \boldsymbol{\varepsilon}_s^0 + \int_A (\mathbf{d}\times)\, \hat{\mathbf{Q}}\, (\mathbf{d}\times)^T\, dA\, \mathbf{k}_s = \mathbf{D}_{FM}^T\, \boldsymbol{\varepsilon}_s^0 + \mathbf{D}_{MM}\, \mathbf{k}_s\end{aligned} \tag{3.77}$$

Components of matrices ($\mathbf{D}_{FF}\,, \mathbf{D}_{FM}\,, \mathbf{D}_{MM}$), are computed solving the area integrals, obtaining the following results:

$$\begin{aligned}\mathbf{D}_{FF} &= \begin{bmatrix} h_s\overline{A}_{11} & 0 & h_s\overline{A}_{16} \\ 0 & h_s\overline{A}_{55}K_s & 0 \\ h_s\overline{A}_{16} & 0 & h_s\overline{A}_{66} \end{bmatrix} \\ \mathbf{D}_{FM} &= \begin{bmatrix} h_s\overline{B}_{16} & h_se\overline{A}_{11} & -h_s\overline{B}_{11} \\ -h_se\overline{A}_{55}K_s & 0 & 0 \\ h_s\overline{B}_{66} & h_se\overline{A}_{16} & -h_s\overline{B}_{16} \end{bmatrix} \\ \mathbf{D}_{MM} &= \begin{bmatrix} GJ & h_se\overline{B}_{16} & h_s\overline{D}_{16} \\ h_se\overline{B}_{16} & \left(\frac{h_s^3}{12} + h_se^2\right)\overline{A}_{11} & -h_se\overline{B}_{11} \\ h_s\overline{D}_{16} & -h_se\overline{B}_{11} & h_s\overline{D}_{11} \end{bmatrix}\end{aligned} \tag{3.78}$$

where shear factor K_s has been introduced, along with beam laminate stiffnesses:

$$\begin{aligned}\overline{\mathbf{A}} &= \sum_{k=1}^{n_s} \int_{n_k}^{n_{k+1}} \hat{\mathbf{Q}}\, dn \qquad \overline{\mathbf{B}} = \sum_{k=1}^{n_s} \int_{n_k}^{n_{k+1}} n\, \hat{\mathbf{Q}}\, dn \\ \overline{\mathbf{D}} &= \sum_{k=1}^{n_s} \int_{n_k}^{n_{k+1}} n^2\, \hat{\mathbf{Q}}\, dn\end{aligned} \tag{3.79}$$

Matrices ($\overline{\mathbf{A}}$, $\overline{\mathbf{B}}$, $\overline{\mathbf{D}}$) are obtained performing the first integration along the thickness coordinate of the laminate, which is also the width coordinate of the beam considering the assumption on the lamination direction. Surface integrals are then completed with a second integration along the height of

the beam leading to all the terms in 3.78. To make all these steps more clear, the case of the torque M_t is considered, which will be useful also to derive the expression of torsional stiffness GJ:

$$\begin{aligned} M_t &= \int_{h_s}\int_{t_s} (n\,\tau_b - b\,\tau_n)\; dn\, db \\ &= \int_{h_s}\int_{t_s} n\,\hat{Q}_{16}\, dn\, db\,\varepsilon_t^0 + \int_{h_s}\int_{t_s} n\,\hat{Q}_{66}\, dn\, db\,\gamma_b^0 + \int_{h_s}\int_{t_s} n^2\,\hat{Q}_{66}\, dn\, db\, k_t \\ &\quad + \int_{h_s}\int_{t_s} n\,b\,\hat{Q}_{16}\, dn\, db\, k_n - \int_{h_s}\int_{t_s} n^2\,\hat{Q}_{16}\, dn\, db\, k_b \\ &\quad - \int_{h_s}\int_{t_s} b\,K_s\,\hat{Q}_{55}\, dn\, db\,\gamma_n^0 + \int_{h_s}\int_{t_s} b^2\,K_s\,\hat{Q}_{55}\, dn\, db\, k_t \end{aligned} \tag{3.80}$$

and using 3.79:

$$\begin{aligned} M_t &= \int_{h_s} \overline{B}_{16}\, db\,\varepsilon_t^0 + \int_{h_s} \overline{B}_{66}\, db\,\gamma_b^0 + \int_{h_s} b\,\overline{B}_{16}\, db\, k_n - \int_{h_s} \overline{D}_{16}\, db\, k_b \\ &\quad - \int_{h_s} b\,K_s\,\overline{A}_{55}\, db\,\gamma_n^0 + \int_{h_s} \left(\overline{D}_{66} + b^2\,K_s\,\overline{A}_{55}\right) db\, k_t \end{aligned} \tag{3.81}$$

eventually, integrating along the stiffener height:

$$\begin{aligned} M_t &= h_s\,\overline{B}_{16}\,\varepsilon_t^0 + h_s\,\overline{B}_{66}\,\gamma_b^0 + h_s\,e\,\overline{B}_{16}\,k_n - h_s\,\overline{D}_{16}\,k_b - h_s\,e\,K\,\overline{A}_{55}\,\gamma_n^0 \\ &\quad + \underbrace{\left[h_s\,\overline{D}_{66} + K\left(\frac{h_s^3}{12} + h_s e^2\right)\overline{A}_{55}\right]}_{GJ} k_t \end{aligned} \tag{3.82}$$

It is worth noting that the coupling between strain parameters is not only due to the laminate anisotropy, but it is also linked to the offset e, which is the distance of the elastic centroid of the beam from the plate midplane. Since the couple of coordinates $(s\,, n)$ is forced to lie on the midplane, when $e \neq 0$ the adopted axes are not the principal ones. At this point the virtual

internal work for the stiffener can be easily written as:

$$\delta W_i^s = \int_\Gamma \begin{Bmatrix} \delta\boldsymbol{\varepsilon}_s^l \\ \delta\mathbf{k}_s \end{Bmatrix}^T \begin{bmatrix} \mathbf{D}_{FF} & \mathbf{D}_{FM} \\ \mathbf{D}_{FM}^T & \mathbf{D}_{MM} \end{bmatrix} \begin{Bmatrix} \boldsymbol{\varepsilon}_s^l \\ \mathbf{k}_s \end{Bmatrix} ds + \int_\Gamma \delta w_{b/s}\, F_t^0\, w_{b/s}\, ds \tag{3.83}$$

and collecting all the unknowns in the vector $\mathbf{q}_s(s) = \begin{Bmatrix} \mathbf{u}_s(s) \\ \boldsymbol{\theta}_s(s) \end{Bmatrix}$:

$$\delta W_i^s = \int_\Gamma \Big(\boldsymbol{\mathfrak{D}}_1 \delta\mathbf{q}_s\Big)^T \mathbf{D}_s \Big(\boldsymbol{\mathfrak{D}}_1 \mathbf{q}_s\Big)\, ds + \int_\Gamma \Big(\boldsymbol{\mathfrak{D}}_2 \delta\mathbf{q}_s\Big)^T F_t^0 \Big(\boldsymbol{\mathfrak{D}}_2 \mathbf{q}_s\Big)\, ds \tag{3.84}$$

where $\mathbf{D}_1$ and $\boldsymbol{\mathfrak{D}}_2$ are differential operators through which it is possible to obtain strain parameters from displacements and rotations fields:

$$\begin{aligned} \boldsymbol{\mathfrak{D}}_1 &= \begin{bmatrix} \frac{\partial}{\partial s} & -\kappa(s) & 0 & 0 & 0 & 0 \\ \kappa(s) & \frac{\partial}{\partial s} & 0 & 0 & 0 & -1 \\ 0 & 0 & \frac{\partial}{\partial s} & 0 & 1 & 0 \\ 0 & 0 & 0 & \frac{\partial}{\partial s} & -\kappa(s) & 0 \\ 0 & 0 & 0 & \kappa(s) & \frac{\partial}{\partial s} & 0 \\ 0 & 0 & 0 & 0 & 0 & \frac{\partial}{\partial s} \end{bmatrix} \\ \boldsymbol{\mathfrak{D}}_2 &= \begin{bmatrix} 0 & 0 & \frac{\partial}{\partial s} & 0 & 0 & 0 \end{bmatrix} \end{aligned} \tag{3.85}$$

Virtual work of the external forces, which is composed by the inertial and external loads contributes, is now considered. Only forces applied at the two beam ends $\mathbf{p}_s = \{P_t\,, P_n\,, P_b\}^T$ are taken into account.

$$\begin{aligned} \delta W_e^s &= \int_\Gamma \int_A \delta\mathbf{u}_s^T \rho\, \ddot{\mathbf{u}}_s\, dA\, d\Gamma - \Big[\delta\mathbf{u}_s^{0^T} \mathbf{p}_s\Big]_{s=0}^{s=\Gamma} \\ &= \int_\Gamma \int_A \Big(\delta\mathbf{u}_s^{0^T} + \delta\boldsymbol{\theta}_s^T\,(\mathbf{d}\times)\Big)\, \rho\, \Big(\delta\ddot{\mathbf{u}}_s^0 + \delta\boldsymbol{\theta}_s^T\,(\mathbf{d}\times)\Big)\, dA\, d\Gamma \\ &\quad - \Big[\delta\mathbf{u}_s^{0^T} \mathbf{p}_s\Big]_{s=0}^{s=\Gamma} \end{aligned} \tag{3.86}$$

Considering that the kinematic parameters depend on the curvilinear coordinate only, it is possible to write:

$$\begin{aligned}\delta W_e^s = &\int_\Gamma \begin{Bmatrix}\delta \mathbf{u}_s^0 \\ \delta \boldsymbol{\theta}_s\end{Bmatrix}^T \begin{bmatrix}\int_A \rho\, \mathbf{I}\, dA & \int_A \rho\, (\mathbf{d}\times)^T\, dA \\ \int_A \rho\, (\mathbf{d}\times)\, dA & \int_A \rho\, (\mathbf{d}\times)\, (\mathbf{d}\times)^T\, dA\end{bmatrix} \begin{Bmatrix}\mathbf{u}_s^0 \\ \boldsymbol{\theta}_s\end{Bmatrix} d\Gamma \\ &- \left[\delta \mathbf{u}_s^{0^T}\, \mathbf{p}_s\right]_{s=0}^{s=\Gamma}\end{aligned} \tag{3.87}$$

As already done with the plate, density is assumed constant in the whole continuum. So Eq. 3.87 can be written as:

$$\begin{aligned}\delta W_e^s &= \int_\Gamma \begin{Bmatrix}\delta \mathbf{u}_s^0 \\ \delta \boldsymbol{\theta}_s\end{Bmatrix}^T \begin{bmatrix}\mathbf{M}_{uu} & \mathbf{M}_{u\theta} \\ \mathbf{M}_{u\theta}^T & \mathbf{M}_{\theta\theta}\end{bmatrix} \begin{Bmatrix}\mathbf{u}_s^0 \\ \boldsymbol{\theta}_s\end{Bmatrix} ds - \left[\delta \mathbf{u}_s^{0^T}\, \mathbf{p}_s\right]_{s=0}^{s=\Gamma} \\ &= \int_\Gamma \delta \mathbf{q}_s^T\, \overline{\mathbf{M}}_s\, \mathbf{q}_s\, ds - \left[\delta \mathbf{u}_s^{0^T}\, \mathbf{p}_s\right]_{s=0}^{s=\Gamma}\end{aligned} \tag{3.88}$$

with:

$$\begin{aligned}\mathbf{M}_{uu} &= \int_A \rho\, \mathbf{I}\, dA = \rho \begin{bmatrix}A & 0 & 0 \\ 0 & A & 0 \\ 0 & 0 & A\end{bmatrix} \\ \mathbf{M}_{u\theta} &= \int_A \rho\, (\mathbf{d}\times)^T\, dA = \rho \begin{bmatrix}0 & e\,A & 0 \\ -e\,A & 0 & 0 \\ 0 & 0 & 0\end{bmatrix} \\ \mathbf{M}_{\theta\theta} &= \int_A \rho\, (\mathbf{d}\times)\, (\mathbf{d}\times)^T\, dA = \rho \begin{bmatrix}I_n + I_b & 0 & 0 \\ 0 & I_n & 0 \\ 0 & 0 & I_b\end{bmatrix}\end{aligned} \tag{3.89}$$

where I_n and I_b are the area moment of inertia around n and b axis respectively.

3.4 Plate/Stiffener compatibility

The plate and stiffener models illustrated so far are now coupled to illustrate the modelling a stiffened plate. To this aim compatibility condition between plate and stiffeners has to be enforced. With this regard, the present Ritz procedure allows to impose the compatibilty conditions in a straightforward way, making the overall modeling process fast and efficient. This feature represents a noticeable advantage as the time for modelling could be, in the case of curvinearly-stiffened plates, particularly relevant. In finite elements, for instance, the plate/stiffener compatibility can be obtained using contact algorithms, or tritely by ensuring that plate and stiffeners share their nodes. In the first case, an algorithm able to recognize the plate element where a beam element node is located is needed, in order to approximate the displacement of such node using the shape functions of the 2D element[7] [6]. Otherwise, if plate and stiffener share the same nodes, the issue of re-meshing needs to be taken into account whenever the topology (i.e. the path of the stringer) changes, for example when a preliminary optimisation of the geometry has to be performed; moreover complex geometries can lead to the presence of distorted elements potentially decreasing the accuracy of the solution. Essentially, all this difficulties are caused by the presence of basis function whose support is defined on a small portion of the global domain. Differently, in a Ritz-based approach, the support of the basis functions is the whole plate surface, making the treatment of the junction much easier. In the following two different methods to enforce plate/stiffener compatibility are presented.

3.4.1 Penalty method

This method consists in the addition of an elastic element at the interface between plate and stiffener. The stiffness of this element has to be tuned so as to make it much more rigid compared to the other elastic elements of the system. In other words the contact is modelled through a "fictitious" distributed and infinitely rigid spring that connects the stiffener to the plate.

[7] Many contact algorithms are based on the so called *multipoint constraint*.

Consequently two sets of degrees of freedom are present, one describing the motion of the stiffener and the other one the motion of the plate. This means that a Ritz approximation of stiffener displacements and rotations is required. Since all the unknowns describing the movement of the beam depend on a single parameter, their discretization is composed of 1D Ritz functions defined in the interval $[-1\,,1]$. This implies a change of coordinate from the arc-length parameter $s \in [0\,,\Gamma]$, to parameter $\zeta \in [-1\,,1]$. The generic component $g(\zeta)$ can be discretized as:

$$g(\zeta) = \sum_{k=0}^{K} \psi_k(\zeta)\, C_k^g \tag{3.90}$$

being $\psi_k(\zeta)$, the k-th Legendre polynomial. Collecting all the unknowns in the vector $\mathbf{q}_s(\zeta) = \begin{Bmatrix} \mathbf{u}_s(\zeta) \\ \boldsymbol{\theta}_s(\zeta) \end{Bmatrix}$, similarly to what said for the plate, it is possible to write:

$$\mathbf{q}_s(\zeta) = \boldsymbol{\Psi}(\zeta)\, \mathbf{a}_s \tag{3.91}$$

At this point it is possible to substitute the discretisation in all the energetic contributes of the stiffener. The virtual internal work becomes:

$$\begin{aligned} \delta W_s &= \delta \mathbf{a}_s^T \int_{-1}^{1} \Big(\boldsymbol{\mathfrak{D}}_1 \boldsymbol{\Psi}(\zeta)\Big)^T \mathbf{D}_s \Big(\boldsymbol{\mathfrak{D}}_1 \boldsymbol{\Psi}(\zeta)\Big)\, J_s\, d\zeta\, \mathbf{a}_s \\ &= \delta \mathbf{a}_s^T\, \mathbf{K}_s\, \mathbf{a}_s + \delta \mathbf{a}_s^T\, \mathbf{K}_{sG}\, \mathbf{a}_s \end{aligned} \tag{3.92}$$

where J_s is the Jacobian of the curvilinear coordinate transformation which is also used to compute the derivative with respect to s, contained in differential operator $\boldsymbol{\mathfrak{D}}_1$:

$$\begin{aligned} J_s = \|\mathbf{r}_{/\zeta}\| &= \sqrt{\left(\frac{\partial x}{\partial \zeta}\right)^2 + \left(\frac{\partial y}{\partial \zeta}\right)^2} \\ \frac{\partial}{\partial s} &= \frac{1}{J_s}\frac{\partial}{\partial \zeta} \end{aligned} \tag{3.93}$$

The discretization of the virtual work of the inertia and external forces results in:

$$\begin{aligned}\delta U_s + \delta V_s &= \delta \mathbf{a}_s^T \int_{-1}^{1} \mathbf{\Psi}(\zeta)^T \, \overline{\mathbf{M}}_s \, \mathbf{\Psi}(\zeta) \, J_s \, ds \, \mathbf{a}_s - \delta \mathbf{a}_s^T \left[\mathbf{\Psi}(\zeta)^T \mathbf{p}_{stiff} \right]_{\zeta=-1}^{\zeta=1} \\ &= \delta \mathbf{a}_s^T \, \mathbf{M}_s \, \mathbf{a}_s - \delta \mathbf{a}_s^T \, \mathbf{P}_s \end{aligned} \tag{3.94}$$

The deformation work of the junction element can be written as:

$$\delta W_{ps} = \int_\Gamma \left[\left(\delta \hat{\mathbf{u}}_p^0 - \delta \hat{\mathbf{u}}_s^0 \right)^T \mathbf{K}_{ps}^u \left(\hat{\mathbf{u}}_p^0 - \hat{\mathbf{u}}_s^0 \right) \, d\Gamma + \left(\delta \hat{\boldsymbol{\theta}}_p - \delta \hat{\boldsymbol{\theta}}_s \right)^T \mathbf{K}_{ps}^\theta \left(\hat{\boldsymbol{\theta}}_p - \hat{\boldsymbol{\theta}}_s \right) \right] d\Gamma \tag{3.95}$$

where $(\hat{\mathbf{u}}_p^0 \, , \hat{\boldsymbol{\theta}}_p)$ and $(\hat{\mathbf{u}}_s^0 \, , \hat{\boldsymbol{\theta}}_s)$ are plate and stiffener fields expressed in the same reference frame. A good choice is to use the system of coordinate $(x \, , y \, , z)$ both for displacements and for rotations[8]. In this way the variables appearing in Eq. 3.95 are linked to the degrees of freedom $(\mathbf{u}_p \, , \boldsymbol{\theta}_p \, , \mathbf{u}_s \, , \boldsymbol{\theta}_s)$ by the following relations:

$$\begin{aligned} \hat{\mathbf{u}}_p^0 &= \mathbf{u}_p^0 \quad , \quad \hat{\mathbf{u}}_s^0 = \mathbf{R}^T \mathbf{u}_s^0 \\ \hat{\boldsymbol{\theta}}_p &= \mathfrak{J}^T \, \boldsymbol{\theta}_p \, , \quad \hat{\boldsymbol{\theta}}_s = \mathbf{R}^T \boldsymbol{\theta}_s \end{aligned} \tag{3.96}$$

where:

$$\mathbf{R} = \begin{bmatrix} \mathbf{t} & \mathbf{n} & \mathbf{b} \end{bmatrix}^T \quad , \quad \mathfrak{J} = \begin{bmatrix} 0 & 1 & 0 \\ -1 & 0 & 0 \\ 0 & 0 & 1 \end{bmatrix} \tag{3.97}$$

By substituting relations 3.97 in 3.95, and collecting the unknowns in vectors $\mathbf{q}_p$ and $\mathbf{q}_s$, the penalty contribute on the principle of virtual work can be written as:

$$\delta W_{ps} = \int_\Gamma \begin{Bmatrix} \delta \mathbf{q}_p \\ \delta \mathbf{q}_s \end{Bmatrix}^T \begin{bmatrix} \mathbf{\Lambda}_{pp} & \mathbf{\Lambda}_{ps} \\ \mathbf{\Lambda}_{ps}^T & \mathbf{\Lambda}_{ss} \end{bmatrix} \begin{Bmatrix} \mathbf{q}_p \\ \mathbf{q}_s \end{Bmatrix} d\Gamma \tag{3.98}$$

[8]It should be noted that this is not the reference frame used for plate rotation degrees of freedom, indeed they don't even follow the right hand rule.

where:

$$\begin{aligned}
\mathbf{\Lambda}_{pp} &= \begin{bmatrix} \mathbf{K}^u_{ps} & \mathbf{0} \\ \mathbf{0} & \mathfrak{J}\,\mathbf{K}^\theta_{ps}\,\mathfrak{J}^T \end{bmatrix} \\
\mathbf{\Lambda}_{ss} &= \begin{bmatrix} \mathbf{R}\,\mathbf{K}^u_{ps}\,\mathbf{R}^T & \mathbf{0} \\ \mathbf{0} & \mathbf{R}\,\mathbf{K}^\theta_{ps}\,\mathbf{R}^T \end{bmatrix} \\
\mathbf{\Lambda}_{ps} &= \begin{bmatrix} -\mathbf{K}^u_{ps}\,\mathbf{R}^T & \mathbf{0} \\ \mathbf{0} & -\mathfrak{J}\,\mathbf{K}^\theta_{ps}\,\mathbf{R}^T \end{bmatrix}
\end{aligned} \tag{3.99}$$

At this point it is possible to introduce the Ritz approximation:

$$\begin{aligned}
\delta W_{ps} &= \begin{Bmatrix} \delta\mathbf{a}_p \\ \delta\mathbf{a}_s \end{Bmatrix}^T \int_{-1}^{1} \begin{bmatrix} \mathbf{\Phi}^T\mathbf{\Lambda}_{pp}\,\mathbf{\Phi} & \mathbf{\Phi}^T\mathbf{\Lambda}_{ps}\,\mathbf{\Psi} \\ \mathbf{\Psi}^T\mathbf{\Lambda}^T_{ps}\mathbf{\Phi} & \mathbf{\Psi}^T\mathbf{\Lambda}_{ss}\,\mathbf{\Psi} \end{bmatrix} J_s\,d\zeta \begin{Bmatrix} \mathbf{a}_p \\ \mathbf{a}_s \end{Bmatrix} \\
&= \begin{Bmatrix} \delta\mathbf{a}_p \\ \delta\mathbf{a}_s \end{Bmatrix}^T \begin{bmatrix} \mathbf{Z}_{pp} & \mathbf{Z}_{ps} \\ \mathbf{Z}^T_{ps} & \mathbf{Z}_{ss} \end{bmatrix} \begin{Bmatrix} \mathbf{a}_p \\ \mathbf{a}_s \end{Bmatrix}
\end{aligned} \tag{3.100}$$

The integral in 3.100 can be easily computed with gaussian quadrature rule. The evaluation in the integration point ζ_i of terms depending on $(\xi\,,\eta)$, and not directly on ζ, can be performed using relations in Eq. 3.41 and Eq. 3.63.

3.4.2 Strong form approach

The second method that has been developed consists in the description of the beam kinematics as a function of that of the plate. In other words, the compatibility is imposed in strong form by enforcing the requirement in terms of problem unknowns. This can be achieved considering the following relations:

$$\mathbf{u}^0_s(s) = \mathbf{R}\,\mathbf{u}^0_p(x,y) \quad , \qquad \boldsymbol{\theta}_s(s) = \mathbf{R}\,\mathfrak{J}^T\,\boldsymbol{\theta}_p(x,y) \tag{3.101}$$

which can be directly substituted in the expressions of the beam virtual work, making the set of plate degrees of freedom the only unknowns, no matter the number of the stringers. Consequently a mono-dimensional discretization of each beam element is unnecessary. The key point is the handling of the beam strains that are obtained through the differential operator $\mathfrak{D}_1$ which

involves the derivative with respect to arc-length parameter. Considering, for example, the axial strain ε_t^0:

$$\begin{aligned}\varepsilon_t^0 &= \frac{\partial\, u_t^0}{\partial s} - \kappa\, v_n^0 \\ &= \frac{\partial\left(\mathbf{u}_p^0 \cdot \mathbf{t}\right)}{\partial s} - \kappa\,\left(\mathbf{u}_p^0 \cdot \mathbf{n}\right) = \frac{\partial \mathbf{u}_p^0}{\partial s} \cdot \mathbf{t} + \mathbf{u}_p^0 \cdot \frac{\partial \mathbf{t}}{\partial s} - \kappa\,\left(\mathbf{u}_p^0 \cdot \mathbf{n}\right) \\ &= \frac{\partial \mathbf{u}_p^0}{\partial s} \cdot \mathbf{t}\end{aligned} \tag{3.102}$$

where in the last step the Frénét formulas 3.61 have been used to solve the tangent vector derivative. Now using the chain rule it is possible to write:

$$\begin{aligned}\varepsilon_t^0 &= \left[\left(\frac{\partial \mathbf{u}_p^0}{\partial x}\,\frac{\partial x}{\partial s} + \frac{\partial \mathbf{u}_p^0}{\partial y}\,\frac{\partial y}{\partial s}\right)\right] \cdot \mathbf{t} \\ &= \left[\frac{1}{J_s}\left(\frac{\partial \mathbf{u}_p^0}{\partial x}\,\frac{\partial x}{\partial \zeta} + \frac{\partial \mathbf{u}_p^0}{\partial y}\,\frac{\partial y}{\partial \zeta}\right)\right] \cdot \mathbf{t}\end{aligned} \tag{3.103}$$

At this point Ritz approximation for plate displacement[9] $\mathbf{u}_p^0 = \boldsymbol{\Phi}_u(\xi,\eta)\,\mathbf{a}_p^u$ is introduced, and recalling the differentiation rule 3.42:

$$\begin{aligned}\varepsilon_t^0 &= \left[\frac{1}{J_s}\left(\frac{2}{a}\,\frac{\partial \boldsymbol{\Phi}_u}{\partial \xi}\,\frac{\partial x}{\partial \zeta} + \frac{2}{b}\,\frac{\partial \boldsymbol{\Phi}_u}{\partial \eta}\,\frac{\partial y}{\partial \zeta}\right)\,\mathbf{a}_p^u\right] \cdot \mathbf{t} \\ &= \left[\frac{\mathbf{t}^T}{J_s}\left(\frac{2}{a}\,\frac{\partial \boldsymbol{\Phi}_u}{\partial \xi}\,\frac{\partial x}{\partial \zeta} + \frac{2}{b}\,\frac{\partial \boldsymbol{\Phi}_u}{\partial \eta}\,\frac{\partial y}{\partial \zeta}\right)\right]\,\mathbf{a}_p^u\end{aligned} \tag{3.104}$$

The same approach can be adopted for all the other strain parameters and for the derivative of the transversal displacement $w_{b/s}^0$ (Appendix A), and eventually it is possible to express them as functions of the plate degrees of freedom (set $\mathbf{a}_p$):

$$\begin{Bmatrix}\boldsymbol{\varepsilon}_s^0 \\ \mathbf{k}_s\end{Bmatrix} = \boldsymbol{H}_1\,\mathbf{a}_p \qquad , \qquad w_{b/s}^0 = \boldsymbol{H}_2\,\mathbf{a}_p \tag{3.105}$$

[9] $\boldsymbol{\Phi}_u(\xi,\eta)$ is a principal north-west submatrix of matrix $\boldsymbol{\Phi}(\xi,\eta)$, see Appendix A.

In a similar way substituting the obtained relation into the beam virtual internal work:

$$\begin{aligned}\delta W_s &= \delta\mathbf{a}_p^T \int_{-1}^{1} \boldsymbol{H}_1^T \, \mathbf{D}_s \, \boldsymbol{H}_1 \, J_s \, d\zeta \, \mathbf{a}_p + \delta\mathbf{a}_p^T \int_{-1}^{1} \boldsymbol{H}_2^T \, F_t^0 \boldsymbol{H}_2 \, J_s \, d\zeta \, \mathbf{a}_p \\ &= \delta\mathbf{a}_p^T \, \tilde{\mathbf{K}}_s \, \delta\mathbf{a}_p + \delta\mathbf{a}_p^T \, \tilde{\mathbf{K}}_{Gs} \, \delta\mathbf{a}_p\end{aligned} \tag{3.106}$$

Differently, relations 3.101 can be directly substituted in the virtual external work:

$$\begin{aligned}\delta U_s &= \int_\Gamma \begin{Bmatrix} \delta\mathbf{u}_p^0 \\ \delta\boldsymbol{\theta}_p \end{Bmatrix}^T \begin{bmatrix} \mathbf{R}^T \mathbf{M}_{uu} \mathbf{R} & \mathbf{R}^T \mathbf{M}_{u\theta} \mathbf{R} \, \boldsymbol{\mathcal{I}}^T \\ \boldsymbol{\mathcal{I}} \, \mathbf{R}^T \mathbf{M}_{u\theta}^T \mathbf{R} & \boldsymbol{\mathcal{I}} \, \mathbf{R}^T \mathbf{M}_{\theta\theta} \mathbf{R} \, \boldsymbol{\mathcal{I}}^T \end{bmatrix} \begin{Bmatrix} \mathbf{u}_p^0 \\ \boldsymbol{\theta}_p \end{Bmatrix} ds \\ \delta V_s &= -\left[\delta\mathbf{u}_p^{0^T} \, \mathbf{R}^T \, \mathbf{p}_s \right]_{s=0}^{s=\Gamma}\end{aligned} \tag{3.107}$$

and introducing the discretization:

$$\begin{aligned}\delta U_s &= \begin{Bmatrix} \delta\mathbf{a}_p^u \\ \delta\mathbf{a}_p^\theta \end{Bmatrix}^T \int_{-1}^{1} \begin{bmatrix} \boldsymbol{\Phi}_u^T \mathbf{R}^T \mathbf{M}_{uu} \mathbf{R} \boldsymbol{\Phi}_u & \boldsymbol{\Phi}_u^T \mathbf{R}^T \mathbf{M}_{u\theta} \mathbf{R} \, \boldsymbol{\mathcal{I}}^T \boldsymbol{\Phi}_\theta \\ \boldsymbol{\Phi}_\theta^T \boldsymbol{\mathcal{I}} \, \mathbf{R}^T \mathbf{M}_{u\theta}^T \mathbf{R} \boldsymbol{\Phi}_u & \boldsymbol{\Phi}_\theta^T \boldsymbol{\mathcal{I}} \, \mathbf{R}^T \mathbf{M}_{\theta\theta} \mathbf{R} \, \boldsymbol{\mathcal{I}}^T \boldsymbol{\Phi}_\theta \end{bmatrix} J_s \, d\zeta \begin{Bmatrix} \delta\mathbf{a}_p^u \\ \delta\mathbf{a}_p^\theta \end{Bmatrix} \\ &= \delta\mathbf{a}_p^T \, \tilde{\mathbf{M}}_s \, \mathbf{a}_p \\ \delta V_s &= -\delta\mathbf{a}_p^{0^T} \, \left[\boldsymbol{\Phi}_u^T \mathbf{R}^T \, \mathbf{p}_s \right]_{\zeta=-1}^{\zeta=1} = -\delta\mathbf{a}_p^{0^T} \, \tilde{\mathbf{P}}_s\end{aligned} \tag{3.108}$$

Differently from penalty method, as better described in the following section, in the general case where more than one stiffener is present, the size of the matrices remains unchanged, as the number of degrees of freedom remains limited to that of set $\mathbf{a}_p$; the same approach is repeated for all the stiffeners and the resulting matrices have to be added up.

3.5 Discrete governing equations

In this section the discrete equations describing the stiffened plate behaviour are discussed with regard to the linear static, buckling and free vibration responses. The considered structure is the composite laminated

plate stiffened by an arbitrary number of curvilinear stringers. Plate related quantities will be labelled with subscript $(\cdot)_p$, while k-th stiffener related ones with $(\cdot)_s^{(k)}$.

3.5.1 Linear Static Analysis

The first analysis considered aims to compute displacements, strains and stresses due to external loads. The problem is static, meaning that the loads are constant in time or slow enough compared to the characteristic frequencies of the structure. In this circumstances the response can be modelled as static.
The expression of the principle of virtual work depends on the method adopted to enforce plate/stiffener compatibility. Considering the penalty method it can be written as:

$$\delta W_p + \delta V_p + \sum_{k=1}^{N} \left(\delta W_s^{(k)} + \delta W_{ps}^{(k)} + \delta V_s^{(k)} \right) = 0 \tag{3.109}$$

Recalling the notation adopted, the degrees of freedom are arranged in the following set:

$$\mathbf{a} = \begin{Bmatrix} \mathbf{a}_p \\ \mathbf{a}_s^{(1)} \\ \mathbf{a}_s^{(2)} \\ \vdots \\ \mathbf{a}_s^{(N)} \end{Bmatrix} \tag{3.110}$$

The elastic and geometric global stiffness matrices are so assembled:

$$\mathbf{K} = \begin{bmatrix} \mathbf{K}_p & \mathbf{0} & \mathbf{0} & \cdots & \mathbf{0} \\ \mathbf{0} & \mathbf{K}_s^{(1)} & \mathbf{0} & \cdots & \mathbf{0} \\ \mathbf{0} & \mathbf{0} & \mathbf{K}_s^{(2)} & \cdots & \mathbf{0} \\ \vdots & \vdots & \vdots & \ddots & \vdots \\ \mathbf{0} & \mathbf{0} & \mathbf{0} & \cdots & \mathbf{K}_s^{(N)} \end{bmatrix} \qquad \mathbf{K}_G = \begin{bmatrix} \mathbf{K}_{pG} & \mathbf{0} & \mathbf{0} & \cdots & \mathbf{0} \\ \mathbf{0} & \mathbf{K}_{sG}^{(1)} & \mathbf{0} & \cdots & \mathbf{0} \\ \mathbf{0} & \mathbf{0} & \mathbf{K}_{sG}^{(2)} & \cdots & \mathbf{0} \\ \vdots & \vdots & \vdots & \ddots & \vdots \\ \mathbf{0} & \mathbf{0} & \mathbf{0} & \cdots & \mathbf{K}_{sG}^{(N)} \end{bmatrix} \tag{3.111}$$

The penalty matrix gets filled with all the terms coming from the junction of all the stiffeners to the plate:

$$\mathbf{Z} = \begin{bmatrix} \mathbf{Z}_{pp} & \mathbf{Z}_{ps}^{(1)} & \mathbf{Z}_{ps}^{(2)} & \cdots & \mathbf{Z}_{ps}^{(N)} \\ \mathbf{Z}_{ps}^{(1)T} & \mathbf{Z}_{ss}^{(1)} & \mathbf{0} & \cdots & \mathbf{0} \\ \mathbf{Z}_{ps}^{(2)T} & \mathbf{0} & \mathbf{Z}_{ss}^{(2)} & \cdots & \mathbf{0} \\ \vdots & \vdots & \vdots & \ddots & \vdots \\ \mathbf{Z}_{ps}^{(N)T} & \mathbf{0} & \mathbf{0} & \cdots & \mathbf{Z}_{ss}^{(N)} \end{bmatrix} \tag{3.112}$$

Accordingly, the vector of the external loads becomes:

$$\mathbf{P} = \begin{Bmatrix} \mathbf{P}_p \\ \mathbf{P}_s^{(1)} \\ \mathbf{P}_s^{(2)} \\ \vdots \\ \mathbf{P}_s^{(N)} \end{Bmatrix} \tag{3.113}$$

Recalling the arbitrariness of the virtual variations of the unknowns, the problem is reduced to the following linear system:

$$\left(\mathbf{K} + \mathbf{K}_G + \mathbf{Z}\right) \mathbf{a} = \mathbf{P} \tag{3.114}$$

In the case of strong form enforcement of the compatibility, the principle of virtual work does not require the introduction of penalty-related energetic contributes:

$$\delta W_p + \delta V_p + \sum_{k=1}^{N} \left(\delta W_s^{(k)} + \delta V_s^{(k)}\right) = 0 \tag{3.115}$$

In this case, since the set of degrees of freedom is $\mathbf{a} = \mathbf{a}_p$, the global matrices are computed adding up all the terms related to the single structural

components:

$$\begin{aligned}\mathbf{K} &= \mathbf{K}_p + \sum_{k=1}^{N} \tilde{\mathbf{K}}_s^{(k)} \\ \mathbf{K}_G &= \mathbf{K}_{pG} + \sum_{k=1}^{N} \tilde{\mathbf{K}}_{sG}^{(k)} \\ \mathbf{P} &= \mathbf{P}_p + \sum_{k=1}^{N} \tilde{\mathbf{P}}_s^{(k)}\end{aligned} \tag{3.116}$$

The linear system is then:

$$(\mathbf{K} + \mathbf{K}_G)\, \mathbf{a} = \mathbf{P} \tag{3.117}$$

3.5.2 Buckling analysis

Linearized buckling analysis allows to determine the critical load of a perfect structure over which the uniqueness of the elastic solution is lost. It has to be pointed out that this analysis does not allow to predict the so-called post-buckling behaviour of the structure, namely the sequence of equilibrium configurations with increasing the load after the critical one. The linearisation is performed around the pre-buckling configuration which is the result of the linear static analysis:

$$\mathbf{K}\,\mathbf{a} = \mathbf{P}_0 \tag{3.118}$$

where for simplicity it is assumed that matrix $\mathbf{K}$ includes also $\mathbf{Z}$ if the compatibility is enforced using the penalty method. The resulting spatial distribution of the stresses is necessary to compute the geometric stiffness matrix $\mathbf{K}_G$. Since the pre-buckling problem is linear, the stress distribution resulting from an applied load $\lambda\mathbf{P}_0$ will lead to a geometric geometric stiffness matrix $\lambda\mathbf{K}_G$. Linear buckling analysis is performed solving the following linear eigenvalue problem:

$$(\mathbf{K} + \lambda\mathbf{K}_G)\, \Delta\mathbf{a} = \mathbf{0} \tag{3.119}$$

The solution of the eigenvalue problem gives the critical load $\lambda_{cr}\mathbf{P}_0$, and the corresponding eigenvector provides the mode shape. There are cases in which the pre-stress distribution is already known due to the simplicity of the problem, and the pre-buckling analysis can be performed analytically. This is the case for example of a constant stiffness laminated plate uniformly loaded at the edges, in which the stresses are constant throughout the plate surface and equal to the applied forces per unit length. The complexity of the structure considered here does not allow for such simplification, and the only way to compute the pre-stress distribution is to perform the pre-buckling analysis.

3.5.3 Free vibration analysis

The virtual work principle for a dynamic system writes:

$$\delta U_p + \delta W_p + \delta V_p + \sum_{k=1}^{N} \left(\delta U_s^{(k)} + \delta W_s^{(k)} + \delta V_s^{(k)} \right) = 0 \tag{3.120}$$

leading to the following set of ordinary differential equations with constant coefficients:

$$\mathbf{M}\,\ddot{\mathbf{a}} + (\mathbf{K} + \mathbf{K}_G)\,\mathbf{a} = \mathbf{P} \tag{3.121}$$

which can be written in the frequency domain:

$$\left[-\omega^2\,\mathbf{M} + (\mathbf{K} + \mathbf{K}_G) \right] \mathbf{a} = \mathbf{P} \tag{3.122}$$

The characteristic frequencies of the problem can be computed considering the linear eigenvalue problem associated to the homogeneous problem:

$$\left[-\omega^2\,\mathbf{M} + (\mathbf{K} + \mathbf{K}_G) \right] \mathbf{a} = \mathbf{0} \tag{3.123}$$

The eigenvalues ω_i^2 give us the natural frequencies $f_i = \frac{2\pi}{\omega_i}$ of the system, and the eigenvectors $\mathbf{a}_i$ their mode shapes. All of this is valid when the

compatibility in strongly enforced, but the same notation can be adopted also for the penalty method remembering to include in $\mathbf{K}$ the matrix $\mathbf{Z}$, as the penalty contribute has to be added in the expression of the virtual work principle.

4. Results and discussion

In the following sections the results obtained using the present Ritz-based procedure are presented for a number of test cases. In the first part of the chapter, illustrated is the comparison against finite element calculations using the commercial code Nastran. The efficiency of the proposed computational tool is exploited to perform parametric studies in the second part of the chapter. These studies allow to investigate the mechanical behaviour of this kind of structure and the sensitivity to optimal configuration varying the number of polynomials.

4.1 Comparisons with Finite Element Method

4.1.1 Bending analysis

In this example a simply-supported composite plate stiffened with one curvilinear stringer is loaded with a uniform distribution of pressure $p = 0.001\,MPa$ along the direction z. The dimensions of the structural elements are summarized in Figure 4.9. Stiffener reference line is parametrised using a 2^{nd} order Bézier curve, the position of its control points is reported in Table 4.2. The material considered is a graphite/epoxy composite material whose mechanical properties are reported in Table 4.3. A quasi-isotropic lamination sequence $[0/90/+45/-45]_s$ is chosen following the guidelines reported in [34], about technological constraints and damage tolerability for aircraft structures. The thickness of each ply is 0.129 mm. This solution is adopted for both the plate and stiffeners and it is used also for the other examples in this work.

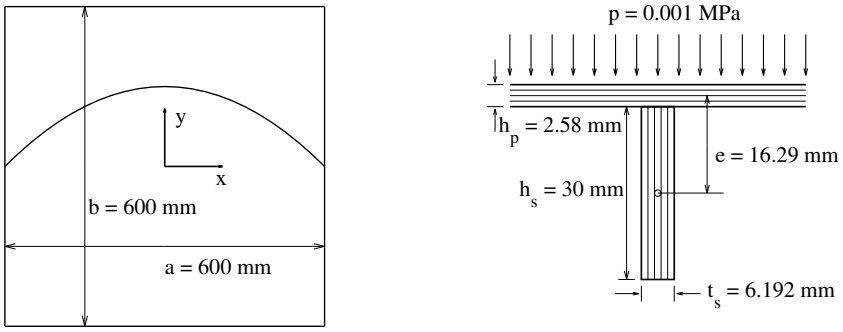

Figure 4.9: Geometry of the example for bending analysis.

Linear static analyses are performed using the Ritz method, gradually increasing the number $R = S$ of polynomials to assess the convergence of the method. Both the approaches to enforce plate/stiffener compatibility are used. Then the analysis is performed with finite elements, where the problem is modelled using CQUAD4 and CTRIA3 elements for the plate, and PBEAM elements for the stringer. It should be remarked that the PBEAM property does not allow to define a fully anistropic beam section, therefore the bendiwng/twisting coupling due to the not null contributions $D16$ and $D26$ is neglected.

A convergence study is presented in Table 4.4, where the maximum values for bending displacement and rotations are presented by considering an increasing number of trial functions. Also, the two different techniques for imposing the compatibility conditions are employed in order to highlight the impact over the convergence of the solution. The values of the maximum transversal displacement for an increasing number of polynomials are reported in Figure 4.10. It can be noted that convergence is monotonic, and a relatively large number of trial functions is needed for achieving errors below 5%. Moreover, one can observe that penalty method and strong compatibility enforcement produce the same results, demonstrating the correctness of the two distinct implementations. With a maximum difference of 2.8%

on the maximum vertical displacement between the present method and the finite element analysis, it is possible to say that the mechanical behaviour of the structure under bending load is well captured.
The transversal displacement at points on the line $(x = 0\,, y)$ is evaluated varying number of polynomials considered in the analysis, and reported in Figure 4.11. The comparison for transversal displacement and rotations between finite elements result and the present method is shown in Figure 4.12. The analysis is carried out using 30 polynomials. It should be noted that, for this comparison, the definition of the sign of the rotation is taken equal to that adopted in the finite element model.

	x, mm	y, mm	z, mm
P_0	-300	0	0
P_1	0	-300	0
P_2	300	0	0

Table 4.2: Position of the 2^{nd} order Bézier curve control points.

E_{11}, GPa	E_{22}, MPa	G_{12}, MPa	ν_{12}	ρ, kg/m^3
150	9080	5290	0.32	1350

Table 4.3: Engineering properties of graphite/epoxy composite material (IM7/8552) [33].

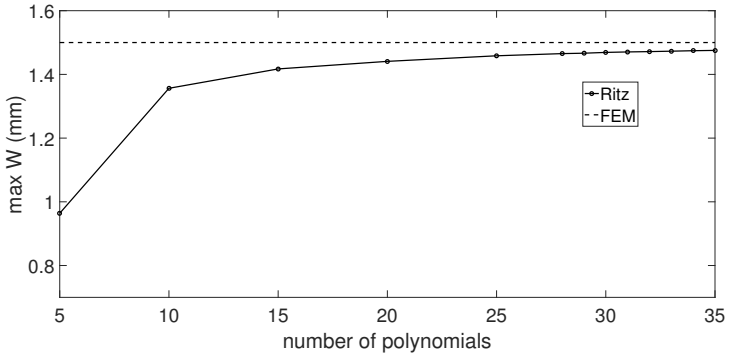

Figure 4.10: Convergence of the Ritz method for bending analysis of curvilinearly stiffened plate.

	strong enforcement			penalty method		
$R = S$	$w\,(mm)$	$\theta_x\,(rad)$	$\theta_y\,(rad)$	$w\,(mm)$	$\theta_x\,(rad)$	$\theta_y\,(rad)$
5	0.9640	0.0046	0.0074	0.9589	0.0046	0.0070
10	1.3564	0.0074	0.0081	1.3550	0.0074	0.0081
15	1.4172	0.0076	0.0084	1.4173	0.0076	0.0084
20	1.4409	0.0076	0.0085	1.4411	0.0076	0.0085
25	1.4584	0.0078	0.0086	1.4586	0.0078	0.0086
30	1.4690	0.0078	0.0086	1.4692	0.0078	0.0086
32	1.4715	0.0078	0.0086	1.4717	0.0078	0.0086
35	1.4753	0.0078	0.0086	1.4755	0.0078	0.0086
FEM	1.517	0.0080	0.0088			

Table 4.4: Results for bending analysis of simply supported curvilinearly stiffened plate.

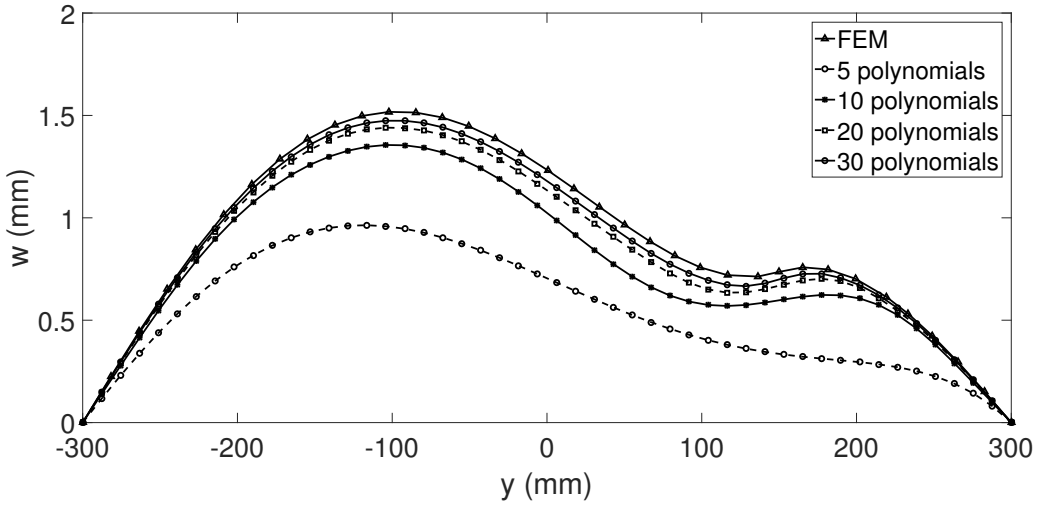

Figure 4.11: Transversal displacement at points on the line $(x = 0\,, y)$ for different number of polynomials.

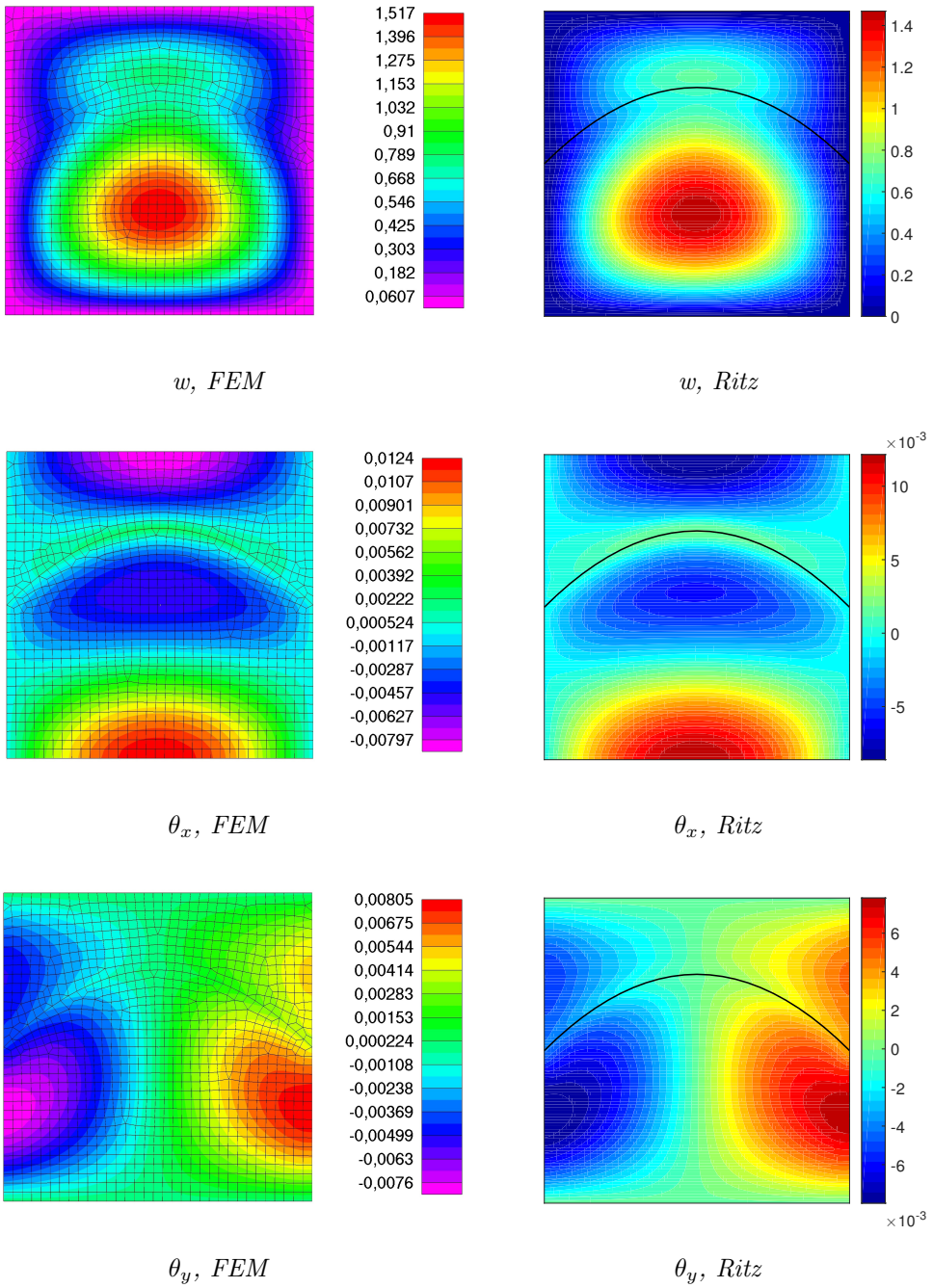

Figure 4.12: Results in terms of transversal displacement and rotations, for bending analysis of curvilinearly stiffened plate.

4.1.2 Free-Vibrations

Free vibration analysis is conducted on the same structure presented in the previous section. Thus, for conciseness, data are not reported here.
The finite element model of the stringer is now carried out using 2D elements, in order to account for the elastic couplings not captured by the Nastran beam model in terms of beam constitutive law. Also in this case different analyses have been performed with increasing the number of polynomials. The results obtained using the present method, with strong enforcement of the compatibility, are presented in Table 4.5 along with the results of the finite element analysis. The first three nondimensional frequencies $\mu^{(i)}$ are summarized in Figure 4.13, where calculations were carried out with the present Ritz formulation for an increasing number of polynomials. The normalization factor is given by the finite elements result:

$$\mu^{(i)} = \frac{\omega^{(i)}}{\omega^{(i)}_{FEM}} \tag{4.124}$$

Also in this case, the convergence is monotonic and shows, as expected, a progressive reduction of the inherent overstiffness associated with the numerical model. At convergence the maximum difference between finite element and Ritz results is about 4% on the second eigen-frequency. Such difference, can be partially attributed to the different modelling solution of the stiffener. In Figure 4.14 are reported the comparison of the first six mode shapes between the present method and Nastran results. The obtained results are in good agreement with finite element computations.
As previously said, when using a commercial FEM software for modeling a curvilinearly stiffened plate, much effort is required for defining the stiffener mesh, as its elements are required to share their nodes with those of the plate. Moreover, when the stiffener is modelled with 2D elements as in this case, a variation of the stiffener size requires a re-definition of the geometry. The process is very time demanding, as the mesh has to be continuously updated to the new surface. In the present method, only few parameters are needed to model the entire structure, and they can be easily modified.

	Number of polynomials $R = S$						FEM
Mode	15	20	25	30	32	35	
1	96.12	95.07	94.42	94.04	93.92	93.77	91.49
2	138.22	136.79	135.93	135.46	135.34	135.15	129.81
3	164.24	163.53	163.16	162.92	162.85	162.76	160.22
4	245.13	243.98	243.36	243.01	242.91	242.77	240.41
5	284.98	283.26	282.34	281.77	281.61	281.39	276.35
6	333.48	332.90	332.60	332.41	332.35	332.28	316.99

Table 4.5: Frequencies (Hz) of the first eight natural modes for simply supported curvilinearly stiffened plate.

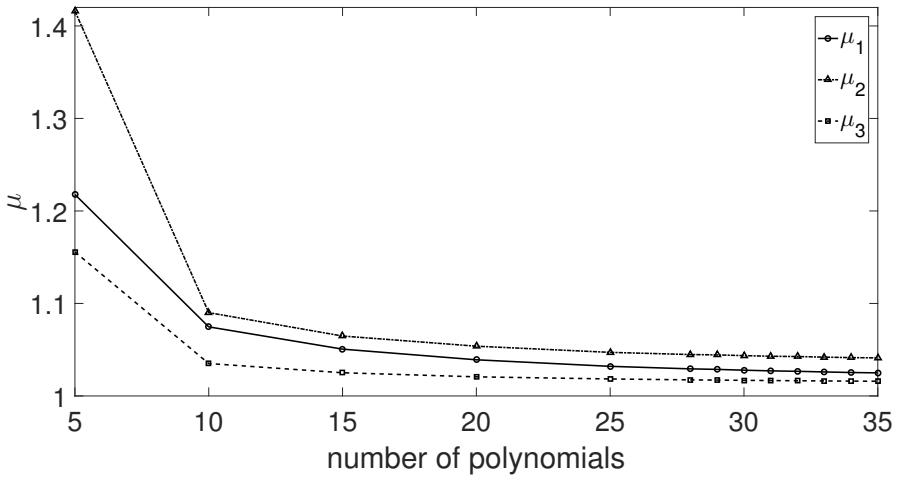

Figure 4.13: Convergence of the Ritz method for the first six natural frequencies of simply supported curvilinearly stiffened plate.

4.1.3 Pre-buckling analysis: uniaxial compression

In this section, the stiffened panel considered in the two previous sections is studied in terms of buckling response for uniaxial compression.
The results of the prebuckling analysis are presented in Figure 4.15, where the contour of the out-of-plane deflections is reported for a unitary membrane force per unit length N_{xx}. For simplicity, but with no loss of generality, no load is applied to the stiffener (sniped stiffener, see Brubak et al. [16]).
One can observe that in contrast to the well-known behaviour of flat unstiffened plates - for which the pre-buckling state is purely a membrane state -

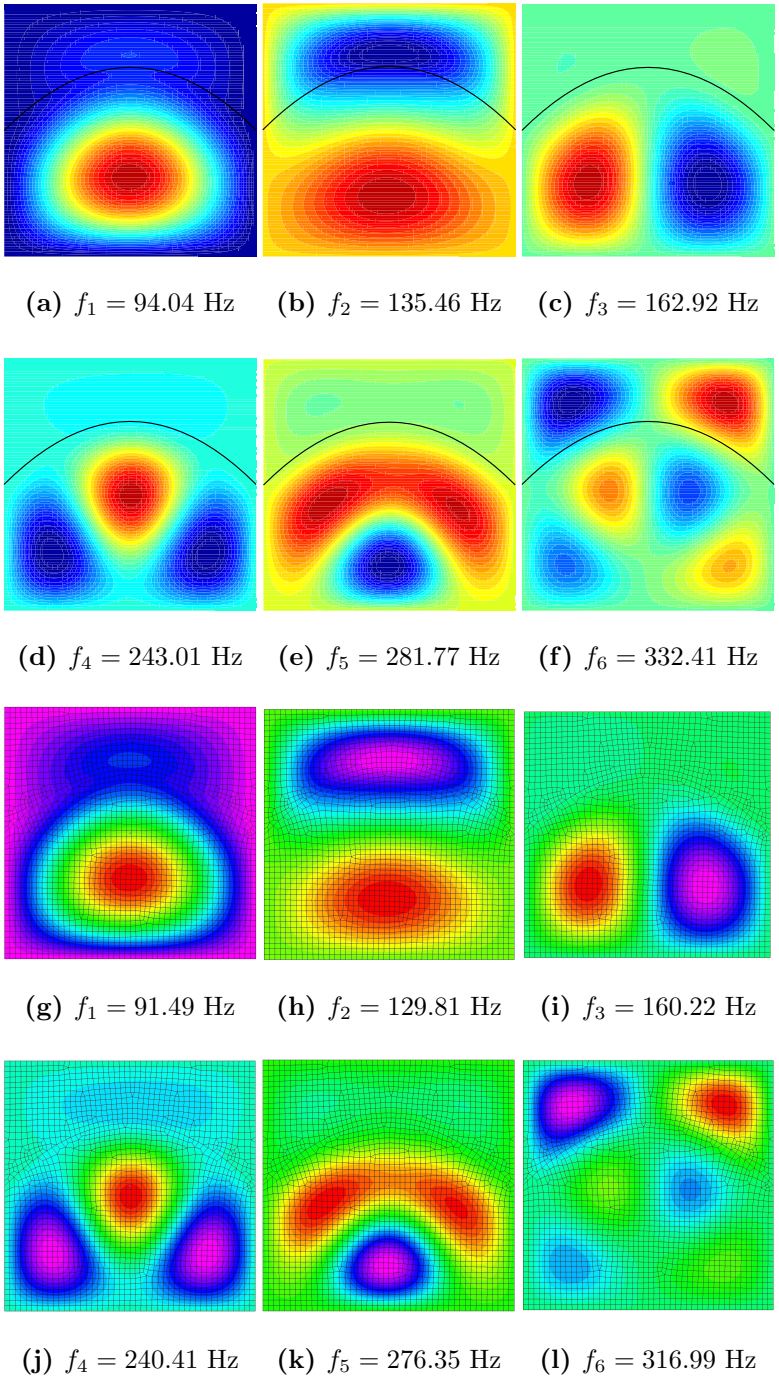

(a) $f_1 = 94.04$ Hz **(b)** $f_2 = 135.46$ Hz **(c)** $f_3 = 162.92$ Hz

(d) $f_4 = 243.01$ Hz **(e)** $f_5 = 281.77$ Hz **(f)** $f_6 = 332.41$ Hz

(g) $f_1 = 91.49$ Hz **(h)** $f_2 = 129.81$ Hz **(i)** $f_3 = 160.22$ Hz

(j) $f_4 = 240.41$ Hz **(k)** $f_5 = 276.35$ Hz **(l)** $f_6 = 316.99$ Hz

Figure 4.14: Mode shapes of the first six natural modes for free-vibration analysis of curvilinearly stiffened plate. Ritz method **(a)**-**(f)**, FEM **(g)**-**(l)**.

the response is now characterized by not null bending deflections. This behaviour is due to the presence of the stiffener offset from the plate midplane, which couples the membrane and flexural behaviour of the structure.

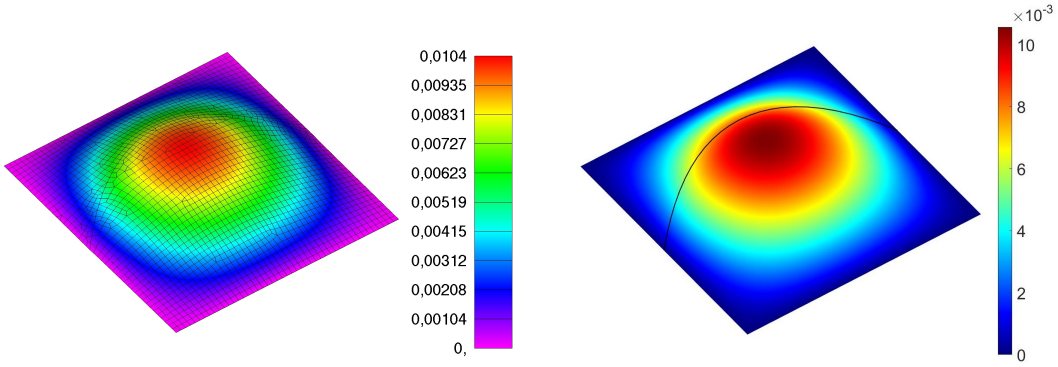

Figure 4.15: Transversal displacement due to beam offset in pre-buckling analysis of curvilinearly stiffened panel.

The membrane forces N_{xx} , N_{yy} , N_{xy}, computed with the present method using 30 polynomials, are reported in Figure 4.16, along with Nastran solutions. It is possible to note that finite elements results are characterized by a clear discontinuity on the stress resultants[10]. This happens because the presence of the beam causes a variation of the structural stiffness which is concentrated along a line. On the other hand, looking at the stress resultants computed with the Ritz method, the gradients near the stiffener are very steep, thanks to the use of high order polynomials but, clearly, the discontinuity cannot be represented using global functions. Moreover the solution is characterized by some low-magnitude oscillations, due to the attempt to replicate with continuous functions (first derivatives of polynomials) the concerned discontinuity (Gibbs phenomenon). The presence of local, spurious oscillation is clearly undesired, and alters the accuracy of the results if one is interested in local values. However, for those cases where the global structural response is of

[10]In finite elements, continuity at the frontier between two elements is assured for displacement, but not for strains and stresses.

concern, this oscillating behaviour tends to be filtered out, and the accuracy of global responses is not compromised.

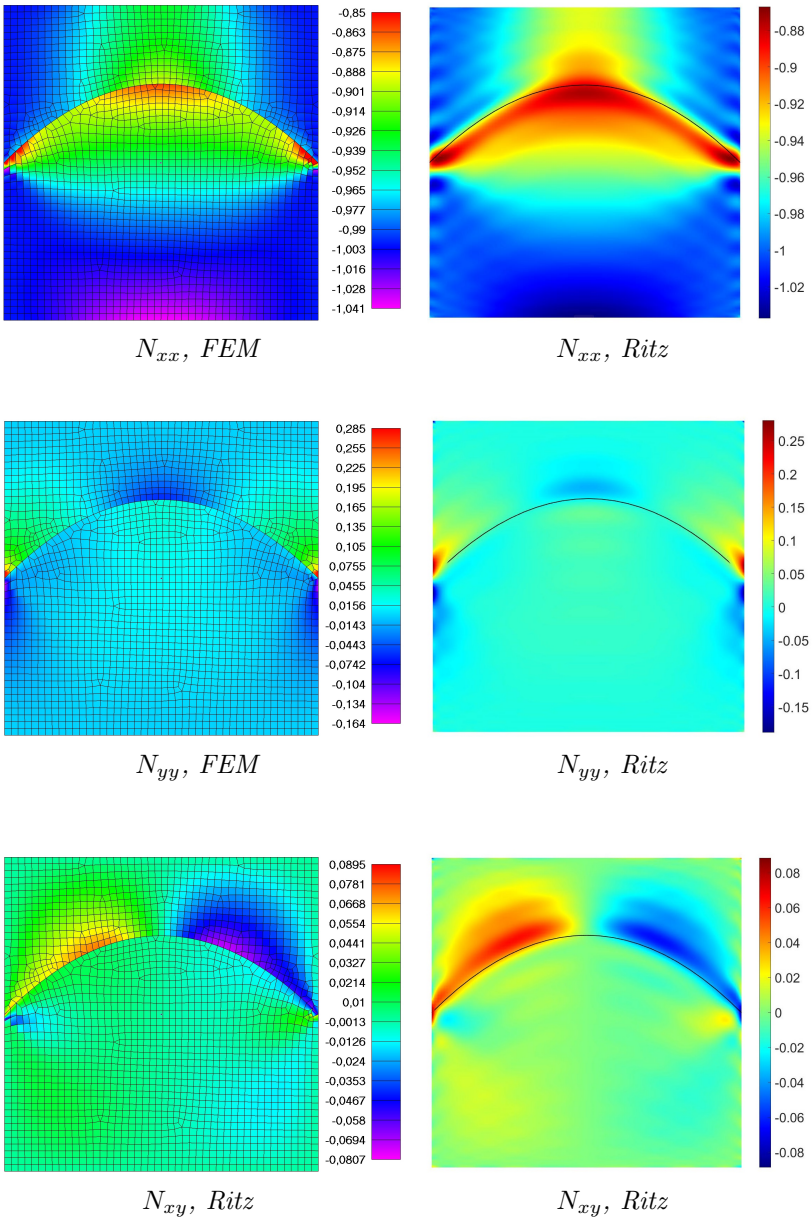

Figure 4.16: Membrane forces (N/mm) resulting from pre-buckling analysis of curvilinearly stiffened panel, in the case of uniaxial compression.

4.1.4 Buckling analysis

4.1.4.1 Single-stringer panel: uniaxial compression and shear

The buckling phase receives in input the results of the pre-buckling analysis to compute the geometric stiffness matrix $\mathbf{K}_G$, and then solves a linear eigenvalue problem to find the critical load. The analyses have been carried out for two different structures, described in Figure 4.17, under uniaxial compression and pure shear loading conditions. The first structure (example 1) is

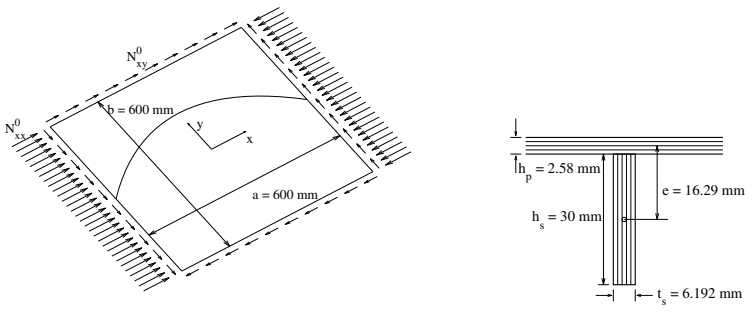

Example 1

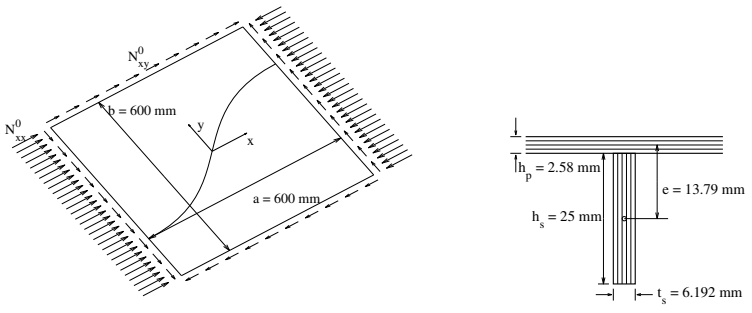

Example 2

Figure 4.17: Geometry of the examples considered for linear buckling analysis.

the stiffened plate considered also in the previous sections. In the second example (example 2) the stringer path is defined by a third order Bézier curve, which requires to set the position of four control points (that is reported in Table 4.6). As it is possible to note, this type of curve description allows to increase the complexity of the stiffener path: the curvature can vary along the curvilinear coordinate s, and inflection points can be present. Neverthe-

less the necessity to define a fourth control point would add two more design variables for every stringer present in the model, challenging the preliminary optimization of the structure. Simply-supported boundary conditions are considered for both the examples.

The results obtained increasing the maximum order of polynomials considered in the analysis are reported in Table 4.7, along with the results computed by Nastran. Again, it is possible to notice that the overall stiffness of the model decreases with increasing the number of polynomials until convergence.

The pre-buckling stress resultants computed using 30 polynomials are reported in Figures 4.18, 4.19 and 4.20, along with finite element results for comparison. Buckling mode shapes for the uniaxial compression and pure shear loading conditions are presented in Figure 4.21. The results of the present method are in good agreement with finite element computations for both the considered example.

	x, mm	y, mm	z, mm
P_0	−300	−150	0
P_1	0	−150	0
P_2	300	150	0
P_3	300	150	0

Table 4.6: Position of the 3^{rd} order Bézier curve control points.

	example 1		example 2	
Polynomials	N_{xx}^{cr}, N/mm	N_{xy}^{cr}, N/mm	N_{xx}^{cr}, N/mm	N_{xy}^{cr}, N/mm
15	32.29	48.01	31.48	39.97
20	32.10	47.62	31.36	39.82
25	32.00	47.38	31.29	39.74
30	31.93	47.25	31.24	39.69
32	31.91	47.21	31.23	39.67
35	31.88	47.16	31.20	39.65
FEM	31.14	46.40	30.74	38.63

Table 4.7: Critical loads for simply supported curvilinearly stiffened plates.

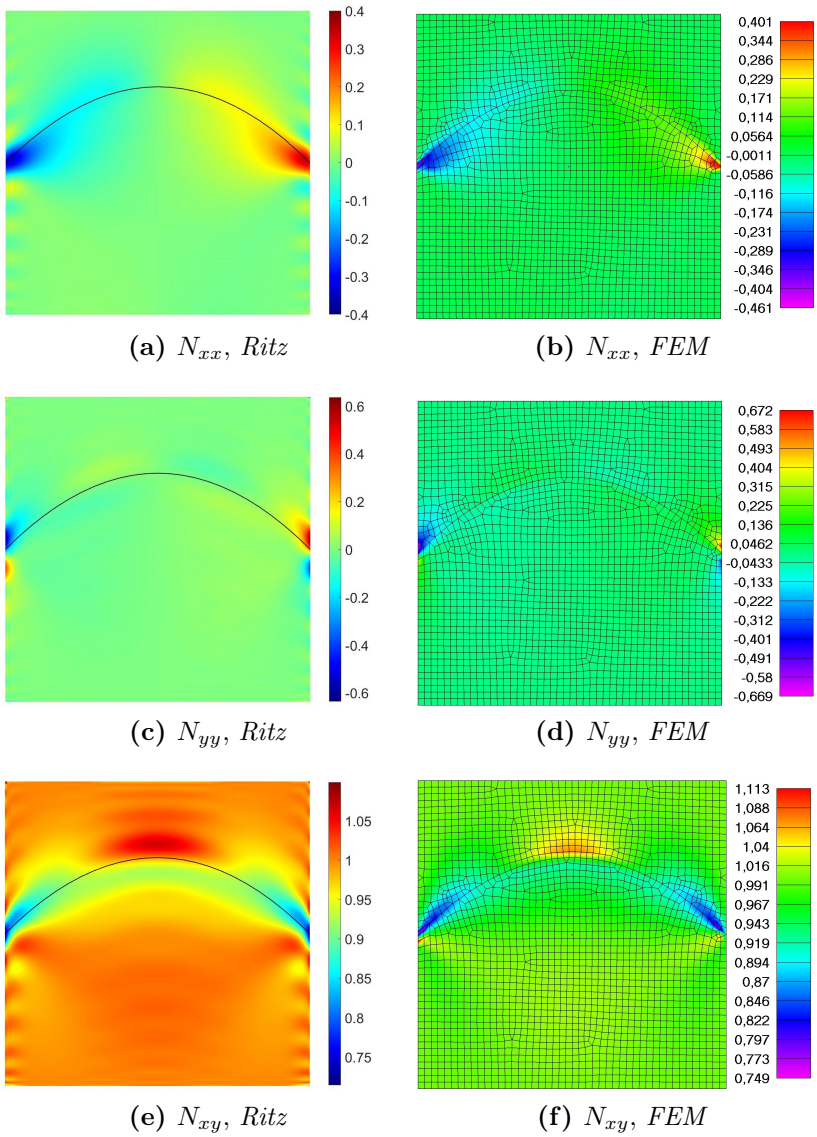

(a) N_{xx}, *Ritz* **(b)** N_{xx}, *FEM*

(c) N_{yy}, *Ritz* **(d)** N_{yy}, *FEM*

(e) N_{xy}, *Ritz* **(f)** N_{xy}, *FEM*

Figure 4.18: Membrane forces (N/mm) resulting from pre-buckling analysis of example 1, in the case of pure shear.

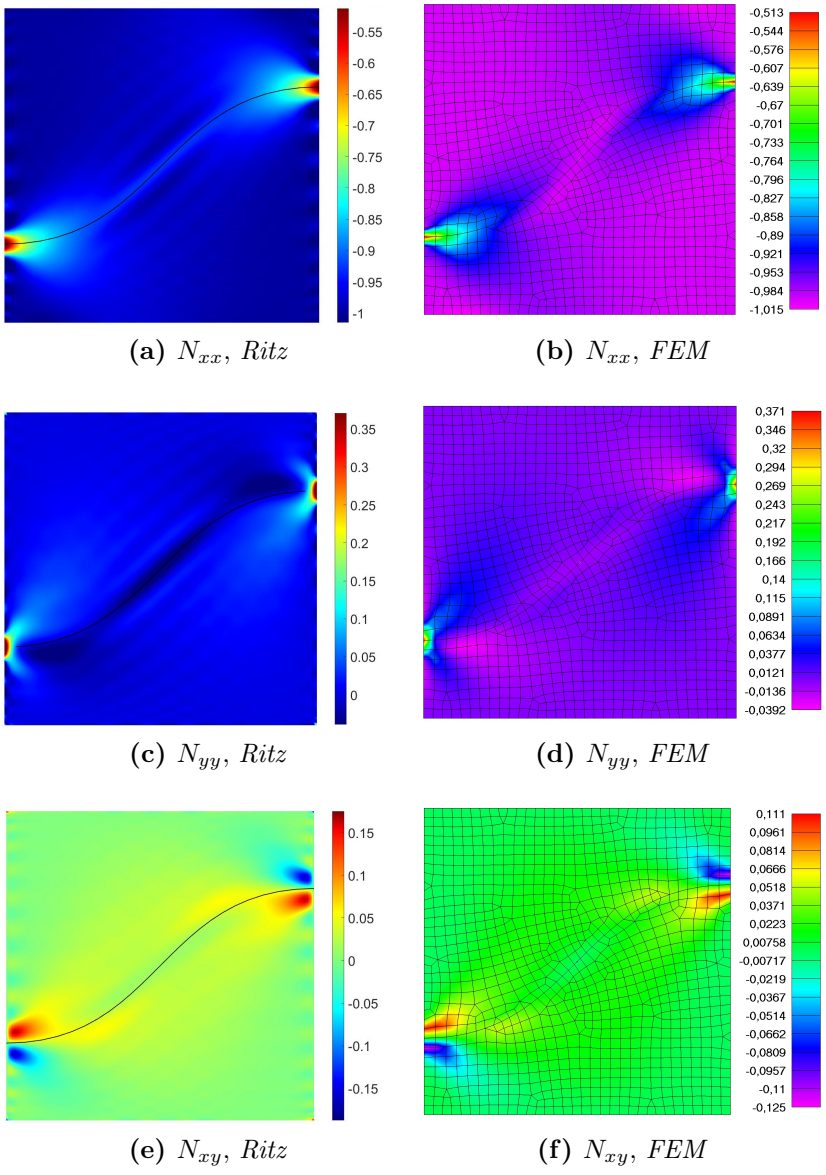

(a) N_{xx}, *Ritz* **(b)** N_{xx}, *FEM*

(c) N_{yy}, *Ritz* **(d)** N_{yy}, *FEM*

(e) N_{xy}, *Ritz* **(f)** N_{xy}, *FEM*

Figure 4.19: Membrane forces (N/mm) resulting from pre-buckling analysis of example 2, in the case of uniaxial compression.

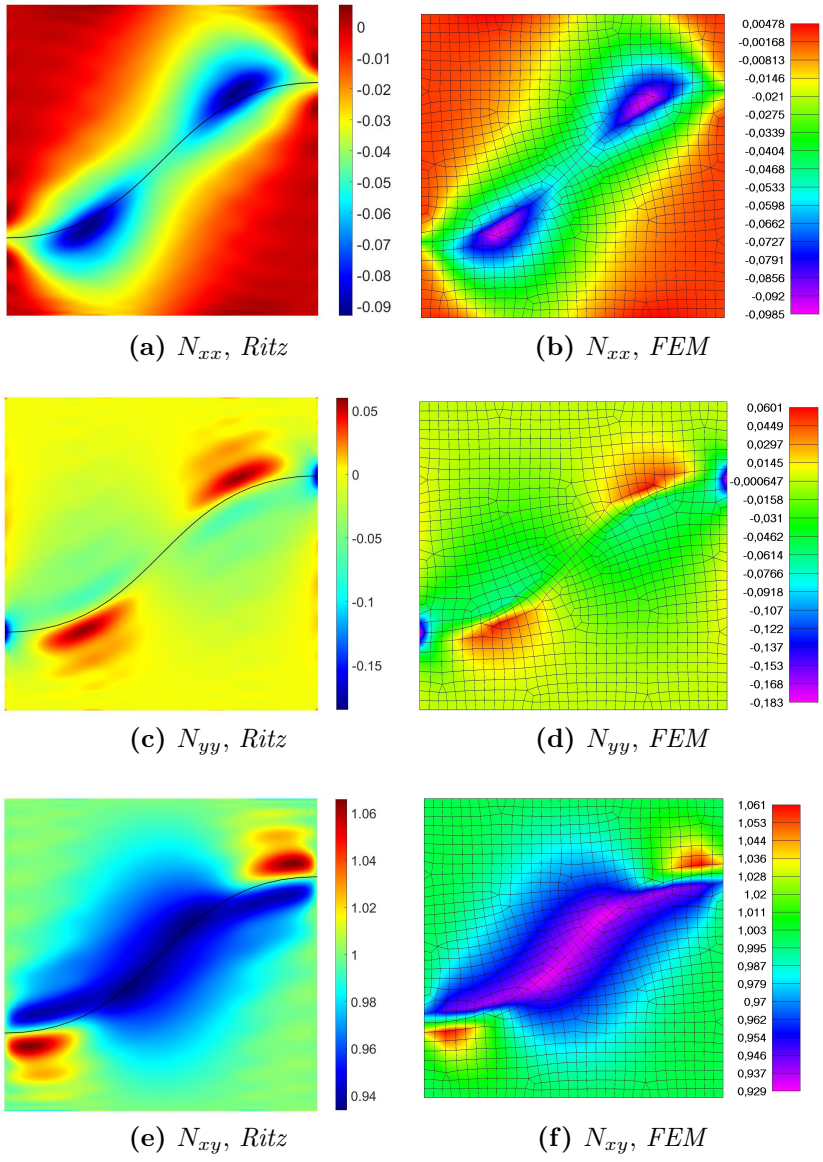

(a) N_{xx}, *Ritz* **(b)** N_{xx}, *FEM*

(c) N_{yy}, *Ritz* **(d)** N_{yy}, *FEM*

(e) N_{xy}, *Ritz* **(f)** N_{xy}, *FEM*

Figure 4.20: Membrane forces (N/mm) resulting from pre-buckling analysis of example 2, in the case of pure shear.

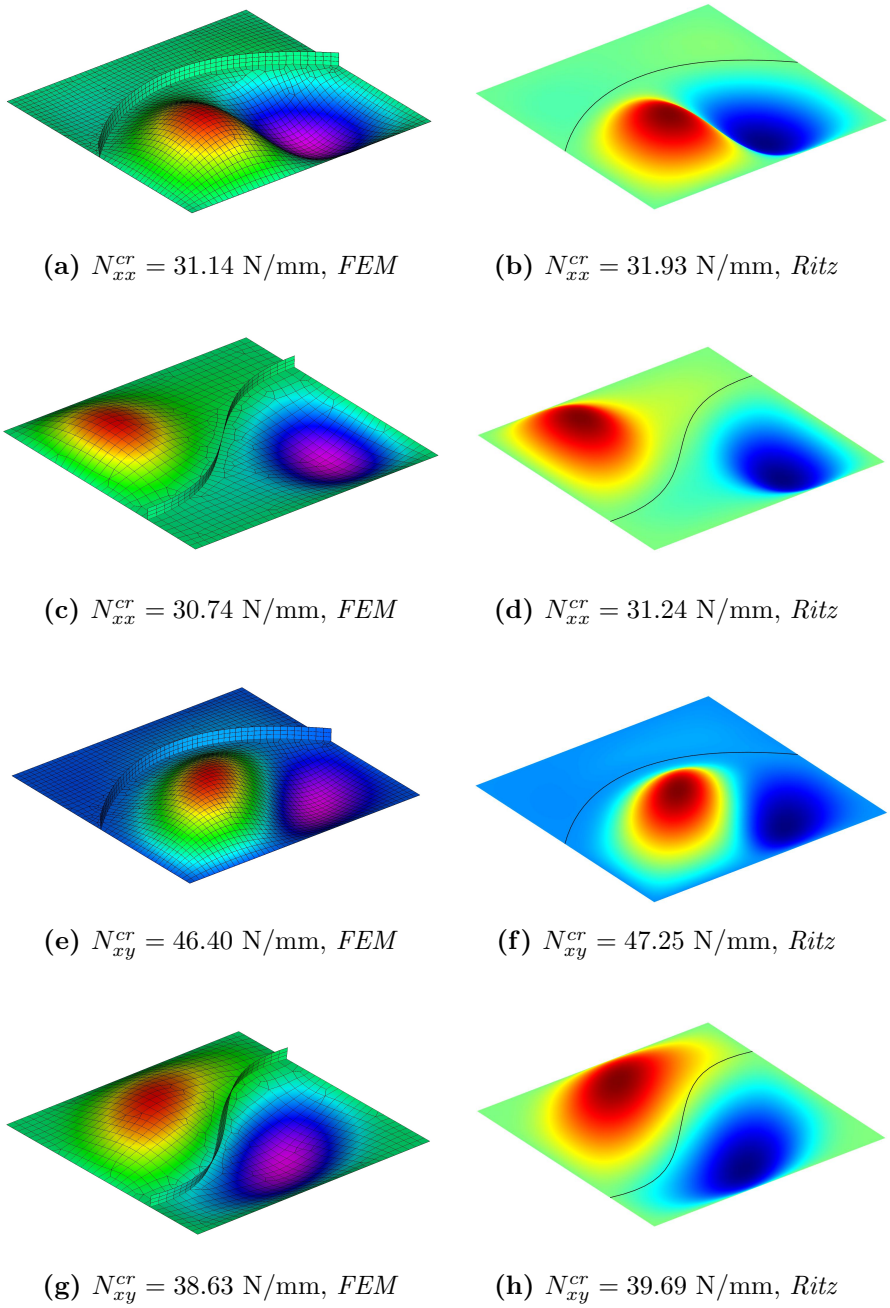

(a) $N_{xx}^{cr} = 31.14$ N/mm, *FEM*

(b) $N_{xx}^{cr} = 31.93$ N/mm, *Ritz*

(c) $N_{xx}^{cr} = 30.74$ N/mm, *FEM*

(d) $N_{xx}^{cr} = 31.24$ N/mm, *Ritz*

(e) $N_{xy}^{cr} = 46.40$ N/mm, *FEM*

(f) $N_{xy}^{cr} = 47.25$ N/mm, *Ritz*

(g) $N_{xy}^{cr} = 38.63$ N/mm, *FEM*

(h) $N_{xy}^{cr} = 39.69$ N/mm, *Ritz*

Figure 4.21: Mode shapes for simply supported curvilinearly stiffened plates under uniaxial compression **(a-d)** and pure shear **(e-h)** load conditions.

4.1.4.2 Three-stringer panel: combined loads

In this section the general case with more than one curvilinear stringer is considered for linear buckling analysis with combined loading condition. The plate is clamped at all its edges and stiffened by three curvilinear stringers which control points are reported in Table 4.8. A sketch of the problem is reported in Figure 4.22. The analyses are conducted gradually increasing the parameter γ defined as:

$$\gamma = \frac{N^0_{xy}}{N^0_{xx}} \tag{4.125}$$

Also in this case the finite element model of the stringers is performed using 2D shell elements, and Ritz analysis has been carried out using 30 polynomials. The comparison between finite element and present method results is reported in Table 4.9. By increasing the amount of shear the critical compression load decreases for both the methods with a nearly constant difference of 3.5%. The Ritz method, again, slightly overestimates the stiffness of the structure compared to finite element solutions, but without compromising the accuracy of the results. Stress resultants of pre-buckling analysis obtained for $\gamma = 1$ are reported in Figure 4.23, while the corresponding mode shape is shown in Figure 4.24.

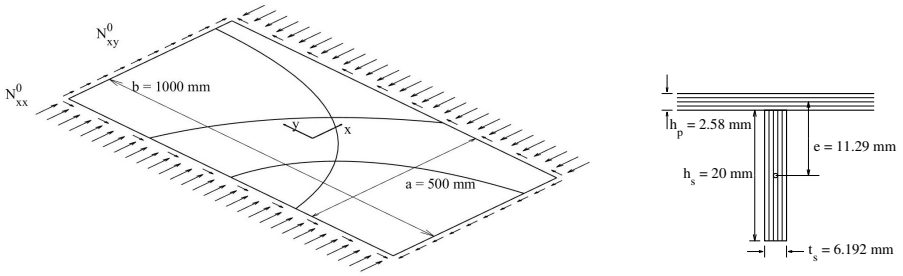

Figure 4.22: Geometry of the composite plate stiffened by three curvilinear stringers.

	stringer 1		stringer 2		stringer 3	
	x, mm	y, mm	x, mm	y, mm	x, mm	y, mm
P_0	−250	250	−250	0	−250	−200
P_1	50	150	50	−50	200	−100
P_2	250	−150	150	−500	200	500

Table 4.8: Position of the control points for the case of the panel stiffened by three curvilinear stiffeners.

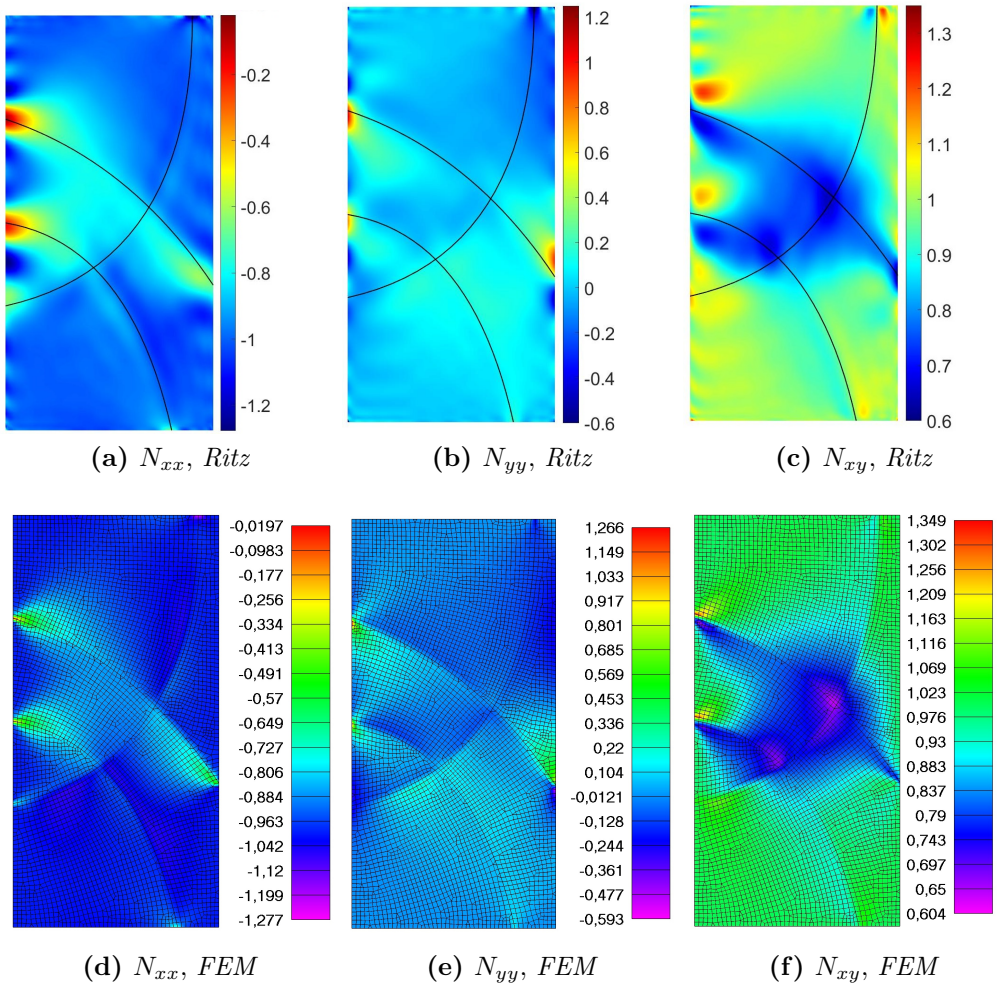

(a) N_{xx}, *Ritz* **(b)** N_{yy}, *Ritz* **(c)** N_{xy}, *Ritz*

(d) N_{xx}, *FEM* **(e)** N_{yy}, *FEM* **(f)** N_{xy}, *FEM*

Figure 4.23: Membrane forces (N/mm) resulting from pre-buckling analysis of the plate with three stiffeners.

γ	N_{xx}^{cr}, N/mm		
	Ritz	FEM	diff %
0.0	51.49	49.71	3.58
0.1	51.28	49.56	3.47
0.2	50.75	49.01	3.55
0.3	49.95	48.30	3.42
0.4	48.94	47.32	3.42
0.5	47.79	46.19	3.46
0.6	46.54	44.97	3.49
0.7	45.22	43.69	3.50
0.8	43.88	42.39	3.51
0.9	42.54	41.08	3.55
1.0	41.21	39.80	3.54

Table 4.9: Results for linear buckling of the composite panel stiffened by three curvilinear stringers under combined loading conditions.

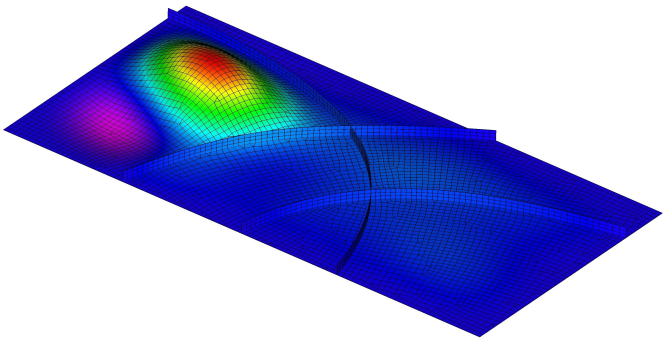

$N_{xx}^{cr} = 39.80$ N/mm, *FEM*

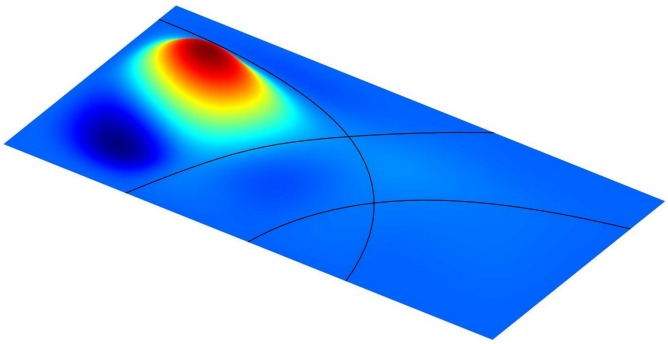

$N_{xx}^{cr} = 41.21$ N/mm, *Ritz*

Figure 4.24: Mode shape of clamped composite panel stiffened by three curvilinear stringers under combined loading condition with $\gamma = 1$.

4.1.4.3 Panel with run-out

The reduction of the transverse area of an aircraft wing or fuselage causes modifications in the number of stringers along the longitudinal direction. This can lead to the abrupt interruption of one or more stringers before they reach the opposite edge of the panel. Using the present method such situation can be easily modelled through an appropriate choice of the control points for stiffener path parametrization. In particular it is sufficient to set the position of P_0 or P_2 (or P_3 if third order curves are considered) to lie inside the plate domain. The case of a composite plate stiffened by two straight stiffener (that can be modelled simply aligning the control points) is illustrated in Figure 4.25. One of them is interrupted at $x = 0$. The panel undergoes combined load condition with $\gamma = 0.5$, where gamma is defined according to Eq. 4.125.
The results of pre-buckling analysis are illustrated in Figure 4.26 in terms of membrane resultants. The obtained buckling mode shape is shown in Figure 4.27, along with the value of the critical load. Also in this case the present method provides an excellent accuracy-to-degrees of freedom ratio, demonstrating close agreement with finite element calculations. In the following sections it will be shown how the modification of the uninterrupted stringer's path can increase the value of the critical load.

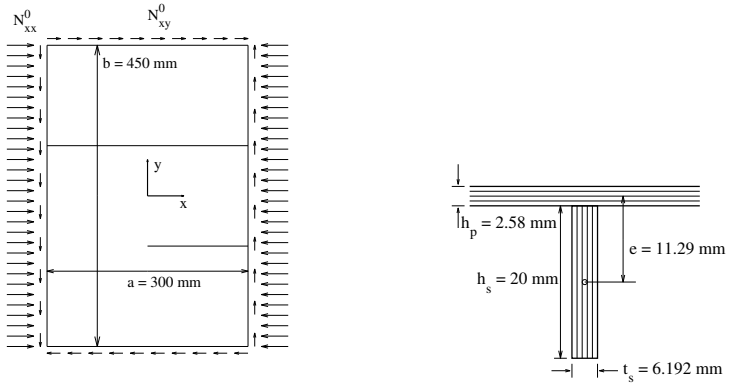

Figure 4.25: Geometry of the test case of stiffened composite panel with run-out.

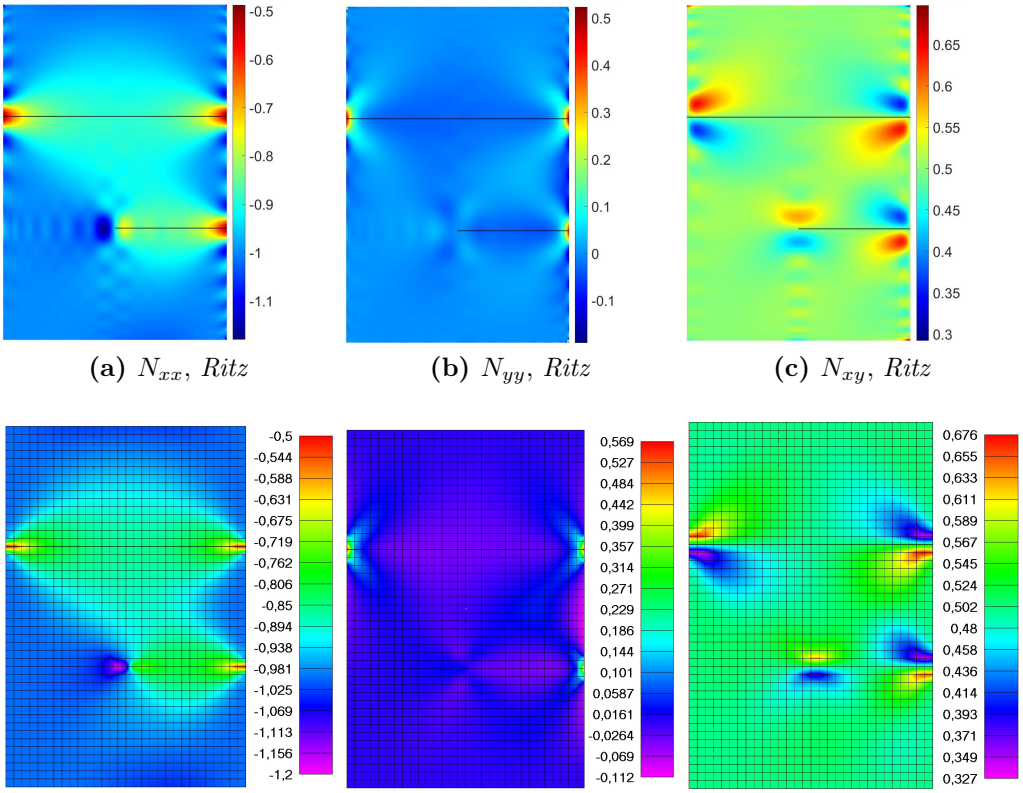

(a) N_{xx}, *Ritz* **(b)** N_{yy}, *Ritz* **(c)** N_{xy}, *Ritz*

(d) N_{xx}, *FEM* **(e)** N_{yy}, *FEM* **(f)** N_{xy}, *FEM*

Figure 4.26: Membrane forces (N/mm) resulting from pre-buckling analysis of the plate with run-out.

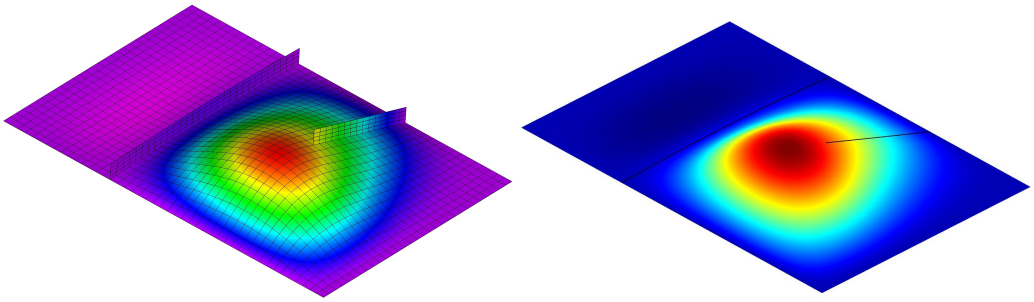

$N_{xx}^{cr} = 70.04$ N/mm, *FEM* $N_{xx}^{cr} = 70.78$ N/mm, *Ritz*

Figure 4.27: Buckling mode of stiffened composite panel with run-out under combined load with $\gamma = 0.5$.

4.2 Parametric studies

One of the most interesting aspects associated with the Ritz method relies in the ease to perform parametric analyses and sensitivity studies. Indeed, the almost null modelling time along with the reduced effort to solve the structural problem make the procedure particularly suitable for these kind of investigations. In the case of curvilinearly stiffened panels, this feature is even more appealing, as far as the structural response can be, in a somewhat manner, less predictable due to the inherent complexity of the panels: the analyst can hardly say in advance how, for instance, the buckling load will be affected by the stringer path. The availability of an efficient tool is thus of crucial importance to gather insight into the effect of the various design parameters.

4.2.1 Vibrations with pre-stress

The presence of the geometric stiffness $\mathbf{K}_G$ in the eigenvalue problem in Eq. 3.123 lead to vibration with pre-stress problem. Due to the linearity of the system the geometric stiffness due to a load $\lambda\mathbf{P}^0$ is simply $\lambda\mathbf{K}_G$. Then solving the eigenvalue problem:

$$\left[-\omega^2\,\mathbf{M} + (\mathbf{K} + \lambda\mathbf{K}_G)\right]\mathbf{a} = \mathbf{0} \tag{4.126}$$

it is possible to study the change of the natural frequencies varying the value of λ and so the pre-stress applied. This study has been performed on the example in Figure 4.9 under uniaxial compression load N^0_{xx}. The free-vibration problem has been solved in section 3.1.2, while the critical load can be found in Table 4.7 (example 1).
The results are shown in Figure 4.28, where the first four natural frequencies are plotted in function of the adimensional parameter λ/λ_{cr}. The in-plane compression may have two main effects on the free vibrations of the stiffened plate: it can change the natural frequency and it may change the corresponding mode shape. It can be seen that, as expected, an increase in magnitude of the in-plane loads reduces the natural frequencies. On the

contrary when the applied load is tensile ($\lambda < 0$) the natural frequencies increase. When $\lambda/\lambda_{cr} = 0$ no prestress is applied and the results are equal to the free-vibration problem ones. The first natural frequency become zero when the in-plane load is equal to the critical buckling load of the stiffened plate. Moreover it is possible to see how the second and third frequencies get close each other until they reach the same value for $\lambda/\lambda_{cr} = 0.38$. In this point the second mode shape switches to the third, and the third mode shape switches to the second. The same thing happens between first and second modes at about $\lambda/\lambda_{cr} = 0.9$. The shapes of mode 2 for three different values of λ/λ_{cr} are reported in Figure 4.29.

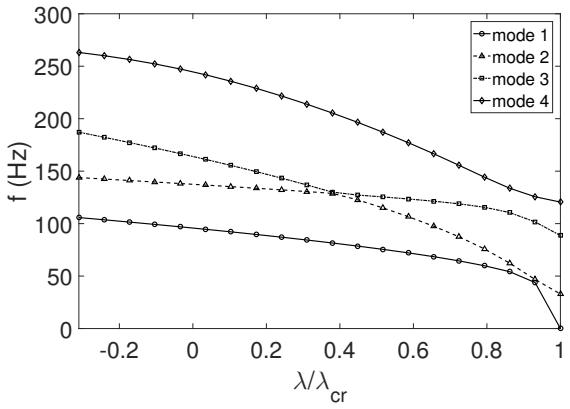

Figure 4.28: Effect of the pre-load on the first four frequencies for curvilinearly stiffened plate.

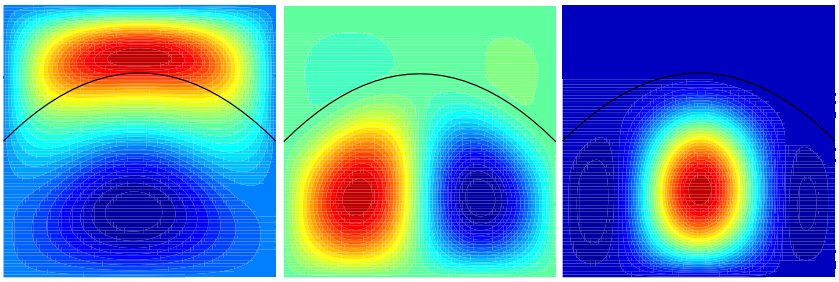

$\lambda/\lambda_{cr} = 0.2$ $\lambda/\lambda_{cr} = 0.6$ $\lambda/\lambda_{cr} = 1$

Figure 4.29: Shape of the second mode of curvilinearly stiffened plate for different values of pre-load.

4.2.2 Effect of the stiffener height h_s and offset e on the critical load

In this section the variation of the critical load with stiffener height is studied for the example 1 of section 3.1.4.1. Both uniaxial compression and pure shear load cases are considered and the study has been performed with and without taking into account the beam offset from the plate midplane.
The trend of the critical load for increasing values of stiffeners height is reported in Figure 4.30 . Both the cases with $e = 0$ and $e \neq 0$ are considered. The study carried out using finite elements (in this case no geometry updating is needed if the stiffener is modelled with beam elements) is also reported to assure the truthfulness of the predictions.
As it is possible to see, the plots can be divided into three regions, identified by two changes on the trend slope. In the first region the height of the stiffener is small, so that the bending energy to lift the stiffener in the out-of-plane direction is relatively small and the structures acts approximately like an unstiffened composite plate; the mode shape is global.
In the second region the energetic contribute of the stiffener in the internal work begins to be important and the critical load increases rapidly; modifications on the mode shape are visible but it remains global.

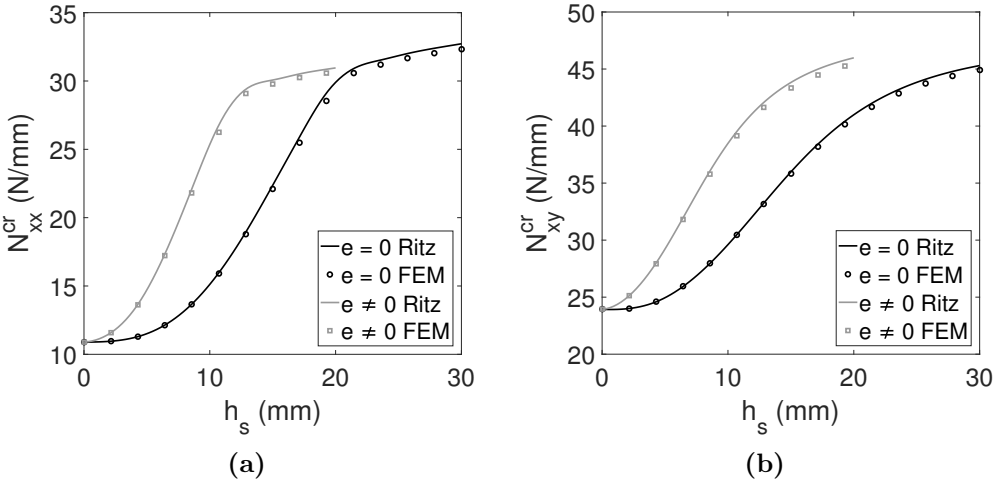

Figure 4.30: Variation of the critical load of curvilinearly stiffened panel with the stiffener height for uniaxial compression **(a)** and pure shear **(b)** loading conditions.

In the third region the stringer bending stiffness is large enough to promote a local mode and the rise of the critical load is slowed down. The effect of the beam offset is the increment of the slope and the anticipation of the switching from one region to the other one. This last phenomenon is more evident in the uniaxial compression case as it is possible to see in Figure 4.31, where mode shapes are shown for different values of h_s and e.

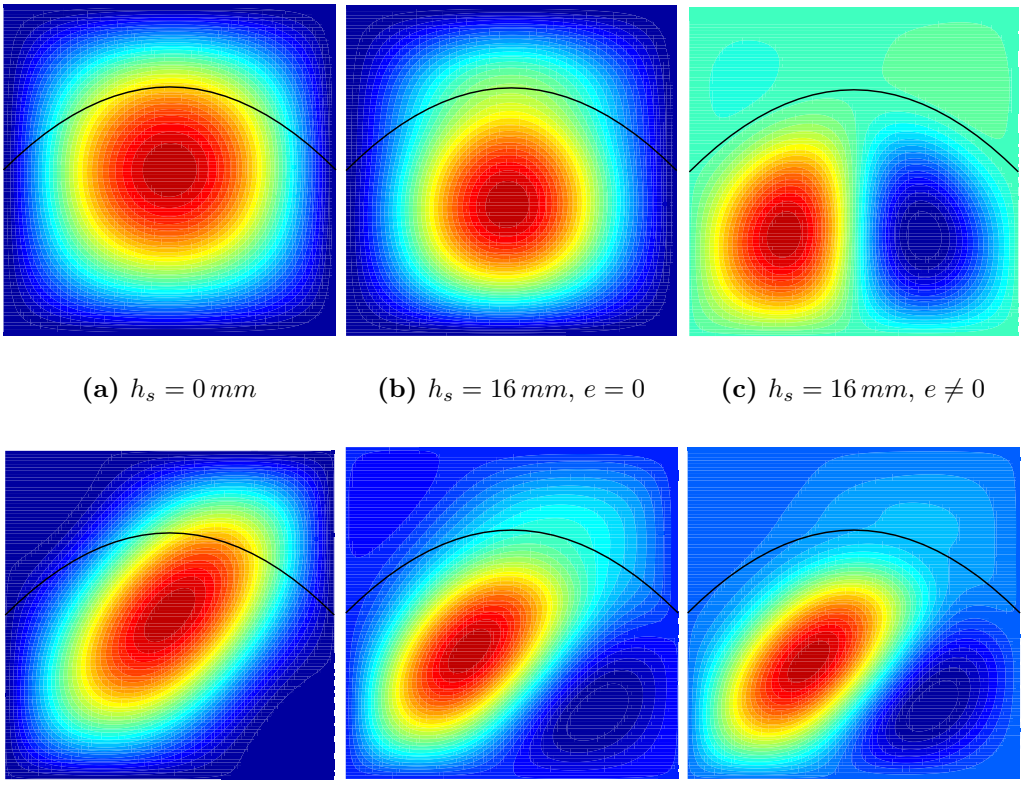

(a) $h_s = 0\,mm$ **(b)** $h_s = 16\,mm$, $e = 0$ **(c)** $h_s = 16\,mm$, $e \neq 0$

(d) $h_s = 0\,mm$ **(e)** $h_s = 16\,mm$, $e = 0$ **(f)** $h_s = 16\,mm$, $e \neq 0$

Figure 4.31: Buckling mode shapes of curvilinearly stiffened panel for different values of stiffener height and offset, for uniaxial compression **(a-c)** and pure shear **(d-f)**.

4.2.3 Effect of the stiffeners geometric curvature on the critical load of stiffened panel under uniaxial compression load

In this section the effect of stiffener curvature on the critical load for the example shown in Figure 4.32 is investigated. Linear buckling analysis is performed varying the couple of parameters $(\alpha\,, d\,)$ defining the geometry of the problem, which is symmetric with respect to the x axis. As shown in Figure 4.32, α controls the position along y of starting and ending points of the stiffeners, while d is the distance with sign between control point P_1, which position along x is fixed at $x = 0$, and the line joining the other two control points. In such way this parameter gives a measure of the curvature of the stringers (when $d = 0$ they are straight). The first study has been

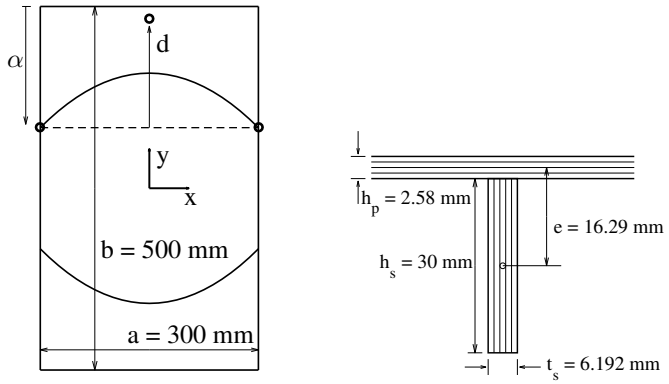

Figure 4.32: Geometry of the model used to investigate the effect of stiffeners geometric curvature on the stability behaviour of the structure.

conducted for the uniform uniaxial compression load case. The sensitivity of the present method to the optimal solution, with varying the maximum order of polynomials considered in the analysis, has been assessed keeping track of the value of d assuring the maximum critical load. The result of the sensitivity study is reported in Figure 4.33a, where the value of d corresponding to the best configuration is plotted for an increasing number of trial functions. As it can be noted, the optimum is reached quite fast and the parametric analyses can be performed with reasonable number of polynomials. For this

study $R = S = 16$ has been chosen.

The value of the critical load is plotted in Figure 4.34 for different values of paramters d and α. The graph shows that the maximum critical load is achieved with the traditional structural solution with evenly-spaced straight stiffener ($\alpha = b/3\,, d = 0\,$). On the other hand, a solution with curvilinear stringers is found to be beneficial whenever the distribution of the stiffeners differs from the evenly-spaced one, as the peak of each curve is reached when $d \neq 0$.

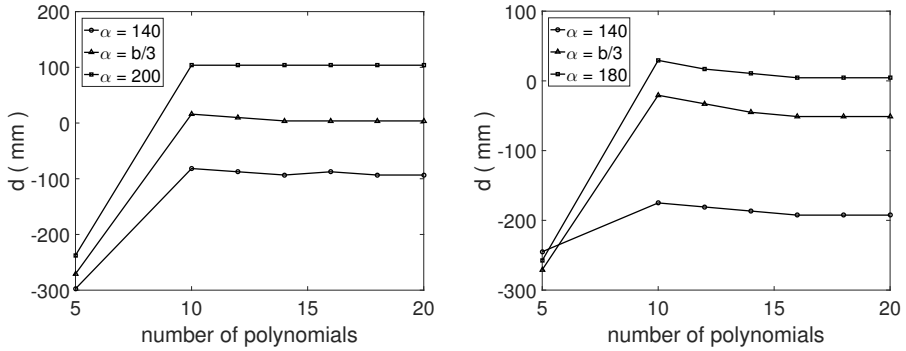

Figure 4.33: Sensitivity study of stiffened composite panel under uniform **(a)** and parabolic **(b)** uniaxial compression.

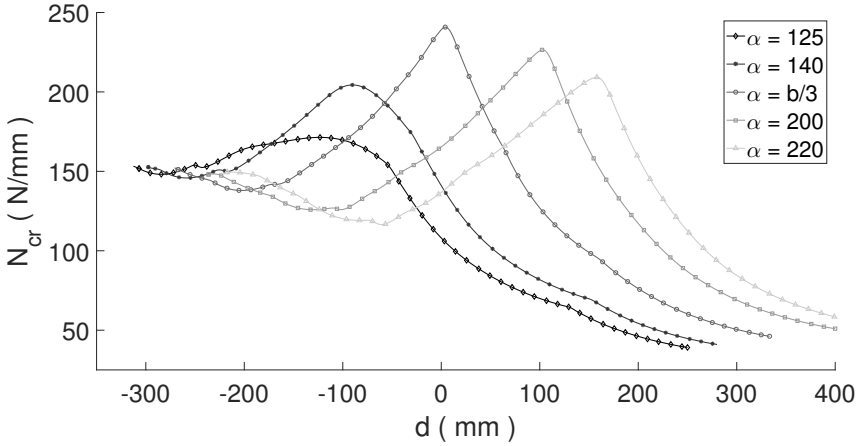

Figure 4.34: Effect of the curvature on the critical load of stiffened composite panel under parabolic uniaxial compression.

Another study has been performed in the case of variable uniaxial compression. In this example the applied membrane force N^0_{xx} varies with the parabolic law:

$$N^0_{xx}(y) = 1 - \frac{4}{b^2}\, y^2 \tag{4.127}$$

which reaches its maximum value for $y = 0$ and goes to zero at $y = \pm b/2$. As done for the previous example, a sensitivity study precedes the analyses. Figure 4.33b shows that also in this case the optimal configuration can be accurately computed with a number of polynomials $R = S = 16$. The results, reported in Figure 4.35, offer different conclusions from the previous example. In this case the highest value of the critical load for the evenly-spaced configuration is reached with curvilinear stiffeners, that can increase significantly the value of the critical load with respect to the straight stringers solution. The global optimum is still achieved using straight stiffeners, but for values of α different from $b/3$. The mode shapes of the optimum solutions are reported in Figure 4.36 and 4.37 for some values of α and d, for both the load case considered. It can be noted that the curvature of the stringers can cause global mode shapes that in some application (for example aircraft wing skin) are not allowed. An increment of the beam stiffness is needed, and it can be obtained, for example, by changing the lamination sequence of the stiffeners or increasing their cross section, as seen in the previous section.

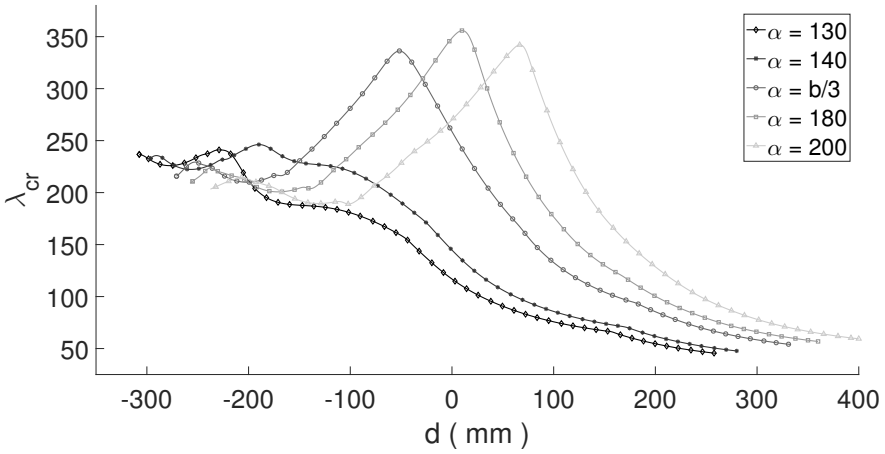

Figure 4.35: Effect of the curvature on the critical load of stiffened composite panel under parabolic uniaxial compression.

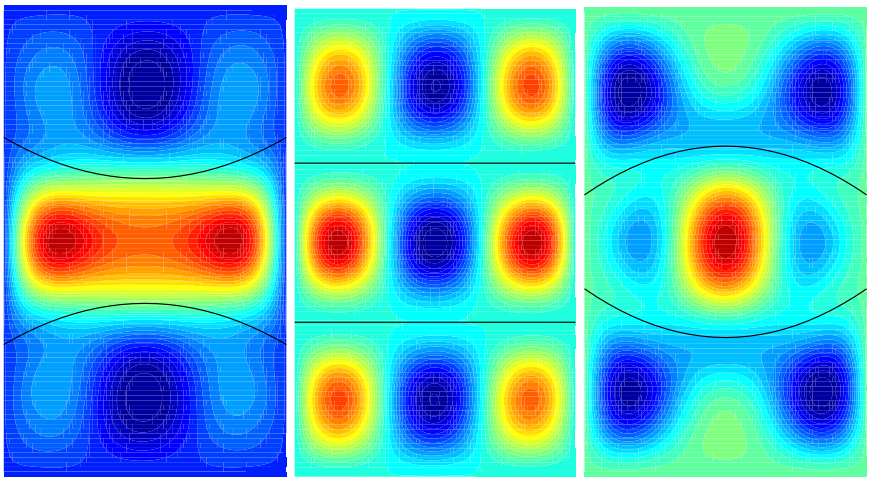

(a) α = 140, d = -87.5 **(b)** α = b/3, d = 0 mm **(c)** α = 200, d = 103.8

Figure 4.36: Buckling mode shape of stiffened composite panel under uniform uniaxial compression with different values of stiffeners spatial distribution α (mm) and geometric curvature parameter d (mm).

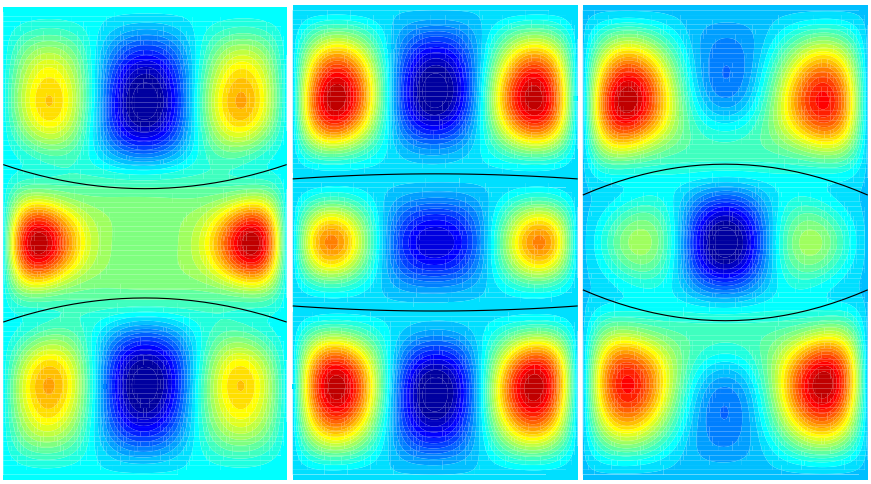

(a) α = b/3, d = -51.1 **(b)** α = 180, d = 10.7 **(c)** α = 200, d = 65.2

Figure 4.37: Buckling mode shape of stiffened composite panel under parabolic uniaxial compression with different values of stiffeners spatial distribution α (mm) and geometric curvature parameter d (mm).

4.2.4 Effect of the stiffener geometric curvature on the critical load of stiffened panel with run-out

As observed in Section 3.1.6, there are cases in which one or more stringers are interrupted due to the reduction of the wing transverse area. In this section the example in Figure 4.38 will be used to perform a study on the effect of the stiffener curvature in this particular application.
The run-out can be performed mainly in two ways. A first possibility is to interrupt the stringer path in correspondence of the rib (see the works of Cosentino and Weaver [35],[36]). The presence of ribs and spars is modelled in the present method by imposing the essential boundary conditions at the edges of the plate, meaning that in this case the stiffener is interrupted outside the plate domain ad it's not part of the model. The mode shape in this condition is reported in Figure 4.39a, along with the value of the critical load. As expected, the stability behaviour is driven by the presence of a large portion of the panel that remains unstiffened. This lead to the decline of the critical load. In order to obviate this problem - which leads to the need to increase the panel thickness and, consequently, the weight of the structure - a common practice is to extend the path of the stiffener within the plate domain. Figure 4.39b shows the mode shape and the critical load in this new condition. As it can be noted this solution increases the stability performance of the panel.
The aim of this section is to understand if a change on the path of the uninterrupted stiffener can have a positive effect on the stability of the panel with run-out.
The path of the stringer is defined by the following relations:

$$\begin{aligned} \mathbf{P}_0 &= \begin{pmatrix} -\frac{a}{2} & y_{P_0} \end{pmatrix} \\ \mathbf{P}_1 &= \begin{pmatrix} x_{P_1} & y_{P_1} \end{pmatrix} \\ \mathbf{P}_2 &= \begin{pmatrix} \frac{a}{2} & \frac{b}{8} \end{pmatrix} \end{aligned} \tag{4.128}$$

where y_{P_0}, x_{P_1}, and y_{P_1} are three design variables taken from a dense-enough set of values. A Linear buckling analysis is performed for all the possible

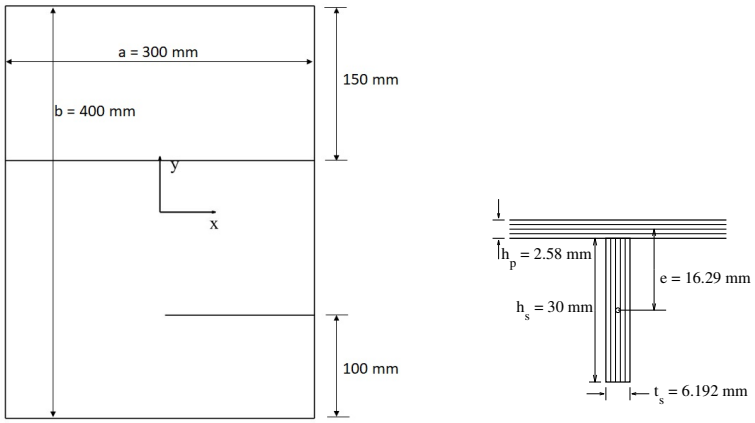

Figure 4.38: Description of the geometry of the panel with run-out.

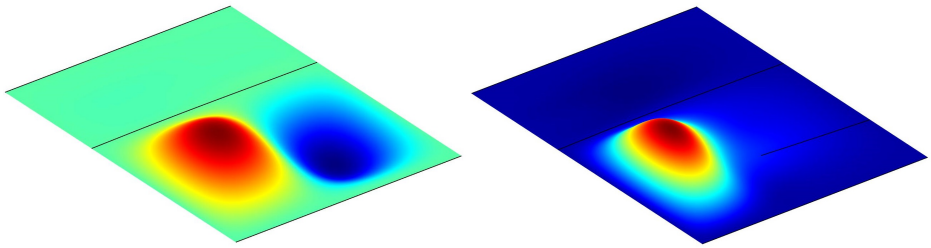

(a) $N_{xx}^{cr} = 95.10$ N/mm **(b)** $N_{xx}^{cr} = 116.93$ N/mm

Figure 4.39: Buckling results for panel with run out. In **(a)** the stiffener is interrupted on the plate edge. In **(b)** the stiffener is interrupted within the plate domain to increase the stability performance.

combinations for both the examples shown in Figure 4.39. The results of the best configuration founded for both the examples are reported in Figure 4.40. In both cases a variation of the uninterrupted stiffener path can increase the value of the critical load. It is worth noting how similar results to those obtained extending the path of the interrupted stiffener (Figure 4.39b) can be achieved employing only one curvilinear stiffener. It should be pointed out that these results are not obtained using an optimization technique. Consequently, configurations in Figure 4.40 may not be the optimal ones. The employment of a global optimization algorithm may allows to achieve a deeper investigation of the design space and better configurations may be founded.

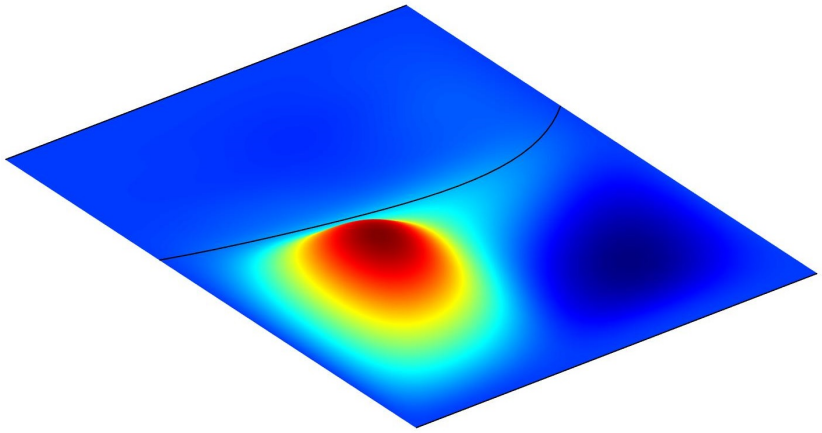

(a) $N_{xx}^{cr} = 128.57$ N/mm

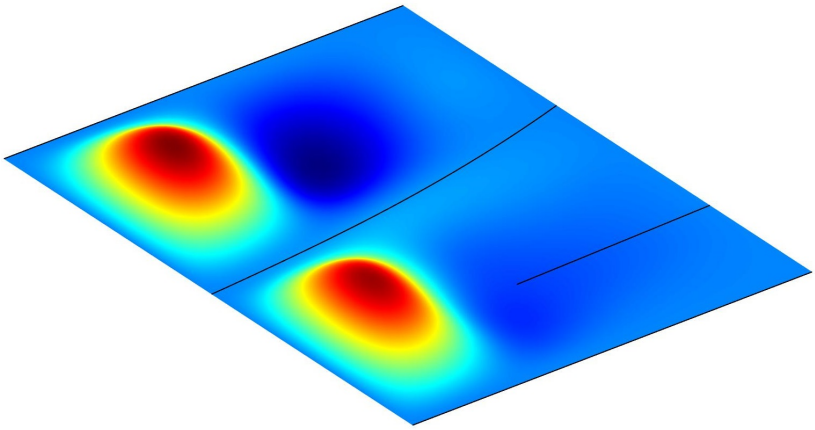

(b) $N_{xx}^{cr} = 166.15$ N/mm

Figure 4.40: Best configurations for the stiffened plate with run-out (case **(a)**: $y_{P_0} = 4.44\,mm$, $y_{P_1} = -50\,mm$, $x_{P_1} = 90\,mm$; case **(b)**: $y_{P_0} = -3.33\,mm$, $y_{P_1} = 4.44\,mm$, $x_{P_1} = 10.0\,mm$).

5. Application to wing-box skin

In the previous sections it has been shown how the geometry of the problem, and the load condition considered, can affect the optimal configuration and the stability performance of composite stiffened panel. Curvilinear stiffeners can be a good solution, for the case of uniform compression, when the stiffeners are not evenly-spaced in the plate surface. At the same time, buckling performance of evenly-spaced configurations can be improved when the applied loads are variable along the edges of the plate. Moreover, when the structure involves the presence of run-out, a curvilinear solution for the uninterrupted stiffeners may increase the stability performance of the structure. These results suggest that the effect of the stringers curvature is very case-dependent, and any conclusion on the convenience of using curvilinear stiffeners can be taken only in relation to their real application. For these reasons further studies were conducted on a composite stiffened panel resulting from a preliminary sizing of an aircraft wing box.

5.1 Description of the reference aircraft

The aircraft taken as reference is based on the NASA Common Research Model (CRM) that has been created in order to provide a standardized model for comparison of computational fluid dynamic codes with experimental data [37]. The mission defined for this aircraft is similar to a Boeing wide body commercial transport aircraft[11], with gross vehicle weight (GVW) 225000 Kg [38]. The cruise speed is 252 m/s at 35000 ft with a Mach number of 0.85. Wing dimensions are taken from the provided CAD file (illustrated in Fig-

[11] E.g. Boeing 777-200.

wing span	$60\,m$
root chord	$11.8\,m$
tip chord	$2.7\,m$
mean aerodynamic chord	$7\,m$

Table 5.10: NASA CRM wing characteristic dimensions.

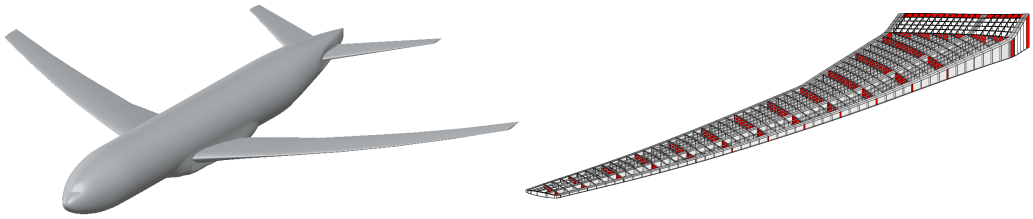

(a) **(b)**

Figure 5.41: Geometry **(a)** and wing FEM model **(b)** of NASA Common Research Model.

ure 5.41a) and are reported in Table 5.10.

5.2 Preliminary sizing

5.2.1 Estimation of the loads

The estimation of the loads is carried out performing an aeroelastic analysis. To this aim a stick airframe model and an aerodynamic panel-based model are developed in Nastran environment.
For this work, the provided isotropic aluminum based finite element model of the wing-box, shown in Figure 5.41b, is used to take informations about the structural solution in terms of spars and skin thickness, stiffener and spar-cap dimensions, and distance between ribs. The adopted configuration consists in a double-cell wing-box, with stringers parallel to the midspar. All these informations, along with the adopted material properties, are necessary to estimate the cross section mechanical properties, which are used to develop the stick airframe model. It should be pointed out that, for this preliminary estimation of the loads, an isotropic-based structural model has to be used since no composite solutions are provided. The cross-section properties are

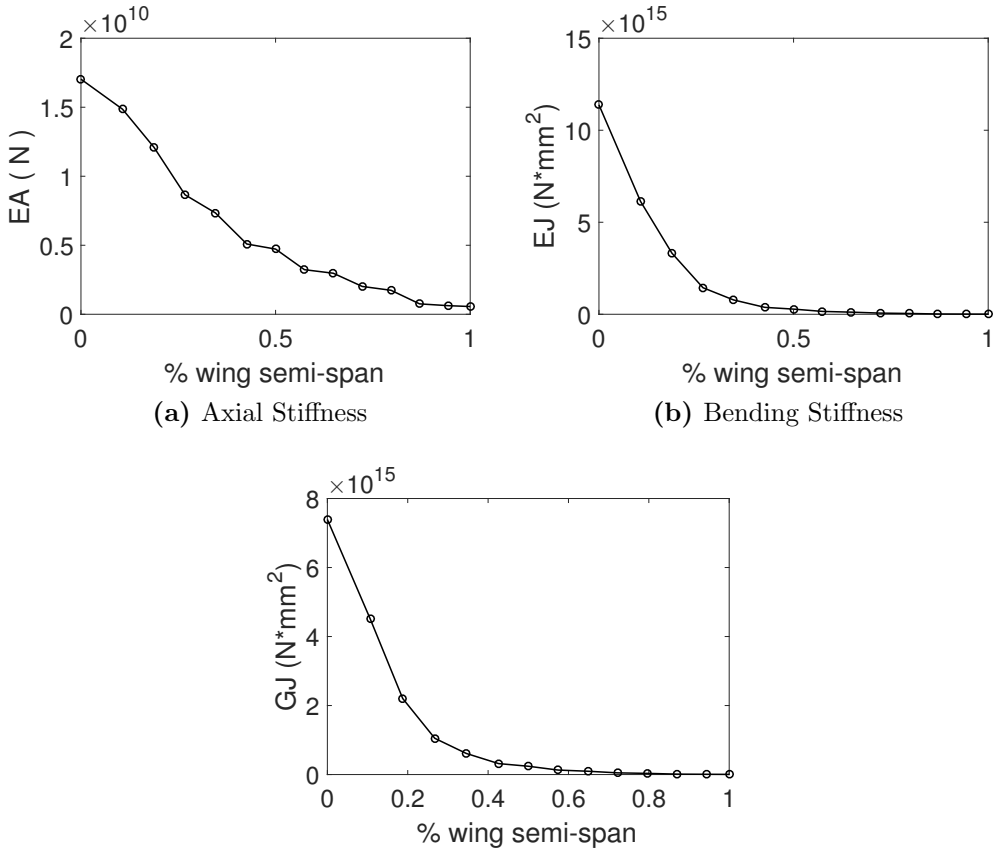

(a) Axial Stiffness

(b) Bending Stiffness

(c) Bending Stiffness

Figure 5.42: Mechanical properties of wing cross sections along the halfwing span.

computed for 14 stations along the half-wing span, using the monocoque section theory.

The obtained distributions of axial, bending and torsional stiffness are reported in Figure 5.42, while Figure 5.43 shows the position of the neutral points and shear centres. These properties, along with the in-plane bending stiffness and the product of inertia, have been interpolated and inserted in Pbeam finite element entries, developing the stick model of the wing. Using this simplified description of the wing, ribs are not taken into consideration. However they represent a substantial contribute to the overall weight of the structure. For this reason, non-structural mass linearly distributed along the wing span, has been added to model the mass of the ribs.

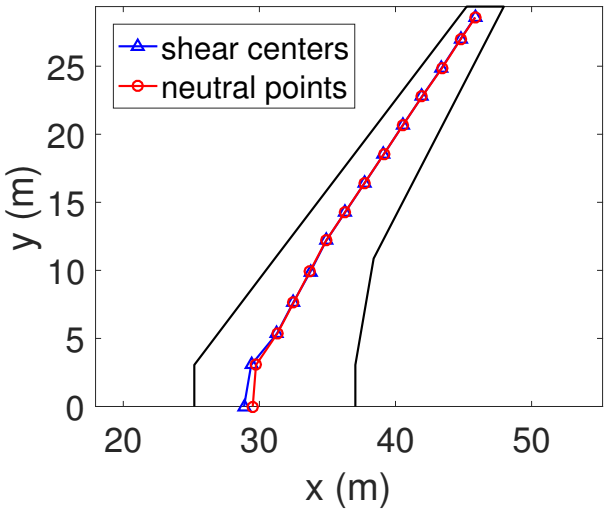

Figure 5.43: Position of section neutral points and shear centres along the halfwing span.

In order to check the accuracy of the modelling, a modal analysis has been performed for both the stick model and the provided 3-D model. The comparison of the obtained results is shown in Figure 5.46 and confirms the good estimation of cross-section stiffnesses and masses. As can be noted the position of the third and fourth mode is inverted. However, this represents an acceptable discordance, as the natural frequencies are really close one another.

The complete stick model of the wing has been completed by reflecting, with respect to the aircraft longitudinal axis, the already created beam elements. Leading and trailing edge flaps and engines are modelled using lumped masses. Another point mass was added to model the remaining part of the aircraft, making the total weight of the model to approach Boeing 777 Operating Empty Weight. Its location is chosen to match the Boeing 777 most forward position of the centre of gravity (typically critical for wing sizing [39]). The Maximum Take Off weight is reached modelling the fuel as non-structural mass linearly distributed along the wing-span (that has been added to ribs mass contribute). Another element required to compute the aeroelastic response to symmetric maneuver is the horizontal tail plane,

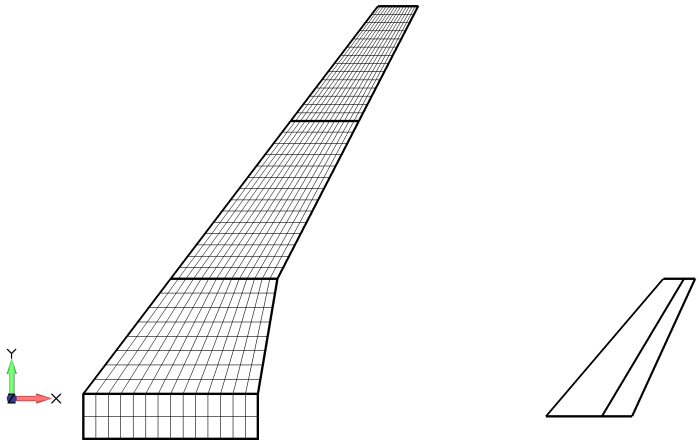

Figure 5.44: Aerodynamic model.

which is modelled using rigid elements RBE2 as no interest is given to tail plane deformability effects.

In order to analyze static the aeroelastic response, a vehicle aerodynamic model is needed. The model was created using the Doublet Lattice Method [40]. This method, implemented in Nastran, is built on the theory of incompressible, inviscid and irrotational flow, also known as ideal or potential flow. Even if this implies to assume the absence of turbulence and boundary layer phenomena, the doublet lattice method allows to compute, with a contained computational effort, the velocity field around the wing and, consequently, the pressure distribution. The lifting surface is divided into quadrilateral panels, and modelled as an infinitely thin sheet of discrete vortices. The intensity of each vortex is constant inside the corresponding panel. To account for twist and camber of the wing airfoil, a downwash correction was used. Aerodynamic control surfaces were created to allow for trimmed maneuver analysis. In Figure 5.44 the developed aerodynamic model is reported. The loads are computed for the maximum load factor (g = 2.5) pull-up maneuver at cruise speed, which is one of the critical loading condition for wing sizing. The analysis solved by Nastran falls under the so called static aeroelasticity analysis: the time variability of the applied loads is considered enough slow to allow for steady aerodynamics and to neglect structural dynamics. In Figure 5.45 is reported the distribution of bending moment and torque along

the half-wing span. These are the loads that will drive the composite wing box sizing procedure.

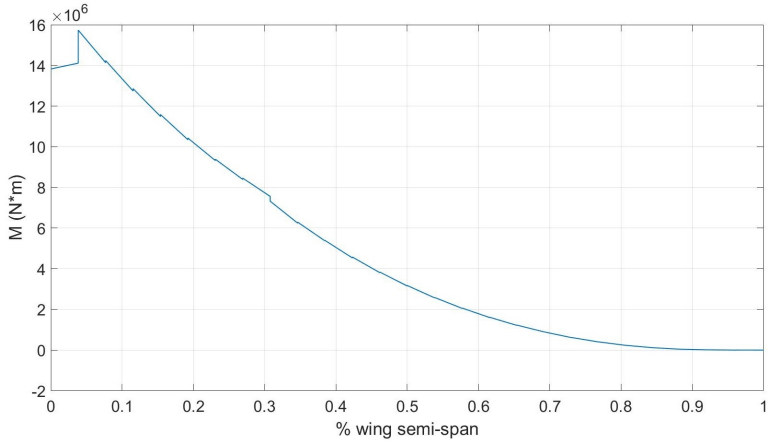

(a) *Bending moment*

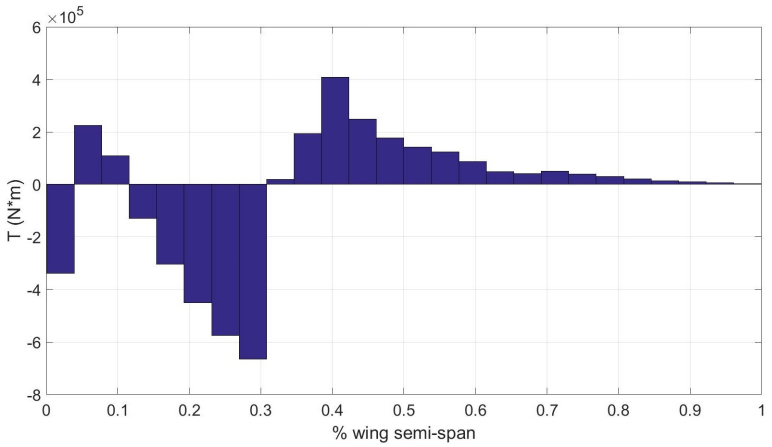

(b) *Torque*

Figure 5.45: Generalized force in beam elements along the halfwing span.

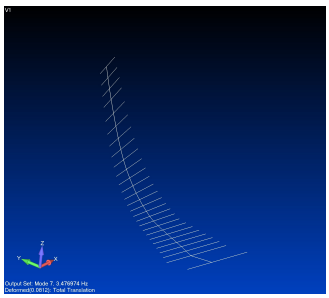

Mode 1, $f = 3.48Hz$

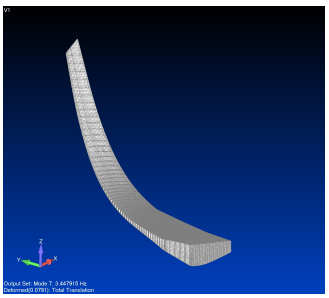

Mode 1, $f = 3.45Hz$

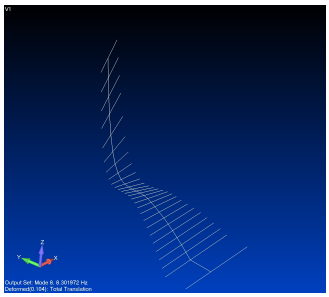

Mode 2, $f = 8.30Hz$

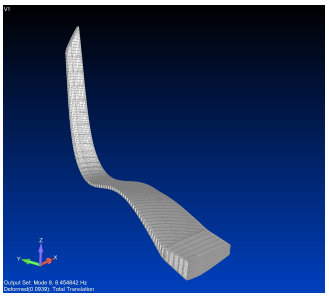

Mode 2, $f = 8.45Hz$

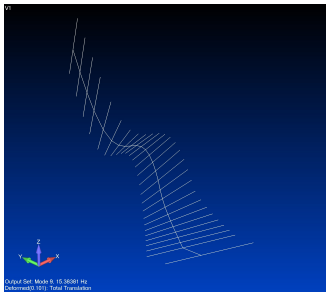

Mode 3, $f = 15.38Hz$

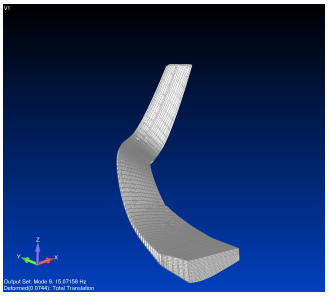

Mode 3, $f = 15.07Hz$

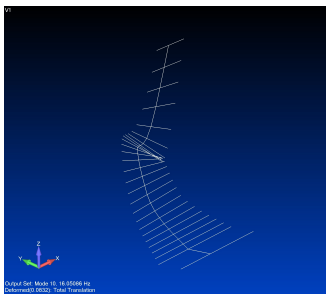

Mode 4, $f = 16.05Hz$

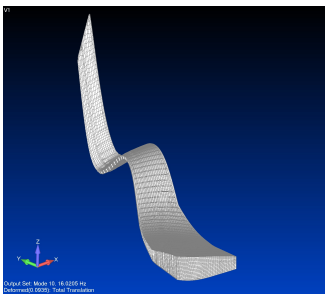

Mode 4, $f = 16.02Hz$

Figure 5.46: Comparison of the first four natural modes between stick and 3D wing FEM models.

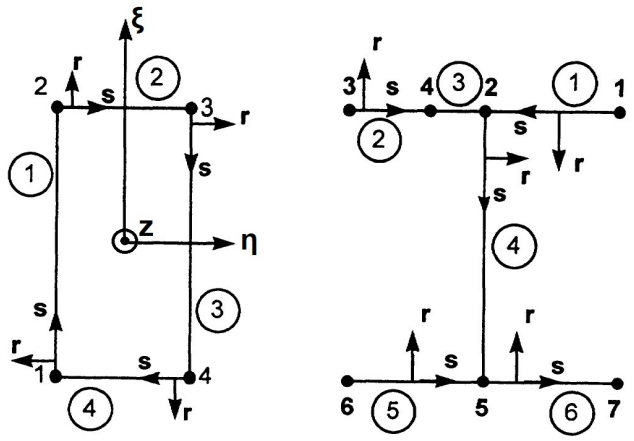

Figure 5.47: Definition of the local coordinate system (taken from [41]).

5.2.2 Composite wing-box sizing procedure

The sizing procedure is based on the thin walled composite beams theory, which is described in detail in [41]. In Figure 5.47 is reported the schematic representation of the cross section, which is described by its contour divided into segments. The segments are equipped with a local reference system (s,r), while (ξ,η,z) are the principal axes of the cross section. Each segment is modelled with the constitutive equations of classical lamination theory [25] and assuming the beam state:

$$\begin{Bmatrix} N_z^{(i)} \\ N_s^{(i)} = 0 \\ N_{zs}^{(i)} \\ M_z^{(i)} \\ M_s^{(i)} = 0 \\ M_{zs}^{(i)} \end{Bmatrix} = \begin{bmatrix} A_{11} & A_{12} & A_{16} & B_{11} & B_{12} & B_{16} \\ & A_{22} & A_{26} & B_{12} & B_{22} & B_{26} \\ & & A_{66} & B_{16} & B_{26} & B_{66} \\ & & & C_{11} & C_{12} & C_{16} \\ & & & & C_{22} & C_{26} \\ sym. & & & & & C_{66} \end{bmatrix} \begin{Bmatrix} \varepsilon_z^{(i)} \\ \varepsilon_s^{(i)} \\ \gamma_{zs}^{(i)} \\ k_z^{(i)} \\ k_s^{(i)} \\ k_{zs}^{(i)} \end{Bmatrix} \tag{5.129}$$

Similarly to what has been done for stiffeners constitutive law in Section 2.3.2, rows in Eq. 5.129 can be reordered and the matrix statically condensed to

obtain:

$$\begin{Bmatrix} N_z^{(i)} \\ M_z^{(i)} \\ N_{zs}^{(i)} \\ M_{zs}^{(i)} \end{Bmatrix} = \begin{bmatrix} A_i & B_i & 0 & 0 \\ B_i & D_i & 0 & 0 \\ 0 & 0 & F_i & C_i \\ 0 & 0 & C_i & H_i \end{bmatrix} \begin{Bmatrix} \varepsilon_z^{(i)} \\ k_z^{(i)} \\ \gamma_{zs}^{(i)} \\ k_{zs}^{(i)} \end{Bmatrix} \tag{5.130}$$

Stiffeners are modelled as concentrated axial stiffnesses. The axial deformation of the cross-section is computed using the beam classical formulas referred to the principal axes (ξ, η):

$$\varepsilon_z = \varepsilon_z^0 + \xi\, k_\eta - \eta\, k_\xi = \frac{F_z}{(EA)} + \xi\, \frac{M_\eta}{(EI_\eta)} - \eta\, \frac{M_\xi}{(EI_\xi)} \tag{5.131}$$

where the notation used for the axial stiffness (EA) and the bending stiffnesses (EI_η), (EI_ξ) is used to highlight the fact that with composite materials it is not possible to separate the elastic properties (E and G) from the geometric properties (area, moment of inertia, etc.). For the present work, the contributes of axial force F_z, and bending moment M_ξ are neglected, as their magnitude is strongly dependent from the aircraft wing configuration and usually much lower with respect to bending moment M_η. If the laminate is symmetric $B_i = 0$, and the normal stress resultant N_z can be computed substituting the constitutive relation in Eq. 5.130 in Eq. 5.131:

$$N_z^i = \xi\, \frac{M_\eta}{(EI_\eta)}\, A_i \tag{5.132}$$

The torque M_t generates a state of pure shear stress in the skin of each cell. Shear fluxes q_1 and q_2, acting in the first and second cell respectively, can be computed enforcing the moment equilibrium equation and the compatibility of the rotations:

$$\begin{cases} M_t = 2\,\Omega_1\, q_1 + 2\,\Omega_2\, q_2 \\ \beta_1 = \beta_2 \end{cases} \tag{5.133}$$

where Ω_i is the area of each cell, while β_i is the rotation of the i-th cell that is computed as:

$$\beta_i = \frac{1}{2\,\Gamma_i} \oint \frac{q_i}{F_i}\, ds \tag{5.134}$$

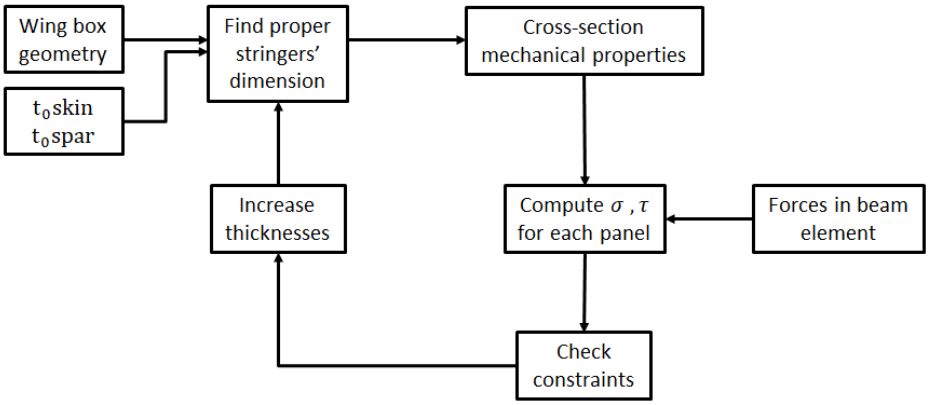

Figure 5.48: Block scheme of the wing-box sizing procedure.

being Γ_i the perimeter.

In Figure 5.48 the block scheme of the sizing procedure is reported. Once generalised forced in beam elements and cross-section mechanical properties are known, it is possible to compute the stresses using Eqs. 5.132 and 5.133. Skin thickness is chosen to satisfy strength and stability constraints. The first requirement is enforced using the maximum stress method. The stability constrained is checked using analytical expressions to compute the critical load of each panel, which is assumed to be simply supported at its edges. Stiffener dimensions are chosen in order to promote a local instability at critical load. This is translated in a requirement on stringers minimum bending stiffness, as described in detail in [42]. The process is repeated gradually increasing skin and spars thickness until all the constraints are not fully satisfied.

It should be pointed out that the resulting cross section properties are changed with respect to the isotropic structure used to compute the loads and, consequently, the aeroelastic response may be slightly different. The entire process should be repeated from the load computation phase, with the new cross-section properties, until convergence. Nonetheless, for the aim of this work, it is sufficient to stop the process at the first iteration, as the attention is not focused on the design of the wing box.

5.2.2 Reference wing box

The section of the considered wing-box is located at about 85% of the aircraft's half wingspan. Its geometry is schematically described in Figure 5.49. It is worth noting that the stiffeners are not evenly spaced on the wing-box skin. More precisely due to the wing taper ratio the external panels are reduced in width. As expected, skin sizing is stability driven, so the skin thickness is large enough to guarantee a critical load higher than the applied state of stress.
The skin of each cell can be modelled using the present method considering the following assumptions:

- the taper ratio and the distance between ribs are low,
- the effect of the panel curvature can be neglected.

With this hypotheses the wing-box skin is reduced to a stiffened rectangular plate. The boundary conditions are given by the presence of ribs and spars, which prevent the out of plane displacement at the edges of the plate. The presence of the spar-caps is taken into account adopting clamped boundary conditions in correspondence of the short edges.
The effect of the stiffeners geometric curvature will be studied using the skin of the largest cell as a baseline. The geometry of the reference configuration with straight stiffeners, along with thicknesses and dimensions resulting from the sizing process, is reported in Figure 5.50. The mode shape in the case of uniaxial compression load, along with the value of the critical load, is plotted in Figure 5.51.

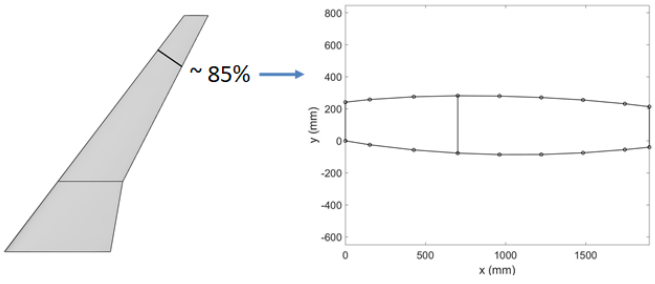

Figure 5.49: Schematic representation of the wing box chosen as reference.

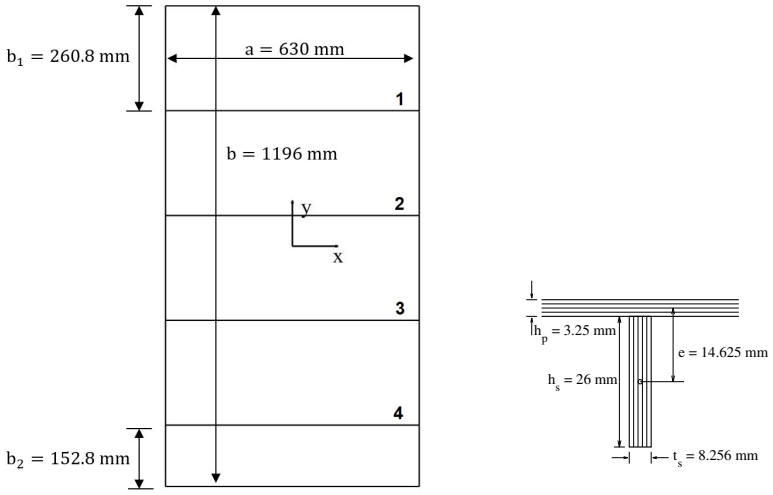

Figure 5.50: Description of the reference configuration resulting from the wing-box sizing process.

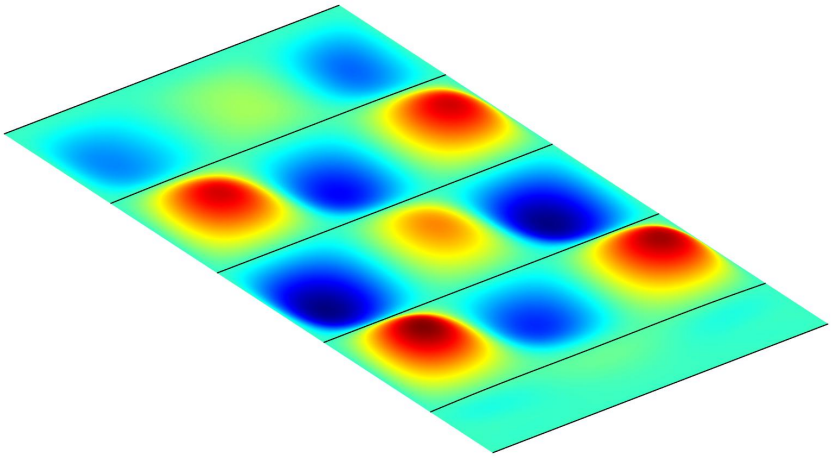

(a) $N_{xx}^{cr} = 184.5$ N/mm

Figure 5.51: Buckling mode shape and critical load value for the reference configuration under uniaxial compression.

5.3 Results

The number of parameters to describe the geometry of the problem increases rapidly with the number of stiffeners. If they are forced to start and end at plate edges, the addition of one stringer add four more variables[12] to the problem. For this reason the optimal stiffeners configuration can be achieved using global optimization techniques [43]. Nonetheless topological optimization of curvilinearly stiffened panels lies outside the scope of this activity. A better understanding of the potential benefits of curvilinear stiffeners can be achieved with simple parametric studies by allowing the variation of few, meaningful parameters.
In this context the stability behaviour of the reference structure in Figure 5.50 is assessed by varying the position of control point $\mathbf{P}_1$ of each stiffener, meaning that stiffeners starting and ending points remain unchanged with respect to the baseline. Similarly to what has been done in Section 3.2.3, the stiffeners curvature is determined by parameter d that measures the distance along y between $\mathbf{P}_1$ and the line joining the other two control points. In order to further reduce the number of variables, the parameter d of each stiffener is determined using the following law:

$$\begin{aligned} d_1 &= \frac{1}{6}\,\alpha \\ d_2 &= \frac{1}{3}\,\alpha \\ d_3 &= \frac{2}{3}\,\alpha \\ d_4 &= \alpha \end{aligned} \tag{5.135}$$

where stiffener numbering is defined in Figure 5.50. The parameter $\alpha = d_4$ represents the curvature parameter of the fourth stringer. Increasing α, control points get more dense towards y positive direction. The control points position along x is the same for all the stiffeners. In this way the curvilinear

[12]Namely the two coordinates of point $\mathbf{P}_1$ and y coordinate of points $\mathbf{P}_0$ and $\mathbf{P}_2$

stiffeners configuration is fully determined by parameters α and β:

$$\begin{aligned}
\mathbf{P}_1^{(1)} &= \left(\beta\ ,\quad \hat{y}_{P1}^{(1)} + \tfrac{1}{6}\,\alpha\right) \\
\mathbf{P}_1^{(2)} &= \left(\beta\ ,\quad \hat{y}_{P1}^{(2)} + \tfrac{1}{3}\,\alpha\right) \\
\mathbf{P}_1^{(3)} &= \left(\beta\ ,\quad \hat{y}_{P1}^{(3)} + \tfrac{2}{3}\,\alpha\right) \\
\mathbf{P}_1^{(4)} &= \left(\beta\ ,\quad \hat{y}_{P1}^{(4)} + \alpha\right)
\end{aligned} \tag{5.136}$$

where $\hat{y}_{P1}^{(i)}$ is the y coordinate of control point $\mathbf{P}_1$ in the reference configuration. The results of the study are summarized in Figure 5.52. The value of the critical load is plotted for different α and β, considering different values for the combined load parameter γ. The starting point of each plot ($\alpha = 0$), represents the traditional configuration with straight stiffeners. The buckling mode shapes of the best configurations for different values of γ are illustrated in Figure 5.53, along with the results of the corresponding traditional configurations. It is worth noting that the presence of global mode for $\gamma \geq 0.3$ is due to the fact that stringers are not sized for such loading conditions.
In all the considered examples, curvilinear stiffeners are found to be beneficial, markedly increasing the value of the critical load and decreasing the stiffeners out of plane displacement in the case of global modes. It is worth noting that in the uniaxial compression case the optimal configuration is symmetric with respect to y axis. Whenever the shear contribute is different from zero ($\gamma \neq 0$), the optimal configuration loses the symmetry, and the position along x axis of control point $\mathbf{P}_1$ acts an important role in the stability behaviour of the structure. This means that more complex configuration should be investigated through a global optimization technique, with the aim to further increase the performance of the structure fully exploiting the potentiality of curvilinearly stiffened panels.
It should be pointed out the capability of the present method of efficiently modelling this type of structure. Every change of configuration can be performed varying a small number of parameters, without the need of implementing complex re-meshing or contact algorithms.

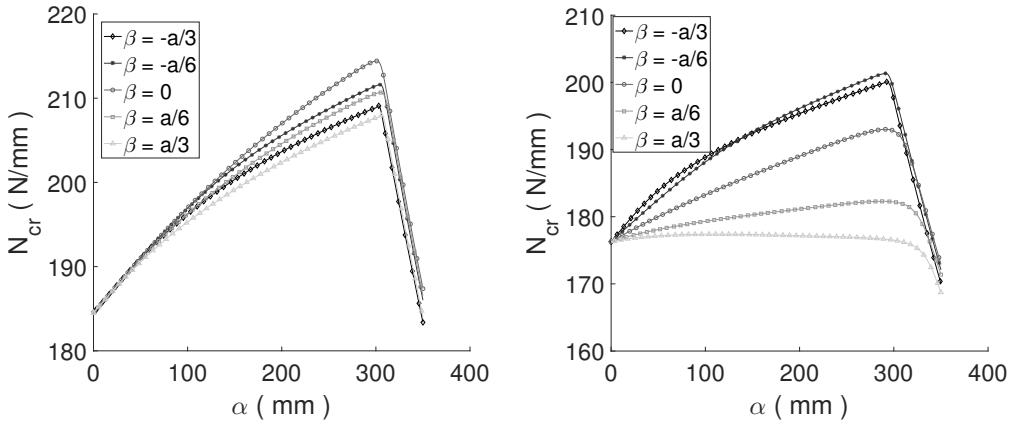

(a) $\gamma = 0.0$ **(b)** $\gamma = 0.3$

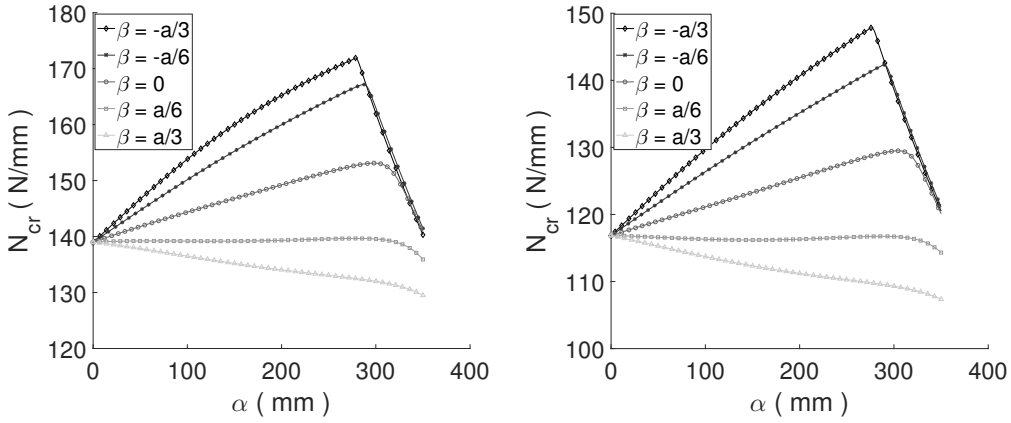

(c) $\gamma = 0.7$ **(d)** $\gamma = 1.0$

Figure 5.52: Critical load for different values of α, β and γ.

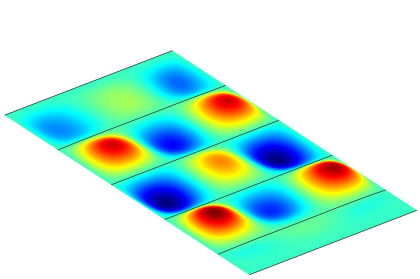

(a) $\gamma = 0.0$, $N_{xx}^{cr} = 184.5$ N/mm

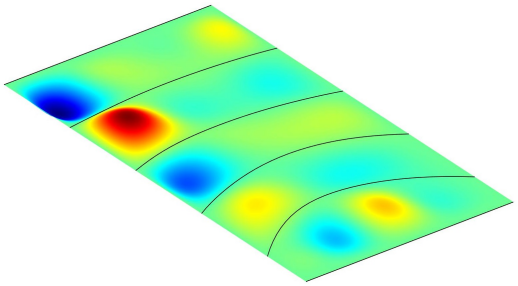

(b) $\gamma = 0.0$, $N_{xx}^{cr} = 214.4$ N/mm

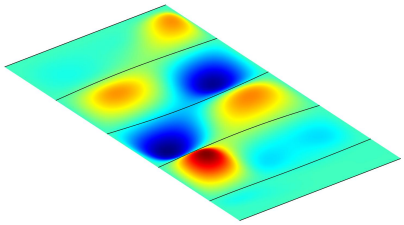

(c) $\gamma = 0.3$, $N_{xx}^{cr} = 176.3$ N/mm

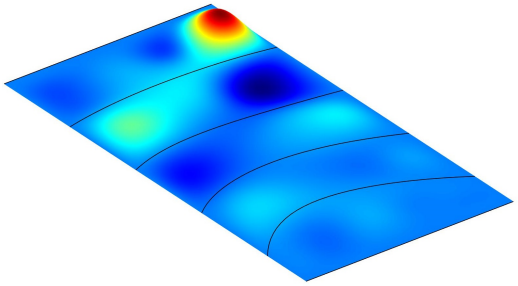

(d) $\gamma = 0.3$, $N_{xx}^{cr} = 201.3$ N/mm

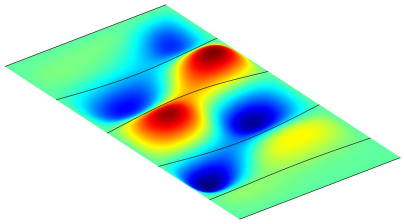

(e) $\gamma = 0.7$, $N_{xx}^{cr} = 139.0$ N/mm

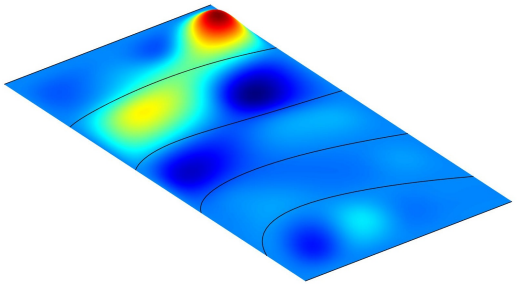

(f) $\gamma = 0.7$, $N_{xx}^{cr} = 171.9$ N/mm

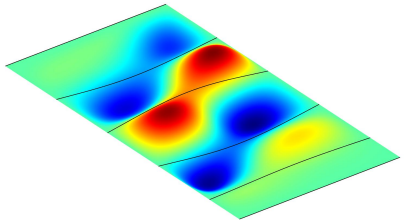

(g) $\gamma = 1.0$, $N_{xx}^{cr} = 116.9$ N/mm

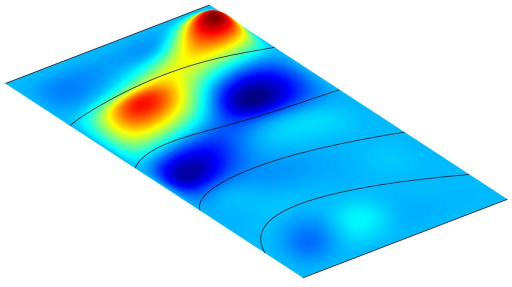

(h) $\gamma = 1.0$, $N_{xx}^{cr} = 147.8$ N/mm

Figure 5.53: Mode shape of the optimal configuration for different values of γ.

6. Conclusions

A Ritz-based approach for the analysis of stiffened composite panels with arbitrarily shaped stiffeners has been developed. A first-order shear-deformable theory is employed to model the deflections of both the composite panel and the curved composite stiffeners, and two approaches to enforce plate/stringers compatibility are explained in detail. The method is capable of managing different type of boundary and loading conditions.
The almost null modelling time and the reduced computational burden make the Ritz method particularly suitable for the analysis of these structures: the inherent complexity of the geometry leads to the need of a deep investigation of the design space, hence a fast yet accurate modelling procedure is of prime importance.
After a preliminary validation of the developed computational tool, the potentialities of the Ritz method are exploited to study the mechanical behaviour of curvilinearly stiffened panels and the benefits that this solution could bring to aeronautical airframe design. Curvilinear stiffeners are found to be beneficial whenever the traditional structural solution does not allow for a evenly-spaced configuration for the stiffeners. This situation can occur in the case of an aircraft wing-box where the wing taper ratio, may cause the reduction of the transverse area.
Nonetheless, this work represents a preliminary investigation of the problem. All of the considerations are driven here from buckling considerations, whilst a real design should consider a more complex set of design requirements, including, but not restricted to, aeroelastic responses and dynamic ones.
A global optimization technique may be the best approach to have a more clear idea of the potential advantages of this structural solution, and how

they depend on the geometry of the problem and on the loading conditions. Moreover the computational tool can be improved, for example adding the possibility to model non-rectangular plates, or implementing other type of analysis. In this context the investigation of the post-buckling behaviour of curvilinearly stiffened panel may be interesting to asses the level of residual stiffness of these structures after the critical load.

Appendix A

In section 2.5 it has been showed how it is possible to express the strain parameter ε_t^0 in function of the linear displacement of the plate. Here is presented the same approach for all the other strain components and curvatures:

$$
\begin{aligned}
\varepsilon_t^0 &= \frac{\partial\, u_t^0}{\partial s} - \kappa\, v_n^0 \\
&= \frac{\partial\left(\mathbf{u}_p^0 \cdot \mathbf{t}\right)}{\partial s} - \kappa\,\left(\mathbf{u}_p^0 \cdot \mathbf{n}\right) \\
&= \frac{\partial \mathbf{u}_p^0}{\partial s} \cdot \mathbf{t} + \cancel{\mathbf{u}_p^0 \cdot \frac{\partial \mathbf{t}}{\partial s} - \kappa\,\left(\mathbf{u}_p^0 \cdot \mathbf{n}\right)} \\
&= \left[\frac{1}{J_s}\left(\frac{2}{a}\frac{\partial \mathbf{\Phi}_u}{\partial \xi}\frac{\partial x}{\partial \zeta} + \frac{2}{b}\frac{\partial \mathbf{\Phi}_u}{\partial \eta}\frac{\partial y}{\partial \zeta}\right)\mathbf{a}_p^u\right] \cdot \mathbf{t} \\
&= \left[\frac{\mathbf{t}^T}{J_s}\left(\frac{2}{a}\frac{\partial \mathbf{\Phi}_u}{\partial \xi}\frac{\partial x}{\partial \zeta} + \frac{2}{b}\frac{\partial \mathbf{\Phi}_u}{\partial \eta}\frac{\partial y}{\partial \zeta}\right)\right]\mathbf{a}_p^u
\end{aligned}
$$

$$
\begin{aligned}
\gamma_n^0 &= \frac{\partial\, v_n^0}{\partial s} + \kappa\, u_t^0 - \theta_b \\
&= \frac{\partial\left(\mathbf{u}_p^0 \cdot \mathbf{n}\right)}{\partial s} + \kappa\,\left(\mathbf{u}_p^0 \cdot \mathbf{t}\right) - \hat{\boldsymbol{\theta}}_p \cdot \mathbf{b} \\
&= \frac{\partial \mathbf{u}_p^0}{\partial s} \cdot \mathbf{n} + \cancel{\mathbf{u}_p^0 \cdot \frac{\partial \mathbf{n}}{\partial s} + \kappa\,\left(\mathbf{u}_p^0 \cdot \mathbf{t}\right)} - \hat{\boldsymbol{\theta}}_p \cdot \mathbf{b} \\
&= \left[\frac{1}{J_s}\left(\frac{2}{a}\frac{\partial \mathbf{\Phi}_u}{\partial \xi}\frac{\partial x}{\partial \zeta} + \frac{2}{b}\frac{\partial \mathbf{\Phi}_u}{\partial \eta}\frac{\partial y}{\partial \zeta}\right)\mathbf{a}_p^u\right] \cdot \mathbf{n} - \left[\mathfrak{J}^T\, \mathbf{\Phi}_{\boldsymbol{\theta}}\, \mathbf{a}_p^\theta\right] \cdot \mathbf{b} \\
&= \left[\frac{\mathbf{n}^T}{J_s}\left(\frac{2}{a}\frac{\partial \mathbf{\Phi}_u}{\partial \xi}\frac{\partial x}{\partial \zeta} + \frac{2}{b}\frac{\partial \mathbf{\Phi}_u}{\partial \eta}\frac{\partial y}{\partial \zeta}\right)\right]\mathbf{a}_p^u - \left[\mathbf{b}^T \mathfrak{J}^T\, \mathbf{\Phi}_{\boldsymbol{\theta}}\right]\, \mathbf{a}_p^\theta
\end{aligned}
$$

$$
\begin{aligned}
\gamma_b^0 &= \frac{\partial\, w_b^0}{\partial s} + \theta_n \\
&= \frac{\partial\left(\mathbf{u}_p^0 \cdot \mathbf{b}\right)}{\partial s} + \hat{\boldsymbol{\theta}}_p \cdot \mathbf{n} \\
&= \frac{\partial \mathbf{u}_p^0}{\partial s} \cdot \mathbf{n} + \cancel{\mathbf{u}_p^0 \cdot \frac{\partial \mathbf{b}}{\partial s}} + \hat{\boldsymbol{\theta}}_p \cdot \mathbf{n} \\
&= \left[\frac{1}{J_s}\left(\frac{2}{a}\frac{\partial \boldsymbol{\Phi}_u}{\partial \xi}\frac{\partial x}{\partial \zeta} + \frac{2}{b}\frac{\partial \boldsymbol{\Phi}_u}{\partial \eta}\frac{\partial y}{\partial \zeta}\right)\mathbf{a}_p^u\right] \cdot \mathbf{b} + \left[\boldsymbol{\jmath}^T\, \boldsymbol{\Phi}_{\boldsymbol{\theta}}\, \mathbf{a}_p^\theta\right] \cdot \mathbf{n} \\
&= \left[\frac{\mathbf{b}^T}{J_s}\left(\frac{2}{a}\frac{\partial \boldsymbol{\Phi}_u}{\partial \xi}\frac{\partial x}{\partial \zeta} + \frac{2}{b}\frac{\partial \boldsymbol{\Phi}_u}{\partial \eta}\frac{\partial y}{\partial \zeta}\right)\right]\mathbf{a}_p^u + \left[\mathbf{n}^T\boldsymbol{\jmath}^T\, \boldsymbol{\Phi}_{\boldsymbol{\theta}}\right]\mathbf{a}_p^\theta
\end{aligned}
$$

$$
\begin{aligned}
k_t &= \frac{\partial\, \theta_t}{\partial s} - \kappa\, \theta_n \\
&= \frac{\partial\left(\hat{\boldsymbol{\theta}}_p \cdot \mathbf{t}\right)}{\partial s} - \kappa\left(\hat{\boldsymbol{\theta}}_p \cdot \mathbf{n}\right) \\
&= \frac{\partial \hat{\boldsymbol{\theta}}_p}{\partial s} \cdot \mathbf{t} + \cancel{\hat{\boldsymbol{\theta}}_p \cdot \frac{\partial \mathbf{t}}{\partial s} - \kappa\left(\hat{\boldsymbol{\theta}}_p \cdot \mathbf{n}\right)} \\
&= \left[\frac{1}{J_s}\left(\frac{2}{a}\boldsymbol{\jmath}^T\frac{\partial \boldsymbol{\Phi}_\theta}{\partial \xi}\frac{\partial x}{\partial \zeta} + \frac{2}{b}\boldsymbol{\jmath}^T\frac{\partial \boldsymbol{\Phi}_\theta}{\partial \eta}\frac{\partial y}{\partial \zeta}\right)\mathbf{a}_p^\theta\right] \cdot \mathbf{t} \\
&= \left[\frac{\mathbf{t}^T}{J_s}\left(\frac{2}{a}\boldsymbol{\jmath}^T\frac{\partial \boldsymbol{\Phi}_\theta}{\partial \xi}\frac{\partial x}{\partial \zeta} + \frac{2}{b}\boldsymbol{\jmath}^T\frac{\partial \boldsymbol{\Phi}_\theta}{\partial \eta}\frac{\partial y}{\partial \zeta}\right)\right]\mathbf{a}_p^\theta
\end{aligned}
$$

$$
\begin{aligned}
k_n &= \frac{\partial\, \theta_n}{\partial s} + \kappa\, \theta_t \\
&= \frac{\partial\left(\hat{\boldsymbol{\theta}}_p \cdot \mathbf{n}\right)}{\partial s} + \kappa\left(\hat{\boldsymbol{\theta}}_p \cdot \mathbf{t}\right) \\
&= \frac{\partial \hat{\boldsymbol{\theta}}_p}{\partial s} \cdot \mathbf{n} + \cancel{\hat{\boldsymbol{\theta}}_p \cdot \frac{\partial \mathbf{n}}{\partial s} + \kappa\left(\hat{\boldsymbol{\theta}}_p \cdot \mathbf{t}\right)} \\
&= \left[\frac{1}{J_s}\left(\frac{2}{a}\boldsymbol{\jmath}^T\frac{\partial \boldsymbol{\Phi}_\theta}{\partial \xi}\frac{\partial x}{\partial \zeta} + \frac{2}{b}\boldsymbol{\jmath}^T\frac{\partial \boldsymbol{\Phi}_\theta}{\partial \eta}\frac{\partial y}{\partial \zeta}\right)\mathbf{a}_p^\theta\right] \cdot \mathbf{n} \\
&= \left[\frac{\mathbf{n}^T}{J_s}\left(\frac{2}{a}\boldsymbol{\jmath}^T\frac{\partial \boldsymbol{\Phi}_\theta}{\partial \xi}\frac{\partial x}{\partial \zeta} + \frac{2}{b}\boldsymbol{\jmath}^T\frac{\partial \boldsymbol{\Phi}_\theta}{\partial \eta}\frac{\partial y}{\partial \zeta}\right)\right]\mathbf{a}_p^\theta
\end{aligned}
$$

$$
\begin{aligned}
k_b &= \frac{\partial\,\theta_b}{\partial s} \\
&= \frac{\partial\left(\hat{\boldsymbol{\theta}}_p \cdot \mathbf{b}\right)}{\partial s} \\
&= \frac{\partial \hat{\boldsymbol{\theta}}_p}{\partial s} \cdot \mathbf{b} + \hat{\boldsymbol{\theta}}_p \cdot \cancel{\frac{\partial \mathbf{b}}{\partial s}} \\
&= \left[\frac{1}{J_s}\left(\frac{2}{a}\,\boldsymbol{\jmath}^T\,\frac{\partial \boldsymbol{\Phi}_\theta}{\partial \xi}\,\frac{\partial x}{\partial \zeta} + \frac{2}{b}\,\boldsymbol{\jmath}^T\,\frac{\partial \boldsymbol{\Phi}_\theta}{\partial \eta}\,\frac{\partial y}{\partial \zeta}\right)\,\mathbf{a}_p^\theta\right] \cdot \mathbf{b} \\
&= \left[\frac{\mathbf{b}^T}{J_s}\left(\frac{2}{a}\,\boldsymbol{\jmath}^T\,\frac{\partial \boldsymbol{\Phi}_\theta}{\partial \xi}\,\frac{\partial x}{\partial \zeta} + \frac{2}{b}\,\boldsymbol{\jmath}^T\,\frac{\partial \boldsymbol{\Phi}_\theta}{\partial \eta}\,\frac{\partial y}{\partial \zeta}\right)\right]\,\mathbf{a}_p^\theta
\end{aligned}
$$

At this point, collecting everything in a single compact relation:

$$
\begin{Bmatrix} \boldsymbol{\varepsilon}_{\boldsymbol{s}}^{\mathbf{0}} \\ \mathbf{k}_s \end{Bmatrix} = \begin{bmatrix} \frac{\mathbf{t}^T}{J_s}\left(\frac{2}{a}\,\frac{\partial \boldsymbol{\Phi}_u}{\partial \xi}\,\frac{\partial x}{\partial \zeta} + \frac{2}{b}\,\frac{\partial \boldsymbol{\Phi}_u}{\partial \eta}\,\frac{\partial y}{\partial \zeta}\right) & \mathbf{0} \\ \frac{\mathbf{n}^T}{J_s}\left(\frac{2}{a}\,\frac{\partial \boldsymbol{\Phi}_u}{\partial \xi}\,\frac{\partial x}{\partial \zeta} + \frac{2}{b}\,\frac{\partial \boldsymbol{\Phi}_u}{\partial \eta}\,\frac{\partial y}{\partial \zeta}\right) & -\mathbf{b}^T\boldsymbol{\jmath}^T\,\boldsymbol{\Phi}_{\boldsymbol{\theta}} \\ \frac{\mathbf{b}^T}{J_s}\left(\frac{2}{a}\,\frac{\partial \boldsymbol{\Phi}_u}{\partial \xi}\,\frac{\partial x}{\partial \zeta} + \frac{2}{b}\,\frac{\partial \boldsymbol{\Phi}_u}{\partial \eta}\,\frac{\partial y}{\partial \zeta}\right) & \mathbf{n}^T\boldsymbol{\jmath}^T\,\boldsymbol{\Phi}_{\boldsymbol{\theta}} \\ \mathbf{0} & \frac{\mathbf{t}^T}{J_s}\left(\frac{2}{a}\,\boldsymbol{\jmath}^T\,\frac{\partial \boldsymbol{\Phi}_\theta}{\partial \xi}\,\frac{\partial x}{\partial \zeta} + \frac{2}{b}\,\boldsymbol{\jmath}^T\,\frac{\partial \boldsymbol{\Phi}_\theta}{\partial \eta}\,\frac{\partial y}{\partial \zeta}\right) \\ \mathbf{0} & \frac{\mathbf{n}^T}{J_s}\left(\frac{2}{a}\,\boldsymbol{\jmath}^T\,\frac{\partial \boldsymbol{\Phi}_\theta}{\partial \xi}\,\frac{\partial x}{\partial \zeta} + \frac{2}{b}\,\boldsymbol{\jmath}^T\,\frac{\partial \boldsymbol{\Phi}_\theta}{\partial \eta}\,\frac{\partial y}{\partial \zeta}\right) \\ \mathbf{0} & \frac{\mathbf{b}^T}{J_s}\left(\frac{2}{a}\,\boldsymbol{\jmath}^T\,\frac{\partial \boldsymbol{\Phi}_\theta}{\partial \xi}\,\frac{\partial x}{\partial \zeta} + \frac{2}{b}\,\boldsymbol{\jmath}^T\,\frac{\partial \boldsymbol{\Phi}_\theta}{\partial \eta}\,\frac{\partial y}{\partial \zeta}\right) \end{bmatrix} \begin{Bmatrix} \mathbf{a}_p^u \\ \mathbf{a}_p^\theta \end{Bmatrix} = \boldsymbol{H}_1\,\mathbf{a}_p
$$

Similarly for the term involved by the geometric contribute we can write:

$$
w_{b/s}^0 = \begin{bmatrix} \mathbf{0} & \mathbf{0} & \frac{\mathbf{b}^T}{J_s}\left(\frac{2}{a}\,\frac{\partial \boldsymbol{\Phi}_u}{\partial \xi}\,\frac{\partial x}{\partial \zeta} + \frac{2}{b}\,\frac{\partial \boldsymbol{\Phi}_u}{\partial \eta}\,\frac{\partial y}{\partial \zeta}\right) & \mathbf{0} & \mathbf{0} & \mathbf{0} \end{bmatrix}\,\mathbf{a}_p = \boldsymbol{H}_2\,\mathbf{a}_p
$$

Bibliography

[1] S. Biggers and S. Fageau. "Shear buckling response of tailored rectangular composite plates". *AIAA Journal* 32.5 (1994), pp. 1100–1103.

[2] V. Oliveri, D. Peeters, G.J. Clancy, D. Jones, R. O'Higgins, and P.M. Weaver. "Design, optimization and manufacturing of a unitized carbon fiber/thermoplastic wingbox structure". In: *AIAA/ASCE/AHS/ASC Structures, Structural Dynamics, and Materials Conference*. 2018, p. 0476.

[3] R.K. Kapania, J. Li, and H. Kapoor. "Optimal Design of Unitized Panels with Curvilinear Stiffeners". In: *AIAA 5th Aviation, Technology, Integration, and Operations Conference*. 2005, p. 7482.

[4] K. Cooper, R. Crockett, and F. Roberts. "Free Form Fabrication in Space". In: *42nd AIAA Aerospace Sciences Meeting and Exhibit*. 2004, p. 1307.

[5] D. Locatelli, S.B. Mulani, and R.K. Kapania. "Wing-Box Weight Optimization Using Curvilinear Spars and Ribs". *Journal of Aircraft* 48.5 (2008), pp. 1671-1684.

[6] W. Zhao and R.K. Kapania. "Buckling analysis of unitized curvilinearly stiffened composite panels". *Composite Structures* 135 (2015), pp. 365-382.

[7] W. Ritz. "Uber eine neue Methode zur Lösung gewisser Variationsprobleme der mathematischen Physik". *Journal Fuer die Eeine und Angewandte Math-ematik* 135 (1909), pp. 1-61.

[8] C. Bisagni and R. Vescovini. "Analytical formulation for local buckling and post-buckling analysis of stiffened laminated panels". *Thin-Walled Structures* 47.3 (2009), pp. 318-334.

[9] R. Vescovini and C. Bisagni. "Semi-analytical buckling analysis of omega stiffened panels under multi-axial loads". *Composite Structures* 120 (2015), pp. 285-299.

[10] R. Vescovini and C. Bisagni. "Two-step procedure for fast post-buckling analysis of composite stiffened panels". *Computers & Structures* 128 (2013), pp. 38-47.

[11] C. Bisagni and R. Vescovini. "Fast tool for buckling analysis and optimization of stiffened panels." *Journal of Aircraft* 46.6 (2009), pp. 2041-2053.

[12] R. Vescovini and C. Bisagni. "Buckling Analysis and Optimization of Stiffened Composite Flat and Curved Panels." *AIAA Journal* 50.4 (2012), pp. 904-915.

[13] R. Vescovini and C. Bisagni. "A fast procedure for the design of composite stiffened panels." *Aeronautical Journal* 119.1212 (2015), pp. 185-201.

[14] L. Brubak, J. Hellesland, and E. Steen. "Semi-analytical buckling strength analysis of plates with arbitrary stiffener arrangements". *Journal of Constructional Steel Research* 63 (2007), pp. 532–543.

[15] L. Brubak, J. Hellesland, and O.J. Hareide. "Vibration Analysis of Plates with Arbitrary Stiffener Arrangements Using a Semi-Analytical Approach". In: *V International Conference on Computational Methods in Marine Engineering (MARINE 2013)*. 2013.

[16] L. Brubak and J. Hellesland. "Strength criteria in semi-analytical, large deflection analysis of stiffened plates in local and global bending". *Thin-Walled Structures* 46 (2008), pp. 1382– 1390.

[17] A.Y. Tamijani and R.K. Kapania. "Chebyshev–Ritz Approach to Buckling and Vibration of Curvilinearly Stiffened Plate". *AIAA Journal* 50.5 (2012), pp. 1007–1018.

[18] P. Shi, R.K. Kapania, and C.Y. Dong. "Free Vibration of Curvilinearly Stiffened Shallow Shells". *Journal of Vibration and Acoustics* 137 (2015).

[19] A.Y. Tamijani and R.K. Kapania. "Buckling and Static Analysis of Curvilinearly Stiffened Plates Using Mesh-Free Method". *AIAA Journal* 48.12 (2010), pp. 2739–2751.

[20] A.Y. Tamijani and R.K. Kapania. "Vibration of Plate With Curvilinear Stiffeners Using Mesh-Free Method". *AIAA Journal* 48.8 (2010), pp. 1569–1581.

[21] A.Y. Tamijani, T. McQuigg, and R.K. Kapania. "Free Vibration Analysis of Curvilinear-Stiffened Plates and Experimental Validation". *Journal of Aircraft* 47.1 (2010), pp. 192–200.

[22] V. Giavotto. *Strutture Aeronautiche*. CittàStudiEdizioni, 1993.

[23] J. Bonet and R.D. Wood. *Nonlinear Continuum Mechanics for Finite Element Analysis*. Cambridge University Press, 1997.

[24] K.D. Hjelmstad. *Fundamentals of Structural Mechanics*. Springer, 2005.

[25] J.N. Reddy. *Mechanics of Laminated Composite Plates and Shells*. CRC Press LCC, 2004.

[26] V. Oliveri, A. Milazzo, and P.M. Weaver. "Thermo-mechanical post-buckling analysis of variable angle tow composite plate assemblies". *Composite Structures* 183 (2017), pp. 620-635.

[27] V. Oliveri, A. Alaimo, and A. Milazzo. "Post-buckling analysis of damaged multilayered composite stiffened plates by Rayleigh-Ritz method". *Applied Mechanics and Materials* 828 (2016), pp. 99-116.

[28] A. Milazzo and V. Oliveri. "Post-buckling analysis of cracked multilayered composite plates by pb-2 Rayleigh–Ritz method". *Composite Structures* 132 (2015) pp. 75-86.

[29] R. Vescovini, L. Dozio, M. D'Ottavio, and O.Polit. "On the application of the Ritz method to free vibration and buckling analysis of highly anisotropic plates". *Composite Structures* 192 (2018), pp. 460-474.

[30] A. Molteni (2006). *Introduzione alla teoria delle curve differenziabili* (Master's thesis). Retrieved from http://www.mat.unimi.it/users/alzati/personale/index.html

[31] H. S. Velásquez Leiva (2014). *Structural design optimization of an aircraft composite wing-box using curvilinear stiffeners* (Master's thesis). Retrieved from http://edoc.sub.uni-hamburg.de/haw/volltexte/2014/2685/

[32] L. Martini and R. Vitaliani "On the Polynomial Convergent Formulation of a C^0 Isoparametric Skew Beam Element". *Computers & Structures* 29.3 (1988), pp. 437-449.

[33] C. Bisagni, R. Vescovini, and C. G. Dávila. "Single-Stringer Compression Specimen for the Assessment of Damage Tolerance of Postbuckled Structures". *Journal of Aircraft* 48.2 (2011), pp. 495-502.

[34] M.C. Niu. *Composite Airframe Structures*. Hong Kong Conmilit Press limited, 1992.

[35] E. Cosentino and P.M. Weaver. "Prebuckling and Buckling of Unsymmetrically Laminated Composite Panels with Stringer Run-Outs". *AIAA Journal* 47.10 (2009), pp. 2284-2297.

[36] E. Cosentino and P.M. Weaver. "Buckling of Stiffened Composite Panels with Stringer Terminations". *Journal of Mechanics of Materials and Structures* 4.9 (2009), pp. 1505-1533.

[37] J. Vassberg, M. Dehaan, M. Rivers, and R. Wahls. "Development of a Common Research Model for Applied CFD Validation Studies". In: *26th AIAA Applied Aerodynamics Conference*. 2008, p. 6919.

[38] NASA Common Research Model. (2013). Retrieved from http://commonresearchmodel.larc.nasa.gov/

[39] J. Robinson, S. Doyle, G. Ogawa, M. Baker, S. De, M. Jrad, and R.K. Kapania. "Aeroelastic Optimization of Wing Structure Using Curvilinear Spars and Ribs (SpaRibs)". In: *17th AIAA/ISSMO Multidisciplinary Analysis and Optimization Conference*. 2016, p. 1303

[40] MSC Software Corporation. *MSC Nastran Aeroelastic Analysis User's Guide.* Santa Ana, CA, 2004.

[41] J.C. Massa and E.J. Barbero. "A Strength of Materials Formulation for Thin Walled Composite Beams with Torsion". *Journal of Composite Materials* 32.17 (1998), pp. 1560-1594.

[42] C. Mittelstedt. "Explicit analysis and design equations for buckling loads and minimum stiffener requirements of orthotropic and isotropic plates under compressive load braced by longitudinal stiffeners". *Thin-Walled Structures* 46 (2008), pp. 1409–1429.

[43] S.B. Mulani, D. Locatelli, and R.K. Kapania. "Algorithm Development fro Optimization of Arbitrary Geometry Panels using Curvilinear Stiffeners". In: *17th AIAA/ASME/ASCE/AHS/ASC Structures, Structural Dynamics, and Materials Conference*. 2010, p. 2674.